Inducing Periodic Effects in Bose-Einstein Condensates : Bloch Oscillations of Solitons and Superfluid Fraction

Franco Rabec

Sorbonne Université

Unité de recherche **Laboratoire Kastler Brossel**

Thèse présentée par **Franco Rabec**

Soutenue le **20 juin 2025**

En vue de l'obtention du grade de docteur de Sorbonne Université

Discipline **Physique**

Inducing Periodic Effects in Bose-Einstein Condensates :

Soliton Oscillations and Superfluid Fraction

Thèse dirigée par Jérôme Beugnon directeur
Jean Dalibard co-directeur

Composition du jury

Rapporteurs	Blair Blakie	professeur à l'Université d'Otago	
	Thomas Bourdel	directeur de recherche à l'Institut d'Optique	
Examinateurs	Amandine Aftalion	directrice de recherche au Laboratoire de Mathémathiques d'Orsay	
	Frank Pereira dos Santos	directeur de recherche à l'Observatoire de Paris	président du jury
Directeurs de thèse	Jérôme Beugnon	professeur à Sorbonne Université	
	Jean Dalibard	professeur au Collège de France	

Cette thèse a été préparée dans les laboratoires suivants.

Laboratoire Kastler Brossel
11 place Marcelin Berthelot
75005 Paris
France

Collège de France
11 place Marcelin Berthelot
75005 Paris
France

À mes parents, Marina et Claudio

Cuando se proclamó que la Biblioteca abarcaba todos los libros, la primera impresión fue de extravagante felicidad. Todos los hombres se sintieron señores de un tesoro intacto y secreto. […] A la desaforada esperanza, sucedió, como es natural, una depresión excesiva. La certidumbre de que algún anaquel en algún hexágono encerraba libros preciosos y de que esos libros preciosos eran inaccesibles, pareció casi intolerable

---

La biblioteca de Babel
Jorge Luis Borges

Inducing Periodic Effects in Bose-Einstein Condensates:
Soliton Oscillations and Superfluid Fraction

Abstract

This thesis investigates two phenomena in Bose-Einstein condensates related to periodicity: temporal in the first case and spatial in the second. The theory is reviewed and experiments are performed with ultracold atoms. More specifically, our experimental platform consists of a two-dimensional gas of rubidium atoms confined in a flat-bottom box of adjustable geometry. Our setup provides high control over the gas, allowing us to engineer arbitrary potentials and spin-textures.
The first investigation explores solitons, stable wave packets that maintain their shape while propagating. After reviewing theoretical foundations, the thesis presents the experimental realization of magnetic solitons. These appear as a localized spin component immersed in a bath of another component. When subjected to a constant force, these solitons exhibit oscillatory motion. This behavior is similar to an electron in a crystal performing Bloch oscillations, despite the absence of a periodic potential. This remarkable phenomenon stems, in both cases, from the inherent periodicity of the energy-momentum relationship. Experiments in both linear and ring geometries verify these oscillations. In the ring configuration, we demonstrate that the oscillations can generate quantized currents. This represents a novel mechanism for creating persistent currents in quantum fluids.
The second study examines how spatial modulation affects superfluidity, the ability to exhibit frictionless flow. The thesis experimentally demonstrates that breaking translational symmetry in a Bose-Einstein condensate reduces the superfluid fraction. This confirms predictions from the pioneering work of Leggett. We use optical lattices to create controlled density modulations. The superfluid fraction is measured using two methods: through sound propagation and compressibility measurements, and via analysis of the density profile of the cloud. The results confirm the expected reduction of superfluid fraction. These findings have particular relevance for supersolids, a state of matter exhibiting superfluid properties coexisting with spontaneous spatial ordering.

Keywords: bose-einstein condensates, superfluidity, many-body physics

Résumé

Cette thèse étudie deux phénomènes dans les condensats de Bose-Einstein liés à la périodicité : temporelle dans le premier cas et spatiale dans le second. La théorie est passée en revue et des expériences sont réalisées avec des atomes ultra-froids. Plus précisément, notre plateforme expérimentale consiste en un gaz bidimensionnel d'atomes de rubidium confinés dans une boîte à fond plat de géométrie ajustable. Notre dispositif offre un contrôle élevé sur le gaz, nous permettant de concevoir des potentiels et des textures de spin arbitraires.
La première investigation explore les solitons, des paquets d'ondes stables qui maintiennent leur forme pendant la propagation. Après avoir revu les fondements théoriques, cette thèse présente la réalisation expérimentale de solitons magnétiques. Ceux-ci apparaissent comme une composante de spin localisée immergée dans un bain d'une autre composante. Lorsqu'ils sont soumis à une force constante, ces solitons présentent un mouvement oscillatoire. Ce comportement est similaire à celui d'un électron dans un cristal effectuant des oscillations de Bloch, malgré l'absence de potentiel périodique. Ce phénomène remarquable découle, dans les deux cas, de la périodicité inhérente à la relation énergie-impulsion. Des expériences dans des géométries linéaires et en anneau vérifient ces oscillations. Dans la configuration en anneau, nous démontrons que les oscillations peuvent générer des courants quantifiés. Cela représente un nouveau mécanisme pour créer des courants persistants dans les fluides quantiques.
La seconde étude examine comment la modulation spatiale affecte la superfluidité, c'est-à-dire la capacité d'un fluide à s'écouler sans friction. La thèse démontre expérimentalement que briser la symétrie translationnelle dans un condensat de Bose-Einstein réduit la fraction superfluide. Cela confirme les prédictions des travaux pionniers de Leggett. Nous utilisons des réseaux optiques pour créer des modulations de densité contrôlées. La fraction superfluide est mesurée en utilisant deux méthodes : par la propagation du son et les mesures de compressibilité, et via l'analyse du profil de densité du nuage. Les résultats confirment la réduction attendue de la fraction superfluide. Ces découvertes ont une pertinence particulière pour les supersolides, un état de la matière présentant des propriétés superfluides coexistant avec un ordre spatial spontané.

Mots clés : condensats de bose-einstein, superfluidité, physique à n corps

Laboratoire Kastler Brossel
11 place Marcelin Berthelot – 75005 Paris – France

Remerciements

J'aimerais, avec ces quelques lignes, remercier toutes les personnes qui ont rendu ma thèse possible, ou du moins beaucoup plus agréable. À commencer par mes directeurs de thèse, Jérôme et Jean. Merci Jérôme pour ta disponibilité et tes bons conseils. J'ai appris énormément de choses grâce à toi, que ce soit sur la physique, sur les techniques et savoir-faire expérimentaux, ou plus largement sur la science. Merci Jean pour tes précieux enseignements dispensés de multiples manières : les cours au Collège de France, les notes sur les projets, les explications que tu donnais en réunion, les réponses à mes questions, mais aussi les questions que tu nous posais. Je voudrais également remercier Sylvain pour sa contribution précieuse aux projets, ses idées toujours pertinentes et sa disponibilité pour répondre à mes interrogations. Je suis très heureux d'avoir effectué ma thèse dans une équipe où les chercheurs ont toujours été bienveillants, rigoureux et irréprochables sur le plan de l'intégrité scientifique.

En arrivant dans le groupe, j'ai été accueilli par les autres doctorants Rubidium : Brice, Chloé et Guillaume Chauveau, avec qui j'ai principalement travaillé. Guillaume m'a chaleureusement intégré à l'équipe et le courant est tout de suite bien passé. Nous avons partagé de nombreuses heures ensemble, d'abord à construire la quatrième génération de l'expérience Rubidium, puis à faire fonctionner Rubidium 3. Travailler avec Guillaume a toujours été un plaisir, au point que la n-ième reconstruction d'un même chemin optique, le n-ième alignement de l'accordéon ou encore les longs scans Cicero, pour ne citer qu'eux, en devenaient presque des moments agréables. Merci d'avoir toujours été à l'écoute, et merci pour ta rigueur, ta patience et ta persévérance. Sans toi, beaucoup des résultats présentés dans ce manuscrit ne seraient pas là.

Ce fut ensuite à mon tour d'accueillir les nouveaux doctorants : à commencer par Guillaume Brochier, avec qui j'ai également travaillé sur les deux expériences, ainsi que Sarah Wattellier et Sarah Philips, qui ont repris le flambeau sur Rubidium 4. Nous avons également eu la chance de recruter Yifan en postdoc. En plus de leur travail, qui a beaucoup apporté au groupe, ils ont tous contribué à sa bonne ambiance, que ce soit lors des repas de midi, des goûters, ou le vendredi soir autour d'une bière. Je tiens à leur témoigner toute ma gratitude. Je suis également très reconnaissant envers tous les autres doctorants du deuxième étage, en particulier JB et Quentin, pour les discussions scientifiques (et moins scientifiques), ainsi que pour les moments agréables en dehors du labo, au billard ou en conférence.

Je souhaite aussi exprimer ma profonde reconnaissance à mes amis qui, bien qu'ils n'aient pas directement contribué aux travaux de recherche présentés ici, ont joué un rôle tout aussi essentiel. Les moments de détente, les discussions légères ou profondes, les éclats de rire et les instants d'évasion partagés avec eux m'ont permis de garder un équilibre précieux tout au long de cette thèse. Merci à Yann et François, avec qui j'allais boxer ; à Benjamin, Élias, Léo et Pierre, mes amis de lycée que je côtoie depuis si longtemps ;

et surtout à mon inséparable groupe d'amis de Ginette : Quentin, Léo, Pierre Pochet, Marc, Thomas, Théo, Emmanuel, Léonard et Pierre Lepore, on commence à avoir un paquet de très bon souvenirs ensemble.

Enfin, j'aimerais surtout remercier ma famille, qui m'a apporté un soutien indéfectible : mes parents, qui ont su éveiller ma curiosité dès le plus jeune âge et m'ont donné l'opportunité de faire ce que j'aimais, et bien sûr, Santi et Pablo, mes deux petits frères.

Acronyms

B | **C** | **D** | **F** | **G** | **L** | **M** | **O** | **P** | **R** | **T**

B

BEC Bose-Einstein Condensate 1–3, 5, 6, 9, 11, 14, 19, 20, 22, 25, 30, 43, 72, 76, 83, 87–89, 96, 105, 107, 109, 110
BECn Bose-Einstein Condensation 1, 5, 6, 72
BKT Berezinskii-Kosterlitz-Thouless 1, 6
BO Bloch Oscillation 2, 3, 43, 50–52, 60, 63–67, 109

C

CCD Charge-Coupled Device 8, 92
CoM Center-of-Mass 20, 46, 52, 54, 56, 57, 59, 63, 64, 101–105, 109

D

DMD Digital Micromirror Device 2, 5, 8, 10–14, 41, 42, 90–94, 96–98, 105, 109, 110

F

FWHM Full Width at Half Maximum 35

G

GP Gross-Pitaevskii 23, 34
GPE Gross-Pitaevskii Equation 3, 18–20, 23, 25, 26, 28, 30, 31, 33, 34, 41, 43, 47, 55, 57, 58, 65, 80, 82, 83, 94, 95, 98–100, 102–107, 109, 110

L

LDA Local Density Approximation 92, 104
LLE Landau-Lifshitz Equation 18, 31, 33

M

MOT Magneto-Optical Trap 6, 7, 13, 14, 91
MW MicroWave 5, 7, 11, 12, 14, 109

O

ODLRO Off Diagonal Long-Range Order 1

P

PDE Partial Differential Equation 3, 18, 19

R

rhs right-hand-side 24, 48, 55, 64, 77, 78, 81

T

ToF Time of Flight 11, 53

Outline of the Thesis

List of Figures

Introduction

The early 20th century witnessed a revolution in physics with the development of quantum mechanics. A key development in understanding the statistical behavior of identical particles was the formulation of quantum statistics. Following Planck's work on black-body radiation, Bose provided a novel derivation of it [1]. Einstein recognized the profound implications of Bose's approach, extending it to an ideal gas of massive particles [2–4]. Below a critical temperature, he predicted that a macroscopic fraction of integer-spin particles (bosons) would condense into the single-particle ground-state. This novel phase transition, termed Bose-Einstein Condensation (BECn), leads to the emergence of a new state of matter, purely quantum mechanical in origin. The concept of BECn was then extended to interacting systems by Penrose and Onsager [5], by defining BECn as the emergence of Off Diagonal Long-Range Order (ODLRO) in the one-body density matrix of the system.

The link between BECn and another fascinating quantum phenomenon, superfluidity, was first established by London [6]. A theory of superfluidity was then developed by Landau, who explained that superfluidity is a state of matter where part of the fluid flows with zero viscosity [7]. The ratio of this dissipationless flow to the total flow is called the superfluid fraction. Superfluidity was first observed in liquid ^{4}He [8, 9], where a finite Bose-Einstein Condensate (BEC) fraction was later measured [10, 11]. It is now understood that superfluidity and BECn, despite sharing a link, are two different phenomena. Indeed, superfluidity can be observed in systems that do not display BECn such as fermionic ^{3}He [12], but also Berezinskii-Kosterlitz-Thouless (BKT) fluids [13–15] like two-dimensional ^{4}He films [16] or two-dimensional Bose gases [17].

It is only seventy years after Bose's and Einstein's works, enabled by remarkable advances in atomic physics techniques, specifically laser cooling and trapping, followed by evaporative cooling, that BECn was achieved in a dilute atomic gas [18, 19]. Contrary to liquid helium, where the condensate fraction is approximately 10%, the condensate fraction of dilute atomic gases can reach values arbitrarily close to one. A few years later a degenerate Fermi gas was also realized [20]. These breakthroughs have fostered an exciting and rapidly growing field of research [21]. The first experiments cooling mixtures of different atomic species were built in the early 2000s [22–25] opening the door to the study of ultracold dipolar molecules [26], with the recent remarkable achievement of a BEC of polar molecules [27]. Ultracold atoms offer an unprecedented level of control over the system, allowing for the tuning of interactions using Feshbach resonances [28, 29] and manipulation using static magnetic fields and electromagnetic radiation across a wide range of wavelengths, from radio frequency to optical. Light plays a crucial role in controlling ultracold atoms, as it can be used to imprint potentials on them. One of the most prominent examples is the creation of optical lattices, which are typically formed by interfering several laser beams to produce a standing wave. These lattices provide

a spatially periodic potential whose depth can be easily tuned by adjusting the laser intensity. Several lattice geometries can be engineered along 1, 2, or 3 dimensions of space. In addition to conventional optical lattices, modern devices such as Digital Micromirror Devices (DMDs) [30] and spatial light modulators [31] allow for even greater flexibility, enabling the creation of complex light patterns and arbitrary optical potentials.

Optical lattices have become a powerful tool for studying the physics of interacting quantum particles on a lattice, leading to numerous breakthroughs in both bosonic and fermionic systems. A pioneering achievement was the realization of the Bose-Hubbard model, for which the celebrated superfluid to Mott insulator transition was observed [32]. For a deep enough lattice, the superfluidity of the system vanishes completely. The Fermi-Hubbard model, which describes the physics of strongly correlated fermions, has also been realized in optical lattices [33–35]. Richer quantum spin models have been realized subsequently by implementing spin-dependent interactions, such as the Heisenberg model [36–38]. Optical lattices also enable the study of topological phenomena through artificial gauge fields; these approaches have led to implementations of the Hofstadter model [39, 40] as well as the Haldane model [41].

Optical lattices externally impose a periodic modulation of the atomic density; however, in quantum gases this periodicity can also appear spontaneously. This is the case, for instance, for a vortex lattice in a rotating BEC that orders spontaneously in a triangular lattice [42–44]. In this case there is only a single order parameter shared both by the lattice structure and the superfluid, meaning that the lattice structure disappears when crossing the superfluid transition. When a system displays superfluidity simultaneously with crystalline order and these two orders correspond to different order parameters, it is called a supersolid [45]. The existence of a supersolid was debated at length. Notably, Leggett showed that the modulation of the density is associated with a reduction of the superfluid density at zero temperature [46]. Experiments first looked for signatures of supersolidity in solid helium [47, 48], but direct evidence remained elusive [49]. The realization of supersolids was one of the major achievements in the field of cold atoms over the past decade, accomplished through various innovative approaches. These include coupling atoms to optical cavities [50, 51], creating spin-orbit coupled BECs [52, 53], employing periodically driven BECs [54], and using BECs with strong magnetic dipole-dipole interactions [55–57], which have been the most extensively studied. These recent developments have motivated us to revisit Leggett's original work and to experimentally investigate the influence of a periodic modulation of the density on the superfluid fraction in a well-controlled configuration. This work was not done in a supersolid, but by modulating the density of a BEC externally using an optical lattice.

Optical lattices have also been used to study the dynamics of individual particles in a periodic potential. This situation is analogous to a non-interacting electron gas in a solid. In this context, Bloch and Zener [58, 59] strikingly predicted that, in the absence of dissipation, an electron in a crystal lattice subjected to a constant electric field would oscillate, a phenomenon known as Bloch Oscillations (BOs). The period of the oscillations is inversely proportional to the lattice spacing. In natural crystals the period of BOs is very large compared to the typical scattering rate of electrons, making them impossible to observe. BOs were first observed in a semiconductor superlattice [60–62] where the larger lattice spacing yields a shorter oscillation period. A few years later, BOs were observed with cold atoms in an optical lattice [63, 64]. Since then, they have become a powerful tool for metrology applications, such as short-range force measurement or gravimetry [65–71] as well as measurement of the fine structure constant [72, 73]. They can also be used to measure the topological properties of a system [74, 75]. BOs are a consequence of the periodicity of the energy of the system in momentum that appears

in the presence of a lattice. By submitting the particle to a uniform force, its momentum will increase linearly in time; provided the evolution is adiabatic, the particle will explore the ground state of the system. Because the energy is periodic in momentum, the particle will oscillate in real space. Note that the presence of a lattice is not necessary to observe BOs, as long as the energy is periodic in momentum, which is precisely the case of one-dimensional systems in the thermodynamic limit [76]. BOs without a lattice have been first demonstrated experimentally with an impurity immersed in a one-dimensional Bose gas [77]. In this work, we observe BOs of a wave packet, made of few thousands of atoms in a one-dimensional BEC, in the absence of a lattice.

To observe the oscillations, the wave packet must stay localized throughout the dynamics. For this reason, we create a wave packet in the form of a soliton. Solitons are localized wave packets that maintain their shape while propagating, making them ideal for studying such dynamics. Solitons constitute another fascinating phenomenon in quantum gases, particularly in BECs. They emerge as solutions to nonlinear Partial Differential Equations (PDEs), which makes them ubiquitous across various physical systems. They are encountered in nonlinear optics, superconductivity, polymer physics, plasma physics, high-energy physics, and cold atomic systems [78, 79]. In the context of BECs, solitons arise as solutions of the Gross-Pitaevskii Equation (GPE), the equation that governs the classical field describing a weakly-interacting BEC at zero temperature [80]. In our work, we realize a specific soliton called a magnetic soliton in a one-dimensional BEC with two spin components. This represents the first realization of a magnetic soliton in a system where the two components are immiscible, meaning they tend to spatially separate rather than mix.

The results presented in this thesis were obtained using an experimental setup consisting in a two-dimensional ^{87}Rb Bose-gas trapped in a flat-bottom potential; I describe it in the first chapter. The results are organized into two parts. In the first part we induce temporal periodicity by applying a force on a magnetic soliton so that it undergoes BOs, whereas in the second part, spatial periodicity is imposed in a BEC by an optical lattice, and its influence on the superfluid fraction is studied. The outline of the thesis is as follows:

- In chapter 1, I describe the experimental setup used to create and manipulate a two-dimensional BEC of ^{87}Rb atoms.
- In chapter 2, I review the theoretical as well as the experimental aspects of matter-wave solitons in one and two-component BECs. This chapter focuses on the static properties of solitons, in particular for the magnetic soliton. Our creation of a static magnetic soliton in a two-component one-dimensional BEC is presented.
- In chapter 3, I discuss the dynamical properties of solitons with a focus on our experimental observation of BOs of a magnetic soliton as well as the theoretical framework used to describe this phenomenon.
- In chapter 4, I present the theoretical framework used to study superfluidity with an emphasis on zero-temperature systems with broken translational symmetry. This framework is then applied to our experimental platform, namely a BEC in the presence of an optical lattice.
- In chapter 5, I present our experimental results on the reduction of the superfluid fraction of a BEC due to the periodic modulation of the density induced by an optical lattice.

CHAPTER 1

Producing arbitrarily shaped ultracold Bose gases in reduced dimensions

Outline of the current chapter

In this chapter, we describe our experimental apparatus to produce a ^{87}Rb two-dimensional Bose gas. This chapter does not aim at providing a detailed and comprehensive description of our setup as this was already done by several PhD theses preceding this one [81–86], its purpose is rather to give the keys to understanding the subsequent chapters and pinpoint the specific parts of the setup that are less common in cold-atoms experiments and thus worth highlighting.

In section 1.1, we outline the production of a three-dimensional BEC.

In section 1.2, we explain how we transition from a 3D to 2D cloud and how BECn can be achieved in 2D for finite size systems. We present the vertical optical lattice that strongly confines the atoms, as well as the in-plane flat-bottom traps obtained by shaping light with a DMD. We also explain how, by using a DMD, we can engineer almost any potential shape for the atoms.

In section 1.3, we discuss the two tools we can use to control the internal state of the atoms. We can either use MicroWave (MW) for global transfer between states or a pair of Raman beams that allows us to perform the transfer with spatial resolution.

Finally, in section 1.4, we explain how we control magnetic field gradients to generate uniform forces on magnetic-field sensitive states.

1.1 Three-dimensional Bose-Einstein Condensate production

We describe in this section the production of a ^{87}Rb three-dimensional BEC. An energy level diagram of ^{87}Rb is displayed in fig. 1.1. The atoms are first trapped and cooled in a commercial 2D Magneto-Optical Trap (MOT) from SYRTE. A resonant beam then pushes the atoms into the glass cell where the rest of the cooling takes place and where all the science is done subsequently. The ultra-high vacuum inside the glass cell ensures that the lifetime of the cloud is of the order of several minutes. The atoms are then captured in a 3D MOT and cooled down. We cool the atoms further, below the Doppler limit, in optical molasses, and the atoms are subsequently pumped into the $F = 1$ manifold. Afterward, the magnetic quadrupole trap is switched on; it consists of a pair of anti-Helmholtz coils, along the vertical axis, capable of generating a magnetic gradient up to $240\,\mathrm{G\,cm^{-1}}$ on the atoms. Only the atoms in the low-field-seeking state $|F = 1, m_F = -1\rangle$ are captured. The first evaporative cooling stage is performed in the magnetic quadrupole trap through radio-frequency evaporation. Because Majorana losses prevent us from producing a BEC in this trap, the atoms are transferred to a crossed optical dipole trap, consisting of two far-off resonant beams at a wavelength $\lambda = 1064\,\mathrm{nm}$. A second evaporative cooling stage is performed in the optical dipole trap to cross the BEC transition. At the end of this series of steps, totaling a duration of $\approx 25\,\mathrm{s}$, we obtain a degenerate three-dimensional cloud of $\approx 5 \times 10^5$ atoms at a temperature of $\approx 100\,\mathrm{nK}$.

1.2 From a 3D to a 2D Bose-Einstein Condensate

This section explains how we create a 2D BEC starting from a 3D BEC. While the production of ^{87}Rb 3D BEC is fairly standard for a cold atoms experiment, a 2D BEC in a flat-bottom potential is much less common. Figure 1.2 is a layout of the optical system relevant for this section and the next ones of this chapter.

1.2.1 A two-dimensional Bose-Einstein Condensate

The Hohenberg-Mermin-Wagner theorem states that long-range order cannot exist at T>0 for a dimensionality d<3 [87, 88]. Thus, BECn cannot happen for an infinite 2D system at finite temperature. Indeed, BKT theory predicts that the one-body correlation function,

$$g_1(\mathbf{r}) = \langle \hat{\Psi}^\dagger(\mathbf{r})\hat{\Psi}(0)\rangle, \tag{1.1}$$

where $\hat{\Psi}(\mathbf{r})$ is the annihilation operator for a particle at position $\mathbf{r}$, decays algebraically at temperatures close to zero [89], and thus vanishes when $|\mathbf{r}| \to \infty$. However, for finite-size systems, if the size of the system L is larger than the characteristic decay length of g_1, BECn can be reached at finite temperature. To illustrate that, we can estimate the condensed fraction, defined as the largest eigenvalue Π_0 of the one-body density matrix. For a uniform Bose gas of N particles trapped in a box of size L, the condensed fraction can be computed at temperatures close to zero by using [89]:

$$\Pi_0 \sim \left(mgN/\hbar^2\right)^{1/2D}, \tag{1.2}$$

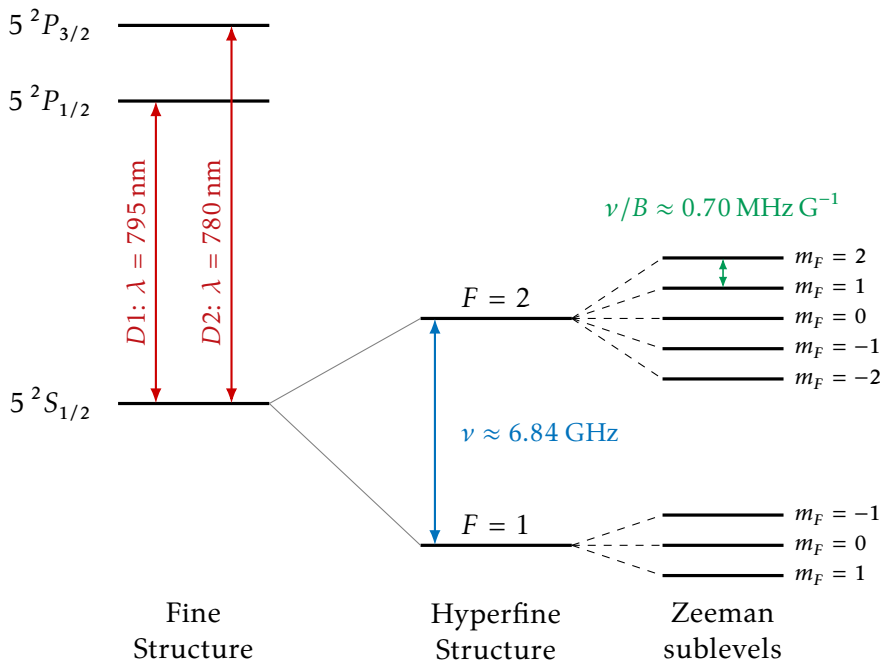

Figure 1.1: Electronic structure of ^{87}Rb, we only represent the energy levels relevant for this thesis. We represent the ground state of the fine structure, $5\,^2S_{1/2}$ and the first two excited states. Each of these states is split into hyperfine states. We only represent them for the $5\,^2S_{1/2}$ level, where the splitting lies in the MW domain. The MOT, molasses and imaging are done along the cycling transition $F = 2 \rightarrow F' = 3$ (the latter state is not represented here) of the $D2$ line. In the presence of a magnetic field B the levels are further split. Provided that the energy splitting is low compared to the hyperfine splitting, *i.e.* $\mu_B B \ll 6.84\,\mathrm{GHz}$ (which is always the case in this work), the hyperfine levels are split into the Zeeman sublevels depicted here. This diagram is not to scale.

where $D = n\lambda_{\mathrm{DB}}^2$ is the phase-space density, $n = N/L^2$ the density, and $\lambda_{\mathrm{DB}} = h/\sqrt{2\pi m k_B T}$ is the thermal de Broglie wavelength. In our experiment, we prepare two-dimensional samples of $N \sim 1 \times 10^5$ particles in a box of size $L \sim 40\,\mu\mathrm{m}$, with a temperature $T \lesssim 20\,\mathrm{nK}$, with a typical interaction parameter $g = 0.15 \times \hbar^2/m$, such that the typical condensed fraction of our samples is $\Pi_0 > 0.99$.

1.2.2 Optical dipole potentials

In all subsequent subsections, we rely on external potentials, whether it is to confine the atoms vertically, in the horizontal plane, or to imprint in-plane potentials. To achieve this, we use optical dipole potentials with light at a wavelength $\lambda = 532\,\mathrm{nm}$, far-off-resonant and blue-detuned with respect to the $D1$ and $D2$ lines. The potential seen by an atom in the presence of a light field with an intensity distribution $I(x, y, z)$ is [90]:

$$V(x, y, z) = -\frac{1}{2\epsilon_0 c}\mathcal{R}(\alpha) I(x, y, z), \tag{1.3}$$

where $\mathcal{R}$ denotes the real part and α is the complex scalar polarizability of the $5\,^2S_{1/2}$ state at $\lambda = 532\,\mathrm{nm}$, which is negative. This means the potential is proportional to the light intensity, with a positive factor in our case.

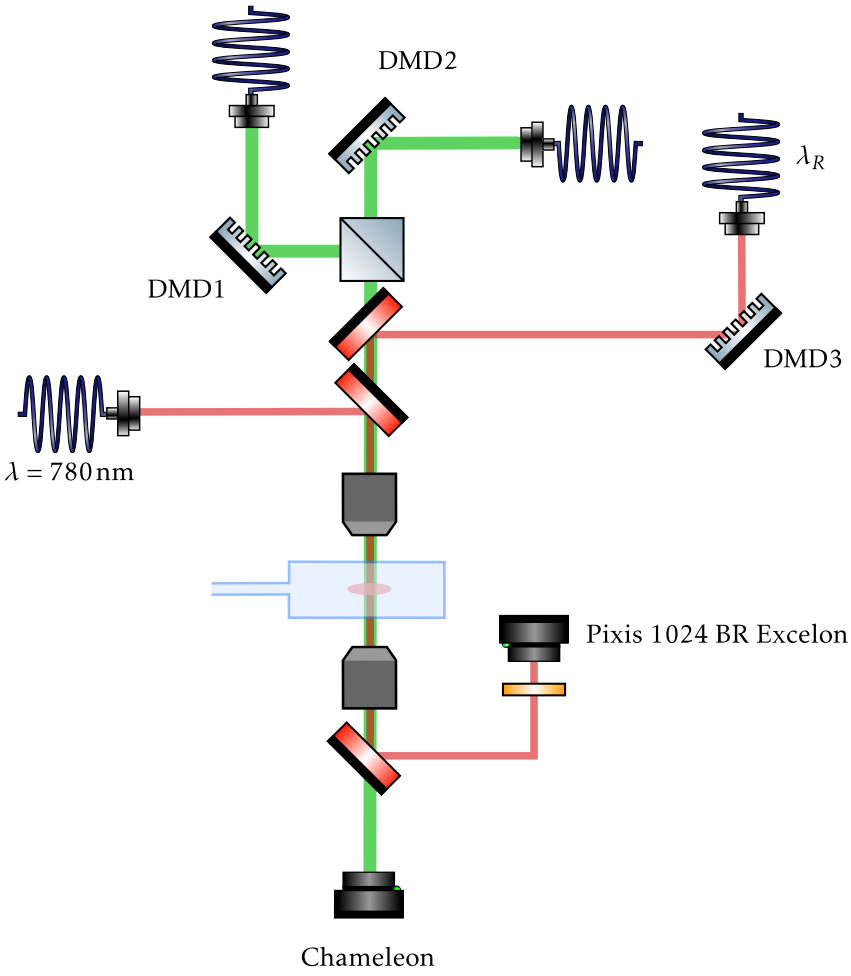

Figure 1.2: Layout of the optical setup, we only represent the simplified optical paths for the three DMDs and the imaging beam. The beams illuminating DMD1 and DMD2 have a wavelength $\lambda = 532\,\text{nm}$. DMD3 is illuminated by two copropagating beams at the tune-out wavelength λ_R, their frequency difference, equal to the hyperfine splitting $\approx 6.84\,\text{GHz}$, is fine-tuned to match the energy of the transition between the state of the $F = 1$ and the state of $F = 2$ we want to address. The beams outgoing of all three DMDs and the imaging beam, go through the same microscope objective that has a numerical aperture of 0.45 and are focused on the atoms inside the glass cell. The light is collected by an identical microscope objective, a Charge-Coupled Device (CCD) camera (Chameleon) monitors the intensity of the green light in the atomic plane, while the PIXIS camera is used for absorption imaging of the cloud. An interference filter is placed in front of the camera that only lets light at $\lambda = 780\,\text{nm}$ through.

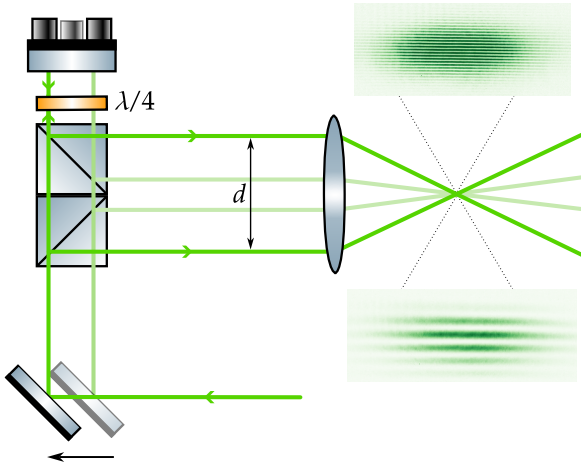

Figure 1.3: Layout of the vertical optical lattice with dynamical period. Two coherent parallel beams interfere at the focal plane of the lens where the atoms sit; the larger the distance d between the beams, the smaller the period of the lattice. The beams come from a single beam split in two by using two polarizing beam splitters. The mirror on top of the two beams is mounted on a piezoelectric actuator that allows us to translate the mirror slightly along the vertical direction in order to change the phase of the lattice. The mirror before the two beam splitters is placed on a motorized translation stage; by moving it, the distance between the two beams is changed. The two pictures displayed are taken by a camera imaging the light intensity in the atomic plane. The bottom one is taken when the lattice period is 13 µm. The atoms are loaded in a single node of this lattice before it is compressed by moving the translation stage to form a lattice that has a period of 3 µm, as captured in the top image.

1.2.3 Vertical confinement

To reach the 2D regime, we confine the atoms using a harmonic potential of frequency ω_z along the vertical direction with an energy spacing of its levels, $\hbar\omega_z$, large compared to the other energy scales. Specifically, the thermal energy: $\hbar\omega_z \gg k_B T$ and the interaction energy: $\hbar\omega_z \gg |\mu|$, where μ is the chemical potential. Under these conditions, the atoms will not populate the excited states of the potential and will remain in the ground state. The dynamics along the vertical direction are thus frozen. We are strictly speaking in the quasi-2D regime: kinematically the cloud is 2D, however, the extent of the cloud along z, $l_z = \sqrt{\hbar/m\omega_z} \approx 170\,\text{nm}$, is large compared to the scattering length, $a \approx 100\ a_0$ (with a_0 the Bohr radius), such that the interactions remain 3D.

Experimentally, we achieve this by loading our BEC in a single node of an optical lattice. The optical lattice is created by two coherent laser beams interfering in the plane of the atoms, as shown in fig. 1.3. Because the light is blue-detuned, the atoms will sit on a dark fringe of the lattice. To avoid loading any other nodes of the lattice, we need a period large compared to the size of the cloud. However, the frequency of the potential at the center of the fringe scales as $1/p_z$, the period of the lattice. Instead of finding a compromise, we use an optical lattice with a dynamical period [91]. The cloud is loaded in a lattice with a period $p_i \approx 13\,\mu\text{m}$, ensuring a single node is loaded. The period of the lattice is then adiabatically decreased, in 150 ms, to $p_f \approx 3\,\mu\text{m}$ for which we end up with a trap frequency $\omega_z \approx 2\pi \times 4\,\text{kHz}$.

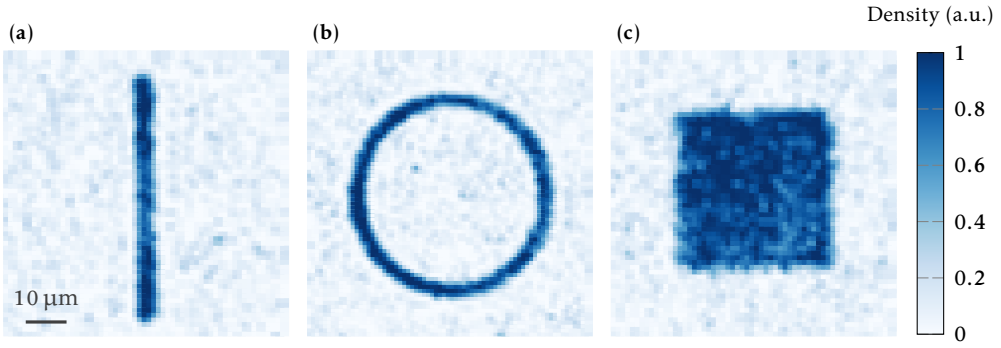

Figure 1.4: Absorption images of atoms in different trap geometries projected by DMD1, each image is obtained by averaging 10 realizations. These trap geometries are used for the experiments presented in this manuscript. (a), A tube of dimensions 60 µm × 3 µm. (b), A ring of outer radius 25 µm and a width of 3 µm. These two geometries are used in part I. (c), a square box of size 40 µm, this geometry is used in part II.

1.2.4 In-plane confinement

The optical lattice only confines the atoms vertically; an additional confinement in-plane is required to fully trap the atoms. This confinement is also done by light shaped by a DMD (Vialux V-7001) that we label DMD1, providing a very high versatility in the confinement geometry. The DMD can display any binary image of 1024×768 pixels on its rectangular array of micromirrors with a pitch size of 13.7 µm. The DMD chip is directly imaged on the atoms with a magnification of $\approx 1/70$, yielding an effective pixel size on the atoms of 0.2 µm. Following the transfer into this in-plane potential, we perform a final evaporative cooling stage, resulting in a two-dimensional quantum gas of $\approx 1 \times 10^5$ atoms at temperatures below 20 nK.

With blue-detuned light, the atoms are trapped in the dark regions, making it more convenient to make homogeneous traps than with red-detuned light. Examples of different trap geometries generated with DMD1 and used in the experiments presented in the next chapters are displayed in fig. 1.4. The DMD can also display movies with a refresh rate up to 23 kHz. This feature is particularly advantageous for the geometries in fig. 1.4b and fig. 1.4c: we initially load the atoms in a larger box trap, and then dynamically compress it to the desired final geometry. This compression procedure significantly increases the final atom number compared to direct loading into the target geometry.

1.2.5 In-plane optical potential

In addition to DMD1, a second DMD that we label DMD2, identical to DMD1, is present on the setup. This DMD is also used to project optical potentials on the atoms. The purpose of having these two devices is that the trap potentials projected by DMD1 and DMD2 are independent, as they are illuminated by separately controllable beams. This configuration allows the height of each potential to be varied independently by adjusting the incident light power on each DMD without changing the displayed image. DMD2 is used in chapter 5 to generate lattice potentials on the atoms.

To generate arbitrary potentials with a DMD, the procedure is the following. If the desired potential is of the form $V(x, y) = V_0 v(x, y)$ where v is a function taking dimensionless values, we have to imprint an intensity proportional to $v(x, y)$ in the atomic plane. Since the DMD chip can only display binary images (each pixel is either 0 or 1), we employ

the Floyd-Steinberg dithering algorithm [92] to approximate grayscale patterns. The optical transfer function of our imaging system naturally acts as a low-pass spatial filter, smoothing the binary pattern and yielding the desired continuous intensity profile at the atomic plane. In this way, the DMD acts as an amplitude modulator [93]. We thus dither the following function to obtain a binary image that we then load on the DMD:

$$\sqrt{A + Bv(x, y)}, \tag{1.4}$$

where the numerical coefficients A and $B > 0$ are chosen to keep the argument of the square root between 0.1 and 1, as the dithering algorithm requires an image with values between 0 and 1. A lower threshold of 0.1 is imposed to prevent the square root from approaching zero, to ensure the smoothness of the profile.

1.3 Controlling the internal atomic state

In this section we present the different tools we have in the experiment to control the internal state of the atoms.

1.3.1 MicroWave transfers and imaging

1.3.1.1 Controlling the internal state

As stated before the BEC is produced in the hyperfine state $|F = 1, m_F = -1\rangle$. We can subsequently transfer the atoms to other hyperfine states using a MW field. The signal from a microwave signal generator is amplified and sent to an antenna. In this way we can perform π, σ^+ and σ^- transitions between the $F = 1$ and $F = 2$ manifolds with a typical Rabi frequency of $\Omega_R \approx 2\pi \times 20\,\text{kHz}$. Starting from $|F = 1, m_F = -1\rangle$, all the 8 states of the $5^2S_{1/2}$ manifold can be reached, by doing one or several successive MW transfers.

1.3.1.2 Partial-transfer absorption imaging

MW transfers are systematically used when imaging the cloud. Almost all results presented in this thesis were obtained using *in-situ* absorption images. For samples as dense as BECs, the Beer-Lambert law does not apply, thus *in-situ* absorption imaging of the cloud is rarely used in BEC experiments. To give an order of magnitude, *in-situ* absorption imaging of our cloud with a typical density of $50\,\mu\text{m}^{-2}$ would lead to an optical density of approximately 7. Absorption images are typically taken after a Time of Flight (ToF), the sample is then more dilute. To image a BEC *in-situ*, we use a technique called partial-transfer absorption imaging [94].

All experiments conducted in this manuscript were performed with atoms in the $F = 1$ manifold. To image the cloud, we use a laser beam resonant with the $|F = 2\rangle \rightarrow |F = 3\rangle$ transition of the $D2$ line. We transfer a small fraction of the atoms from the $F = 1$ to the $F = 2$ manifold and immediately image them afterward. This fraction must be sufficiently small such that the density of atoms in $F = 2$ remains in the regime where the Beer-Lambert law is applicable. In this case, the 2D density can be deduced from the optical density profile, $OD(x, y)$:

$$n_{F=2}(x, y) = \frac{OD(x, y)}{\sigma_0}, \tag{1.5}$$

where σ_0 is the scattering cross-section for the $|F = 2\rangle \rightarrow |F = 3\rangle$ transition. If we know the Rabi frequency of the MW pulse and its duration, the total initial density profile can

be reconstructed. In the case of a resonant MW transfer, we have:

$$n(x,y) = \frac{n_{F=2}(x,y)}{\sin^2(\Omega_R t_p/2)}, \tag{1.6}$$

where t_p is the duration of the MW pulse. The Rabi frequency can be measured precisely by performing Rabi oscillations. The pulse duration is shorter than $\pi/\Omega_R \sim 50\,\mu s$, which is too brief for any atomic motion to occur, thus ensuring we capture an *in-situ* image. With this technique, we can image our cloud *in-situ* across a wide range of densities.

Equation (1.5) is valid when the imaging is not saturated. Furthermore, to know the precise value of σ_0, one must know the exact polarization of the imaging beam. To accurately calibrate the imaging system, we assume that the density is proportional to the optical density as in eq. (1.5), but with an additional factor, $\mathcal{F}$, that is calibrated experimentally:

$$n_{F=2}(x,y) = \mathcal{F}\frac{OD(x,y)}{\sigma_0}, \tag{1.7}$$

To calibrate this factor, we primarily employ two techniques. The density can be measured using the density-dependent frequency shift of the clock transition $|F=1, m_F=0\rangle \rightarrow |F=2, m_F=0\rangle$. This shift, on the order of 10 Hz for the typical densities of our samples, is measured via Ramsey spectroscopy. The density can also be measured by measuring the speed of the sound given by $c = \sqrt{gn/m}$. The protocol used for this measurement is detailed in chapter 5.

1.3.1.3 Precise control of atomic density

The same microwave transfer procedure employed for partial-transfer imaging can also be used for precise control of the cloud density. The density can be reduced to a predetermined value through a two-step process. First, we transfer the excess atoms from the $F = 1$ to the $F = 2$ manifold using a microwave pulse. Second, we selectively remove these atoms in the $F = 2$ state by applying the same resonant imaging beam used for absorption imaging. The atoms remaining in the $F = 1$ manifold are unaffected by this beam, resulting in a cloud with precisely controlled density.

1.3.2 Raman transfers

We can transfer the atoms to different hyperfine states using MW fields; however, their wavelength is of the order of the cm making it impossible to do this transfer in a spatially resolved way. For that, we rely on lasers and perform two-photon transfers. We have a pair of coherent beams that have a frequency difference of the order of the hyperfine splitting. By adjusting the frequency difference between the two beams, we can do coherent two-photon transitions between a state of the $F = 1$ manifold and a state of the $F = 2$ manifold. In our setup the maximal Rabi frequency of this transfer is of the same order magnitude as the one of the MW transfer. The wavelength of the laser is tuned between the $D1$ and $D2$ to the tune-out wavelength [83]. This wavelength is defined as the wavelength at which the contribution of the $D1$ and $D2$ lines cancel each other so that the total light shift of the electronic ground state is zero. Thus, no modification of the phase occurs during the transfer. The two Raman beams are coupled into the same optical fiber, ensuring they are perfectly superimposed at the output of the fiber. With this configuration, no momentum is transferred to the atoms during a Raman transition. The two copropagating beams are then shaped using a DMD labelled DMD3; it is imaged on the plane of the atoms

with a magnification of 1/30, yielding an effective pixel size of 0.45 µm. We now describe how we transfer atoms, in a spatially resolved way, between two Zeeman states, $|i\rangle$, $|f\rangle$, lying in different hyperfine manifolds. We suppose that the intensity profiles of the two Raman beams on the atoms are respectively $I_1 s(x,y)$, $I_2 s(x,y)$, where the function s has dimensionless values and describes the shape of the profile. The shape is the same for the two beams as they are superimposed. The fraction of atoms transferred to state $|f\rangle$ is:

$$r(x,y) = \sin^2(\Omega_R(x,y)t_p/2), \tag{1.8}$$

where t_p is the duration of the pulse and the Rabi frequency $\Omega_R(x,y) \propto \sqrt{I_1 I_2}s(x,y)$. If we want to have a fraction of atoms in component $|f\rangle$ given by $r(x,y)$ we have to dither the following profile and imprint it on DMD3:

$$f(x,y) = \sqrt{\frac{2}{\pi}\arcsin\left(\sqrt{r(x,y)}\right)}. \tag{1.9}$$

1.4 Control of the magnetic field

In the work presented in this thesis we rely on magnetic field gradients to exert forces on atoms in a magnetic field sensitive state. For magnetic fields low enough to generate a splitting small compared to the hyperfine energy (which is always the case in this work), the magnetic field creates the following potential for the atoms[1]:

$$V_{\text{mag}}(x,y,z) = g_F m_F \mu_B B(x,y,z), \tag{1.10}$$

where g_F and m_F are respectively the Landé factor and magnetic quantum number of the state considered, μ_B is the Bohr magneton and B is the norm of the magnetic field. To control the magnetic field, we have bias coils along the three directions of space, generating uniform fields at the position of the atoms. Furthermore, the MOT coils can generate a quadrupolar field at the position of the atoms. Assuming the origin is at the center of the cloud, the magnetic field seen by the atoms reads:

$$\mathbf{B}(x,y,z) = (B_z + b_z z)\mathbf{e}_z + (B_x + b_x x)\mathbf{e}_x + (B_y + b_y y)\mathbf{e}_y, \tag{1.11}$$

where the three bias fields B_i are controllable independently but not the three gradients b_i. We also assume that along every direction $b_i l_i \ll B_0 = \sqrt{B_x^2 + B_y^2 + B_z^2}$, where l_i is the extent of the cloud along direction i. If we expand the magnetic field norm to first order, we have:

$$B(x,y,z) \approx B_0 + \frac{b_x x B_x}{B_0} + \frac{b_y y B_y}{B_0} + \frac{b_z z B_z}{B_0}. \tag{1.12}$$

In the experiment we usually choose a quantization axis along which the bias field is significantly larger than along the other directions; it is usually z. The previous equation can then be written:

$$B(x,y,z) \approx B_z + \frac{b_x x B_x}{B_z} + \frac{b_y y B_y}{B_z} + b_z z. \tag{1.13}$$

[1]This is true as long as the magnetic field, in the reference frame of the moving atom, rotates slowly compared to the Larmor frequency, such that the spin remains aligned with the field.

Using eq. (1.10) we deduce that the magnetic field exerts a force with an in-plane component given by:

$$\mathbf{F}_{/\!/} = -g_F m_F \mu_B \left(\frac{b_x B_x}{B_z} \mathbf{e}_x + \frac{b_y B_y}{B_z} \mathbf{e}_y \right). \tag{1.14}$$

The potential along the z direction does not affect the cloud as it is much smaller than the potential of the vertical optical lattice. To control the force created by the magnetic field, we usually fix the value of the gradients b_x, b_y, b_z by fixing the current circulating in the MOT coils. The orientation and magnitude of the force is then varied by adjusting the bias fields B_x and B_y that can be independently controlled by changing the currents in the different coils. The force given by eq. (1.14) is calibrated using Ramsey interferometry as detailed in [86].

Conclusion

In this chapter, we have described our experimental apparatus for producing and studying two-dimensional ^{87}Rb Bose-Einstein condensates. We began with an overview of our 3D BEC production sequence, which follows well-established cooling protocols to produce a degenerate quantum gas with approximately 5×10^5 atoms.

We then detailed our approach to dimensionality reduction, focusing on the vertical optical lattice that strongly confines atoms along one axis with a dynamically adjustable period. This confinement, combined with our versatile in-plane trapping potentials shaped by DMD1, enables the creation of two-dimensional quantum gases in various geometries such as tubes, rings, and square boxes. Additionally, DMD2 can project potential landscapes with depths independently controlled from the main trapping potential.

We presented our methods for controlling the internal state of the atoms, either globally using MW fields or with spatial resolution using Raman beams. These techniques are essential for our partial-transfer absorption imaging protocol, which allows for *in-situ* measurements of high-density condensates without time-of-flight expansion.

Finally, we explained our magnetic field control system, which enables the application of calibrated forces on atoms in magnetic-sensitive states through precisely controlled field gradients.

Having described the experimental tools necessary for understanding our work, we will proceed in the subsequent chapters to present the experiments performed with this apparatus.

Part I

Solitons

CHAPTER 2

Solitons in the static regime

Outline of the current chapter

Introduction

This chapter introduces the concept of solitons, focusing on their theoretical description and experimental realizations in ultracold quantum gases. We begin by a short definition of the concept of solitary waves and solitons (section 2.1). We then explore one-component matter-wave solitons governed by the Gross-Pitaevskii equation (section 2.2), including bright solitons in the attractive case and dark solitons in the repulsive case. We then extend our analysis to two-component systems (section 2.3), discussing vector solitons in the Manakov limit and beyond, including dark-bright and dark-dark solitons. Finally, we introduce magnetic solitons, which are at the heart of our experimental work. Throughout the chapter, we connect theoretical descriptions with experimental implementations, culminating with our realization of a magnetic soliton at rest in a flat-bottom trap. This provides the foundation for understanding the dynamics of magnetic solitons which will be the focus of the following chapter.

2.1 Solitary waves and solitons

2.1.1 What is a soliton ?

Providing a comprehensive and mathematically rigorous definition of a soliton represents a significant challenge. However, we can establish a conceptual framework by examining a fundamental case. We begin our analysis with a very well-known problem, namely the one-dimensional Schrödinger equation, that reads in dimensionless form

$$\mathrm{i}\frac{\partial\psi}{\partial t} = -\frac{1}{2}\frac{\partial^2\psi}{\partial x^2}. \tag{2.1}$$

It is well known that if the initial condition is a localized wave packet, meaning that $\psi(x,0)$ approaches a constant at infinity, then it will spread out spatially due to the kinetic energy dispersive term $-\frac{\partial^2 .}{\partial x^2}$ and its peak norm will go to zero. These types of solutions are called radiative. If we add a cubic nonlinearity to the previous equation, we obtain the attractive GPE

$$\mathrm{i}\frac{\partial\psi}{\partial t} = -\frac{1}{2}\frac{\partial^2\psi}{\partial x^2} - |\psi|^2\psi, \tag{2.2}$$

The nonlinear term $-|\psi|^2\psi$ has a focusing effect on the wave packet that has the opposite effect of the dispersive term. The equation still has radiative solutions, but by choosing the right initial condition, we can make these two effects balance each other and obtain a solution that stays localized in space and can propagate while conserving its shape [79]

$$\psi(x,t) = \frac{\alpha\exp\left(\mathrm{i}\left(vx - \frac{t}{2}(\alpha^2 - v^2)\right)\right)}{\cosh(\alpha(x-vt))}, \tag{2.3}$$

where $1/\alpha$ is the width of the wave packet, and v its speed. These types of solutions are called solitary waves. Equation (2.3) describes a situation where the shape of the envelope $|\psi(x,t)|^2$ does not change over time. Not all solitary waves have this feature. As pointed out in ref. [79], some solitary waves, called breathers, have an oscillatory behavior of the envelope; they stay, however, localized in space. In the case of the 1D attractive GPE, the Kuznetsov-Ma breather is an example of such a solution [95, 96]. The attractive GPE serves as an illustrative example, but solitary waves can be found in many different nonlinear PDEs including the Korteweg-de Vries equation [97], the Landau-Lifshitz Equation

(LLE) [98, 99], and the sine-Gordon equation [100, 101]. However, not all solitary waves are solitons. The latter have the additional property of conserving their shape and speed when interacting with other solitons or radiative solutions [78, 102]. They can, in a sense, only interact "elastically". However, in the literature, the term soliton is often used to refer to any solitary wave, and this meaning will be adopted in this manuscript.

2.1.2 Soliton resolution

Solitons play a pivotal role in the resolution of nonlinear dispersive PDEs. Indeed, if one sets as an initial condition of the 1D attractive GPE a smooth and localized arbitrary function, the time evolution leads to a radiative part (that spreads out spatially), whose peak amplitude goes to zero, and a finite number (possibly zero) of solitons moving at different speeds. This property is called soliton resolution. In the case of eq. (2.2), this property is justified through the inverse scattering approach [103, 104], that proves that the GPE is integrable. We can thus think of solitons as generalized Fourier modes of dispersive non-linear PDEs. The 1D attractive GPE, can be extended to a more general equation namely the non-linear Schrödinger equation in dimension d:

$$\mathrm{i}\frac{\partial\psi}{\partial t} = -\frac{1}{2}\nabla^2\psi - |\psi|^p\psi, \tag{2.4}$$

where $\psi : \mathbb{R}^d \times \mathbb{R} \longrightarrow \mathbb{C}$ and $p, d \in \mathbb{N}$. In this general case, however, the equation is not necessarily integrable, and the soliton resolution remains a conjecture, as pointed out in ref. [105].

2.2 One-component matter-wave solitons

2.2.1 The scalar Gross-Pitaevskii Equation

We now examine solitons of the 1D GPE that describes a weakly-interacting BEC at zero temperature in the mean-field regime:

$$\mathrm{i}\hbar\frac{\partial\psi}{\partial t} = -\frac{\hbar^2}{2m}\frac{\partial^2\psi}{\partial x^2} + g|\psi|^2\psi, \tag{2.5}$$

where g is the interaction parameter, and ψ is normalized such that $\int |\psi|^2 \mathrm{d}x = N$ the number of particles. The parameter g is positive (resp. negative) when the interactions are repulsive (resp. attractive). Equation (2.5) is also notably used to describe the electric field for the propagation of a light pulse in an optical fiber with Kerr nonlinearity [106], with the difference that t plays the role of the longitudinal coordinate and x the role of time. Fiber optics has been a very fruitful field for experimental observations of solitons [107–112]; however, in the following, we will focus solely on matter-wave solitons realized with cold atoms. The equation can be solved by the inverse scattering method; it is thus integrable [104]. However, in the vast majority of cold-atom experiments, a harmonic potential is present that breaks integrability.

The study of solitons in Bose gases also extends beyond the mean-field regime, where additional quantum effects become relevant [113, 114], however it is beyond the scope of this manuscript.

2.2.2 Attractive case

2.2.2.1 Bright soliton description

In the attractive case ($g < 0$), an example of a soliton was previously presented in eq. (2.3); this solution is called a bright soliton. We start with the bright soliton at rest [115]

$$\Psi_{b,v=0}(x,t) = \frac{\psi_0}{\cosh(\kappa x)} \mathrm{e}^{-\mathrm{i}\Omega t} \tag{2.6}$$
$$\text{where} \quad \kappa = \frac{mN|g|}{2\hbar^2}, \quad \psi_0^2 = \frac{\kappa N}{2}, \quad \hbar\Omega = -\frac{mg^2N^2}{8\hbar^2}.$$

$\Psi_{b,v=0}(x,t)$ is normalized to the number of particles N. The chemical potential μ is given by $\mu = \hbar\Omega$. The whole class of propagating bright solitons can be generated using the Galilean invariance of eq. (2.5):

$$\Psi_{b,v}(x,t) = \Psi_{b,v=0}(x - vt, t)\, \mathrm{e}^{\mathrm{i}\frac{m}{\hbar}(vx - \frac{v^2}{2}t)}, \tag{2.7}$$

where v is the speed of the soliton. The bright soliton has a vanishing background density. We can treat the soliton as a semi-classical particle and associate an energy and momentum with it:

$$p = -\mathrm{i}\hbar \int \mathrm{d}x\, \Psi^*_{b,v} \frac{\partial \Psi_{b,v}}{\partial x} = Nmv \tag{2.8a}$$
$$E(N,p) = \mathcal{E}[\Psi_{b,v}] = \int \mathrm{d}x\, \frac{\hbar^2}{2m}\left|\frac{\partial \Psi_{b,v}}{\partial x}\right|^2 + \frac{g}{2}|\Psi_{b,v}|^4 - \mu|\Psi_{b,v}|^2 = \frac{mg^3N^3}{12\hbar^2} + \frac{p^2}{2Nm}. \tag{2.8b}$$

Its behavior corresponds to that of a classical particle; if a force f is applied to a bright soliton at rest, its Center-of-Mass (CoM) position evolves as $x(t) = ft^2/2m$.

2.2.2.2 Experimental realizations

Bright solitons were first observed experimentally using ^{7}Li [116, 117], followed by numerous subsequent realizations [118–127]. In these experiments, a BEC with repulsive interactions is prepared in an anisotropic trap with loose longitudinal confinement and tight radial confinement, referred to as a cigar-shaped trap. The interactions are then transformed from repulsive to attractive by using a Feshbach resonance, leading to the formation of one [116, 118, 120, 122, 124–127] or several [117, 119, 121, 123, 124] bright solitons.

These experimental realizations differ from ideal bright solitons of the 1D GPE for several fundamental reasons. First, the presence of an axial harmonic potential modifies eq. (2.5). As demonstrated in ref. [128], the trapping axial potential stabilizes the soliton and increases its energy gap with respect to non-solitonic states, enhancing its robustness against, for example, thermal effects. A harmonic potential also enables the creation of 3D solitary waves, which cannot exist in its absence [129]. Second, residual 3D effects influence the nature of collisions; integrability is broken and collisions between solitons are no longer elastic [130]. These effects were particularly evident in ref. [116]. Experiments have also demonstrated superpositions of two [125] and three [127] solitons. When each soliton contains the appropriate number of atoms, they maintain zero relative velocity and form a breather. These solutions are detailed in ref. [131].

Additionally, bright solitons have been observed in gases with repulsive interactions.

This is achieved by placing the gas in a weak optical lattice and preparing it at the band edge where the effective mass becomes negative [132]. These solitons are called bright gap solitons.

2.2.3 Repulsive case

2.2.3.1 Dark soliton description

In the repulsive case, solitons with vanishing background density do not exist ; they are only possible with non-vanishing background densities. One example of such a soliton is the dark soliton, which manifests as a density dip over a uniform density background [80, 133]:

$$\Psi_{d,v}(x,t) = \sqrt{n_0}\left[\mathrm{i}\frac{v}{c} + \sqrt{1-\frac{v^2}{c^2}}\tanh\left(\frac{(x-vt)}{\eta}\sqrt{1-\frac{v^2}{c^2}}\right)\right]\mathrm{e}^{-\mathrm{i}\mu t/\hbar} \tag{2.9a}$$

$$\text{with}\quad \eta = \frac{\hbar}{\sqrt{mgn_0}},\quad \mu = gn_0,\quad c = \sqrt{\frac{gn_0}{m}}, \tag{2.9b}$$

where n_0 is the background density, v is the speed of the soliton, c is the speed of sound, μ is the chemical potential. We also define $\xi = \eta/\sqrt{2}$, the healing length of the condensate.

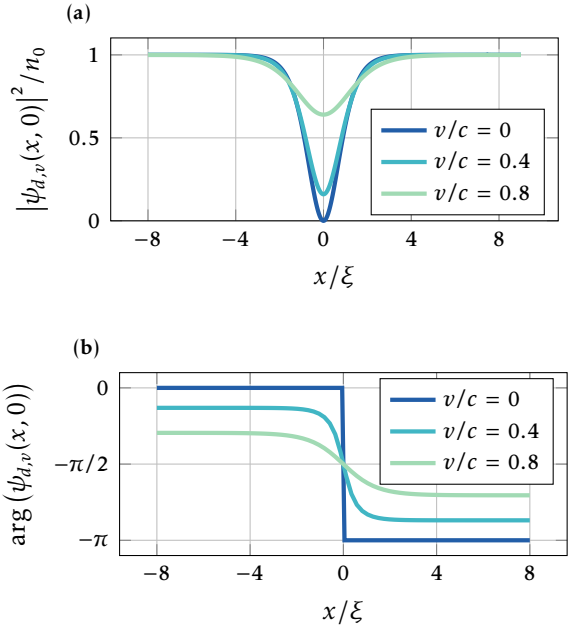

Figure 2.1: Profiles of dark solitons at different speeds. (a), modulus squared and (b), argument of the wave function.

In fig. 2.1, we present the modulus squared and argument of $\psi_{d,v}$ for different speeds. Unlike the bright soliton, the class of dark solitons cannot be generated by Galilean transformations, as these transformations do not affect the speed of the density dip relative to the background. When $v = 0$, the density depletion (the fraction of atoms missing at the center of the soliton) is complete, and the wave function undergoes a sign change. This sign change manifests as a $\pm\pi$ phase jump across the center of the soliton. As the speed of the soliton approaches c, the depletion diminishes. In the limit $v \to c$, the soliton evolves into a flat-density profile, corresponding to the ground state of eq. (2.5). We point

out to the reader that some of the literature terms the solutions given in eq. (2.9) as "gray solitons", while "dark solitons" is preferred for solitons exhibiting a full depletion (*i.e.*, $v = 0$). This convention is not the one followed here, and we will use the term "dark soliton" without distinction throughout this work.

2.2.3.2 Experimental realizations

Similar to bright solitons, all experimental realizations of dark solitons have been conducted in elongated harmonic traps. The first realizations of dark solitons employed a technique called phase imprinting, which involves imprinting a specific phase on the BEC without manipulating its density profile. This technique was first demonstrated with ^{87}Rb [134] and ^{23}Na [135], and was subsequently employed in later studies [136, 137]. For phase imprinting, a far off-resonant laser beam is briefly directed at the BEC to avoid spontaneous emission. The laser beam generates a potential $V(x)$, inducing a light-shift on the cloud given by $\exp(it_pV(x)/\hbar)$, where t_p represents the pulse duration. When $t_p \ll \mu/\hbar$, atomic motion can be neglected during the pulse duration, preventing any density changes. To generate a dark soliton, half of the cloud is illuminated with the laser pulse, creating a phase shift between the two halves. One might initially conclude that imprinting only a phase jump is insufficient to generate a soliton and that the full wave function of eq. (2.11) must be imprinted on the BEC. However, as discussed in section 2.1.2, solitons and radiative solutions are the equivalent of generalized Fourier modes. Therefore, it is not surprising that with the appropriate initial conditions, the system evolves after some time to a state containing solitons. Indeed, as shown in ref. [138], imprinting a phase step function of amplitude $\Delta\phi$ results in the production of a single dark soliton with $v/c = \cos(\Delta\phi/2)$. However, due to finite optical resolution, one cannot imprint a discontinuous phase jump, but only a rapidly varying phase profile. A consequence of this limitation is the generation of several solitons, as demonstrated in ref. [138]. This effect was indeed observed in ref. [134, 135]. Another consequence is that there is a minimal speed for solitons produced with phase imprinting [139]. More broadly, phase imprinting has also been used to generate dark solitons in ultracold fermions [140], enabling the study of their behavior across the Bardeen–Cooper–Schrieffer to the Bose-Einstein Condensate crossover. In ref. [139], the authors improved the protocol. In addition to phase imprinting, they employed another far-detuned laser pulse, applied over a longer duration, to shape their cloud's density. This approach achieved full control over the initial wave function, limited only by the optical resolution of the experiment. As demonstrated through simulations in ref. [141], a discontinuous phase jump is not necessary to generate solitons at arbitrarily low velocities, provided one has control over the density profile. Indeed, in ref. [139], they successfully created solitons with zero velocity by controlling both the phase and the density profile of the cloud.

Other techniques can be used to generate dark solitons without requiring phase-engineering of the wave function. Placing a barrier in the middle of the condensate and then removing it can generate dark solitons, as demonstrated in ref. [142–144]. This technique, however, always generates more than one soliton. Finally, solitons can also form spontaneously without any manipulation of the wave function, appearing as defects caused by the Kibble-Zurek mechanism [145, 146].

2.2.3.3 Dark soliton characteristics

Deriving the energy and momentum of the dark soliton is more involved than for the bright soliton. The energy of the dark soliton can be defined as the energy difference

between the presence and absence of the soliton:

$$E(v) = \mathcal{E}[\Psi_{d,v}] - \mathcal{E}[\sqrt{n_0}], \tag{2.10}$$

where $\mathcal{E}$ is the Gross-Pitaevskii (GP) free energy functional defined in eq. (2.8b). However, as pointed out by Shevchenko [147], this naive approach does not yield the correct result, as also discussed by Pitaevskii in ref. [148]. The reason is that both n_0 and $\Psi_{d,v}$ are solutions of the GPE but with different boundary conditions. The solution with uniform density n_0 satisfies periodic boundary conditions, whereas eq. (2.9) satisfies twisted boundary conditions, meaning the phase at $\pm L/2$ differ.

To recover periodic boundary conditions in the presence of the soliton, the bath needs to acquire a velocity that will generate a phase gradient capable of compensating the phase variation near the center of the soliton. This movement of the bath is called backflow, as it flows in the opposite direction of the current generated by the soliton. The backflow can be found by using a Galilean transformation, resulting in a change of reference frame to one moving at velocity u with respect to the lab frame. The soliton wave function becomes:

$$\tilde{\Psi}_{d,v}(x,t) = \Psi_{d,v}(x-ut,t)\, \mathrm{e}^{\mathrm{i}\left(\frac{mu}{\hbar}x - \frac{mu^2}{2\hbar}t\right)}, \tag{2.11}$$

where we choose u such that $\arg\left(\tilde{\Psi}_{d,v}(L/2,t)\right) = \arg\left(\tilde{\Psi}_{d,v}(-L/2,t)\right) + 2\pi w$, where w is an integer and L is the size of the system. In the case $\xi \ll L$,

$$\arg\left(\tilde{\Psi}_{d,v}(L/2,0)\right) - \arg\left(\tilde{\Psi}_{d,v}(-L/2,0)\right) = 2\arctan\left(\frac{v}{c\sqrt{1-\frac{v^2}{c^2}}}\right) - \pi\,\mathrm{sign}(v) + \frac{muL}{\hbar}, \tag{2.12}$$

where we choose the convention that the phase jump is negative for $v = 0^+$. Therefore, the speed u is given by:

$$u = \frac{h}{mL}\left(w - \frac{1}{\pi}\arcsin\left(\frac{v}{c}\right) + \frac{1}{2}\,\mathrm{sign}(v)\right). \tag{2.13}$$

To compute the energy and momentum, we use $\int \mathrm{d}x \left|\Psi_{d,v}\right|^2 = n_0 L + N_d$ where:

$$N_d = -2n_0\eta\sqrt{1-\frac{v^2}{c^2}} = -\frac{2\hbar}{g\sqrt{m}}\sqrt{\mu - mv^2}, \tag{2.14}$$

is the number of particles missing due to the presence of the soliton. The energy of $\Psi_{d,v}$ is given by [80]:

$$E(v) = \mathcal{E}[\Psi_{d,v}] - \mathcal{E}[\sqrt{n_0}] = \frac{4}{3}\frac{\hbar}{\sqrt{m}g}\left(\mu - mv^2\right)^{3/2} = -\frac{mg^2N_d^3}{6\hbar^2}. \tag{2.15}$$

From this, we can deduce the energy of the dark soliton:

$$E'(v) = \mathcal{E}[\tilde{\Psi}_{d,v}] - \mathcal{E}[\sqrt{n_0}] = -\frac{mg^2N_d^3}{6\hbar^2} + \frac{u^2}{2}N_d. \tag{2.16}$$

In the equation above, we used the fact that $\int \mathrm{d}x\, \partial_x \left|\Psi_{d,v}\right|^2 = 0$. The momentum of the dark

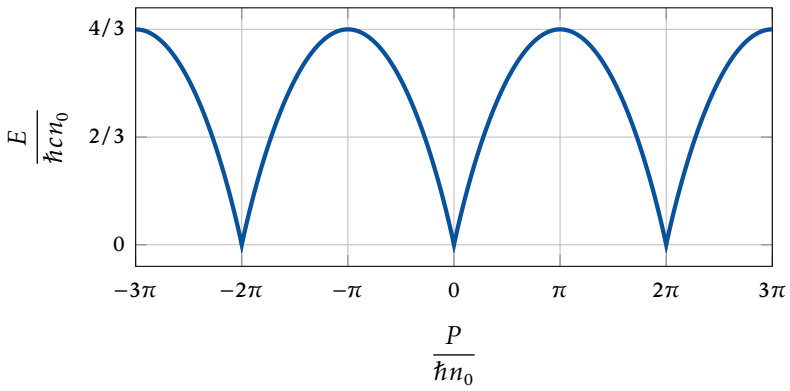

Figure 2.2: Dispersion relation of the dark soliton in the thermodynamic limit.

soliton is given by:

$$P_f = -\mathrm{i}\hbar \int \mathrm{d}x\, \tilde{\Psi}^*_{d,v} \partial_x \tilde{\Psi}_{d,v} = \hbar n_0 \left[2\pi w - 2\frac{v}{c}\sqrt{1-\frac{v^2}{c^2}} + \pi\,\mathrm{sign}(v) - 2\arcsin\left(\frac{v}{c}\right)\right] + N_d m u. \tag{2.17}$$

Taking the thermodynamic limit, i.e., $L \to \infty$ with n_0 constant in eq. (2.13) yields $u \to 0$. Both second terms of the right-hand-side (rhs) of eq. (2.17) and eq. (2.16) thus vanish. The latter, represents the energy of the backflow generated by the soliton. Consequently, the energy of the dark soliton in the thermodynamic limit is given by eq. (2.15) and the momentum by

$$P = \hbar n_0 \left[2\pi w - 2\frac{v}{c}\sqrt{1-\frac{v^2}{c^2}} + \pi\,\mathrm{sign}(v) - 2\arcsin\left(\frac{v}{c}\right)\right]. \tag{2.18}$$

One can verify that the momentum defined in eq. (2.18) corresponds to the canonical momentum of the soliton $v = \left(\partial E/\partial P\right)_\mu$. We notice that in the definition of the momentum there is an integer w that is not present in the energy. This suggests that solitons with momentum P and $P + hn_0$ have the same energy. While we could not find an analytical formula for $E(P)$, we computed it numerically and plotted it in fig. 2.2, where the periodicity is clearly visible. This is a more general property of 1D systems that we will discuss in section 3.5.2. The soliton at rest has a momentum $P/\hbar = \pi\hbar n_0(2k+1)$ where $k \in \mathbb{Z}$ and its energy is maximal. Conversely, when the soliton speed approaches c, the energy becomes minimal.

The dispersion relation of the dark soliton is concave, meaning the effective mass of the soliton:

$$m_{\mathrm{eff}} = \left(\frac{\partial^2 E}{\partial P^2}\right)^{-1} = \frac{1}{v}\left(\frac{\partial E}{\partial v}\right), \tag{2.19}$$

is negative, as confirmed by [149]:

$$m_{\mathrm{eff}} = 2mN_d = -4mn_0\eta\sqrt{1-\frac{v^2}{c^2}}. \tag{2.20}$$

2.3 Two-component matter-wave solitons

2.3.1 The vector Gross-Pitaevskii Equation

2.3.1.1 Miscibility of spin mixtures

We now consider a two-component BEC, i.e. a BEC composed of a single atomic species but with different internal states $|1\rangle$ and $|2\rangle$. We assume there are no processes that can transfer atoms from one component to the other (in the case of a spin-mixture, this means no spin-exchange collisions). In the mean field regime, the system is described by two coupled GPEs:

$$i\hbar\frac{\partial\psi_1}{\partial t} = -\frac{\hbar^2}{2m}\frac{\partial^2\psi_1}{\partial x^2} + g_1 n_1\psi_1 + g_{1,2}n_2\psi_1 \tag{2.21a}$$

$$i\hbar\frac{\partial\psi_2}{\partial t} = -\frac{\hbar^2}{2m}\frac{\partial^2\psi_2}{\partial x^2} + g_2 n_2\psi_2 + g_{1,2}n_1\psi_2, \tag{2.21b}$$

where g_1, g_2 are the intracomponent interaction parameters, $g_{1,2}$ is the intercomponent interaction parameter, and $n_i = |\psi_i|^2$. We also define $N_i = \int \mathrm{d}x\, |\psi_i(x,t)|^2$, the number of atoms in each component and $n_0 = n_1 + n_2$, the total density.

The relative values of the interaction parameters determine the miscibility degree of the two species. The miscibility parameter is given by [150]:

$$\Delta = g_1 g_2 - g_{1,2}^2. \tag{2.22}$$

For $\Delta > 0$ (resp. $\Delta < 0$) the mixture is miscible (resp. immiscible). The case of equal interaction parameters, $g_1 = g_2 = g_{1,2}$, is called the Manakov limit, or SU(2) point. Unlike the one-component case, the two-component GPE is not integrable in the general case. However, it is integrable in the Manakov limit [151].

2.3.1.2 Effective one-component description

We will show in this subsection that near the Manakov limit, in the low depletion regime (i.e., $n_2(x)/n_1(x) \ll 1$ without loss of generality), the two-component BEC can be described, in the static case, by an effective one-component GPE [84, 152].

We begin with the assumption that the interaction parameters are close to the Manakov limit, where the total density undergoes only weak perturbations in the regime of low-energy dynamics: $n_1(x) + n_2(x) = n_\infty + \delta n(x)$, with $\delta n \ll n_\infty$. This will be explained in detail in section 2.3.3.2. The coupled GPEs of the static system are:

$$\mu_1\psi_1 = -\frac{\hbar^2}{2m}\frac{\partial^2\psi_1}{\partial x^2} + g_1 n_1\psi_1 + g_{1,2}n_2\psi_1 \tag{2.23a}$$

$$\mu_2\psi_2 = -\frac{\hbar^2}{2m}\frac{\partial^2\psi_2}{\partial x^2} + g_2 n_2\psi_2 + g_{1,2}n_1\psi_2, \tag{2.23b}$$

with μ_1, μ_2 the chemical potentials. We now suppose that component $|2\rangle$ is localized in space. Thus, the chemical potential of $|1\rangle$ is $\mu_1 = g_1 n_\infty$. Near the Manakov limit, if the initial spatial variations of ψ_1 and ψ_2 occur at a scale much larger than the healing length, they will remain so during the dynamics [150]. In this regime, the kinetic terms $\frac{\hbar^2}{2m}\partial_x^2\cdot$ can be treated as order 1, such that $\partial_x^2\psi_1$ can be replaced by $\partial_x^2\sqrt{n_\infty - n_2}$ (assuming a

real-valued function). Equation (2.23a) then becomes:

$$g_1 \delta n = \frac{\hbar^2}{2m\sqrt{n_\infty - n_2}} \frac{\partial^2 \sqrt{n_\infty - n_2}}{\partial x^2} + (g_1 - g_{1,2}) n_2. \tag{2.24}$$

Substituting the previous expression in eq. (2.23b) yields:

$$\left(\mu_2 - g_{1,2} n_\infty\right) \psi_2 = -\frac{\hbar^2}{2m} \frac{\partial^2 \psi_2}{\partial x^2} + g_e \psi_2^3 + \frac{\hbar^2}{2m\sqrt{n_\infty - n_2}} \frac{\partial^2 \sqrt{n_\infty - n_2}}{\partial x^2} \psi_2, \tag{2.25}$$

where $g_e = g_2 - g_{1,2}^2/g_1 = -\Delta/g_1$ is the effective interaction. Thus, if $g_1 > 0$, a miscible (resp. immiscible) mixture yields an effective repulsive (resp. attractive) interaction.

Up until now there was no assumption on the depletion of $|1\rangle$. If we add to the previous assumption that the depletion is negligible, *i.e.* $n_2/n_\infty \ll 1$, at minimal order in the previous quantity we obtain:

$$\mu_e \psi_2 = -\frac{\hbar^2}{2m} \frac{\partial^2 \psi_2}{\partial x^2} + g_e \left|\psi_2\right|^2 \psi_2, \tag{2.26}$$

where $\mu_e = \mu_2 - g_{1,2} n_\infty$ is the effective chemical potential. In the case of the one-component GPE, we saw that the characteristic length scale is the healing length, which with common densities is smaller than 0.5 µm. This makes it very difficult to perform precise phase or density engineering as well as to image the cloud in-situ. By working with the effective one-component system of eq. (2.26), the relevant length scale becomes the spin healing length $\xi_s = \hbar/\sqrt{2m g_e n_0}$. Near the Manakov limit $g_e \ll g_1, g_2, g_{1,2}$, the spin healing length is much larger than the healing length, $\approx \times 10$ in ref. [152] (which allowed us to treat the $\partial_x^2 \cdot$ as a low order term). Therefore, it is a much more convenient length scale for experiments. While the effective one-component description is useful in certain regimes, we will now focus on solitonic solutions that genuinely require a two-component description and cannot be reduced to a single-component model.

2.3.2 Bright and dark vector solitons

2.3.2.1 Vector solitons in the Manakov limit

We consider eq. (2.21) in the repulsive Manakov limit, we define $g = g_1 = g_2 = g_{1,2} > 0$ as the interaction parameter. We describe here solitonic solutions with a non-vanishing background density.

Dark-bright soliton We start with the dark-bright soliton [153, 154]:

$$\psi_1(x,t) = \sqrt{n_0} \left\{ \mathrm{i} \sin(\alpha) + \cos(\alpha) \tanh\left[\kappa (x - vt)\right] \right\} \mathrm{e}^{-\mathrm{i}\mu t/\hbar} \tag{2.27a}$$

$$\psi_2(x,t) = \frac{\sqrt{N_2 \kappa/2}}{\cosh\left[\kappa (x - vt)\right]} \mathrm{e}^{\mathrm{i}mvx/\hbar - \mathrm{i}\omega t - \mathrm{i}\mu t/\hbar}. \tag{2.27b}$$

As its name indicates, the dark-bright soliton consists of a dark soliton (component $|1\rangle$) and a bright soliton (component $|2\rangle$). Here, N_2 is the total number of atoms in component $|2\rangle$, n_1 is the background density of component $|1\rangle$, and κ is the inverse width of the soliton. The parameter $\eta = \hbar/\sqrt{mgn_0}$ is defined as for the dark soliton, as well as the speed of sound $c = \sqrt{gn_0/m}$. The maximum depletion of component $|1\rangle$ reads: $\cos^2(\alpha)$. To simplify the notation, we define the dimensionless inverse width $\bar{\kappa} = \kappa\eta$ and the dimensionless

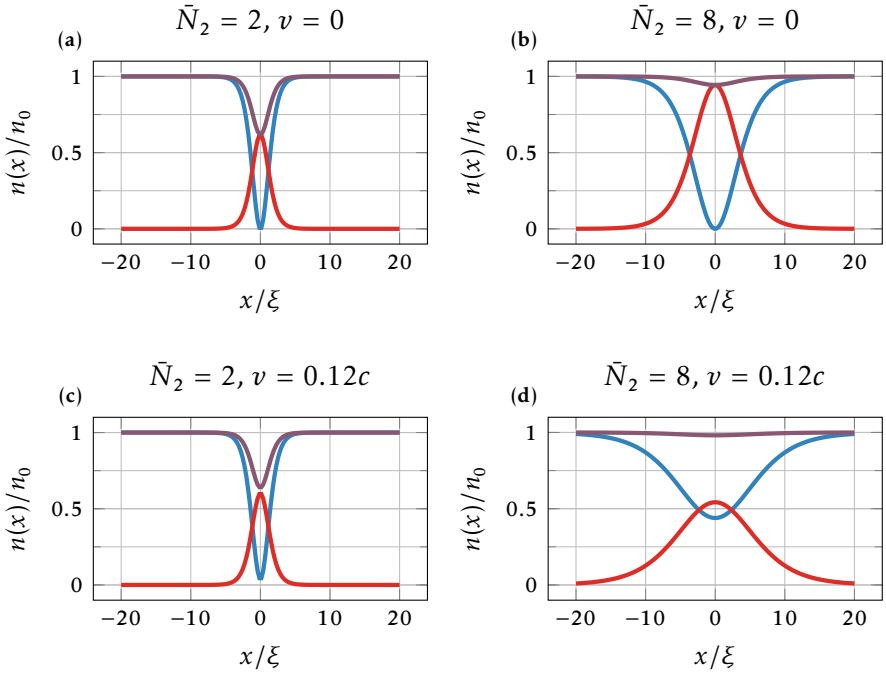

Figure 2.3: Density plots for dark-bright solitons. The blue (resp. red) curves are the density profiles of component $|1\rangle$ (resp. $|2\rangle$). The purple curve is the total density. (a, b) are bright solitons at rest, (c, d) are bright solitons with $v = 0.12c$. For (a, c) $\bar{N}_2 = 2$ whereas for (b, d) $\bar{N}_2 = 8$.

atom number $\bar{N}_2 = N_2/n_0\eta$. The parameter α is related to v by:

$$\frac{v}{c} = \bar{\kappa}\tan(\alpha). \tag{2.28}$$

The inverse width of the soliton is given by:

$$\bar{\kappa} = -\bar{N}_2/4 + \sqrt{\cos^2(\alpha) + \left(\bar{N}_2/4\right)^2}. \tag{2.29}$$

We observe in the equation above that κ is a decreasing function of N_2, meaning that at a given speed and bath density n_0, the dark component of the dark-bright soliton is wider than a one-component dark soliton. Finally, ω is given by:

$$\hbar\omega = \frac{1}{2}mv^2 - \frac{\hbar^2\kappa^2}{2m}. \tag{2.30}$$

In contrast to the dark soliton, the state of uniform density corresponds to a speed of 0 rather than c, as shown in fig. 2.4b. For fixed parameters, two different soliton profiles can share the same speed, as seen in fig. 2.4a. Plots of the density profiles of the soliton can be found in fig. 2.3. The total atomic density is given by:

$$n_0(x,t) = \left|\psi_1\right|^2 + \left|\psi_2\right|^2 = n_0\left(1 - \frac{\bar{\kappa}^2}{\cosh^2(\kappa(x - vt))}\right) \tag{2.31}$$

We can use the same procedure used in section 2.2.3.3 to find the momentum and

energy of the dark-bright soliton in the thermodynamic limit:

$$P = N_2 m v + \hbar n_0 \left[2\pi w + \pi \,\mathrm{sign}(v) - 2\arctan\left(\frac{v}{\bar{\kappa} c}\right) - 2\frac{\frac{v}{\bar{\kappa} c}}{1 + \left(\frac{v}{\bar{\kappa} c}\right)^2} \right] \tag{2.32a}$$

$$E = \hbar n_0 c \left[\frac{4}{3}\bar{\kappa}^3 + \frac{1}{2}\left(\bar{\kappa}^2 + \frac{v^2}{c^2}\right)\bar{N}_2 \right]. \tag{2.32b}$$

We do not address finite-size effects, as they will be studied in detail for the magnetic soliton, which is the primary focus of our experimental work. The energy is displayed in fig. 2.4c as a function of v, and in fig. 2.4d as a function of P. In the thermodynamic limit, we see that the energy is periodic in momentum, as for the dark soliton. As stated before this is a more general property of one-dimensional systems, that will be explained in section 3.5.2. The dark-bright soliton at rest has a momentum $P = (2k+1)\hbar n_0 \pi$ with $k \in \mathbb{Z}$. Its effective mass at rest is negative, as can be seen from the curvature of the energy in fig. 2.4d. Since $m_{\mathrm{eff}} = \left(\partial^2 E / \partial P^2\right)^{-1} = v^{-1}\, \partial E / \partial v$, we can see from fig. 2.4c that the effective mass changes sign after $E(v)$ reaches a maximum.

SU(2) **rotations: generating the dark-dark soliton family** In the Manakov limit, the coupled GP equations possess a SU(2) symmetry, meaning that if $\Psi^\intercal = (\psi_1, \psi_2)$ is a solution, then for any matrix $U \in \mathrm{SU}(2)$, $U\Psi$ is also a solution. This allows us to generate a whole family of solitons starting from the dark-bright soliton [155] (see also [156]). If we only consider solutions where the bath is at rest, we can restrict ourselves to SO(2) transformations that we parametrize by θ. The family of solutions is:

$$\begin{aligned}\psi_1(x,t) = \cos(\theta)\sqrt{n_0}\{\mathrm{i}\sin(\alpha) + \cos(\alpha)\tanh\left[\kappa\left(x - vt\right)\right]\}\,\mathrm{e}^{-\mathrm{i}\mu t/\hbar} \\ - \sin(\theta)\frac{\sqrt{N_2\kappa/2}}{\cosh\left[\kappa\left(x-vt\right)\right]}\,\mathrm{e}^{\mathrm{i}mvx/\hbar - \mathrm{i}\omega t - \mathrm{i}\mu t/\hbar}\end{aligned} \tag{2.33a}$$

$$\begin{aligned}\psi_2(x,t) = \sin(\theta)\sqrt{n_0}\{\mathrm{i}\sin(\alpha) + \cos(\alpha)\tanh\left[\kappa\left(x - vt\right)\right]\}\,\mathrm{e}^{-\mathrm{i}\mu t/\hbar} \\ + \cos(\theta)\frac{\sqrt{N_2\kappa/2}}{\cosh\left[\kappa\left(x-vt\right)\right]}\,\mathrm{e}^{\mathrm{i}mvx/\hbar - \mathrm{i}\omega t - \mathrm{i}\mu t/\hbar}.\end{aligned} \tag{2.33b}$$

For $\theta = 0$, we recover a dark-bright soliton described in eq. (2.27), while for $N_2 = 0$, each component is a dark soliton. In the general case, when $\tan(\theta)$ and N_2 are finite, we have a dark-dark soliton, as both components have a finite density at infinity. Due to the SU(2) symmetry, the total density profile $|\psi_1|^2 + |\psi_2|^2$ is independent of θ. However, the density of each component oscillates at frequency ω. While we have presented single soliton solutions here, analytical multi-soliton solutions can also be derived [154, 157].

2.3.2.2 Bright and dark solitons outside the Manakov limit

The solitons given in eq. (2.33) exist only in the Manakov limit. However, we can investigate solutions of the GPE outside the Manakov limit using either a bright or a dark soliton as an ansatz for each component. In this way, bright and dark solitons can be generalized beyond the Manakov limit. We will assume however in the following that all the interaction parameters are positive. This analysis was conducted by Mao *et al.* [158], who employed a Lagrangian approach. It is important to note that solutions like eq. (2.33), which mix bright and dark solutions for each component, are not included in their ansatz. Another constraint is that they examine only solutions with the same inverse width parameter κ for

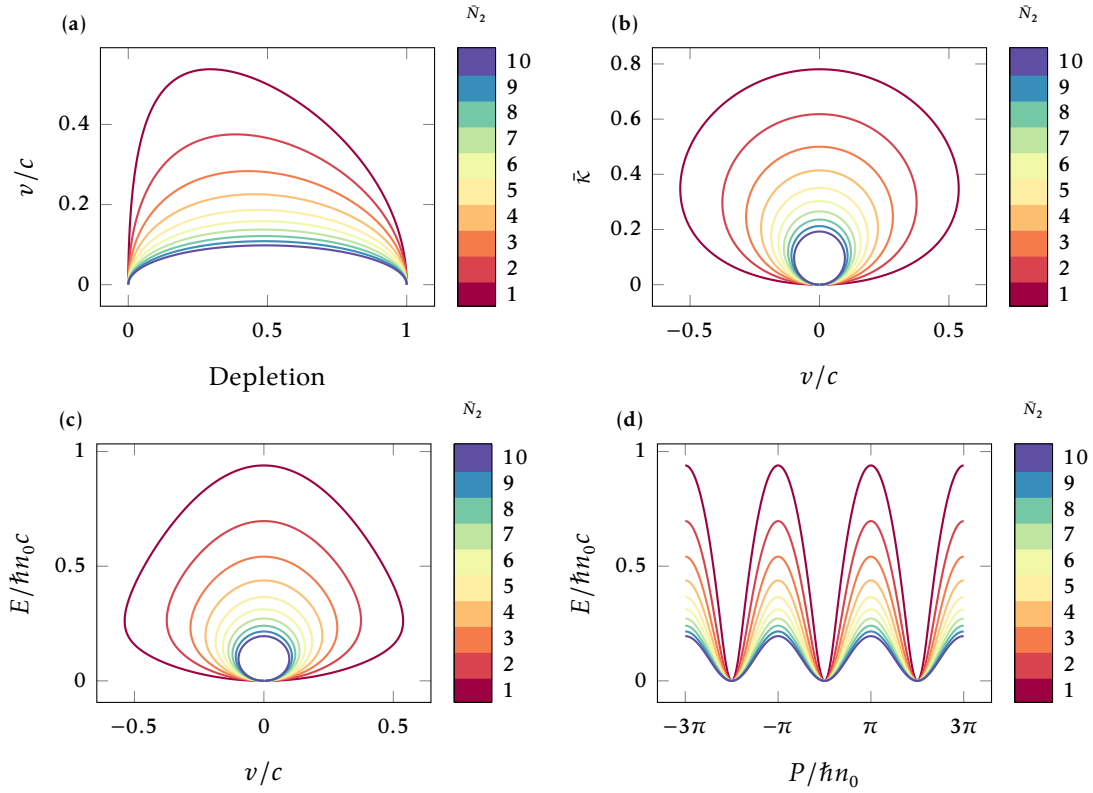

Figure 2.4: Plot of different characteristics of the dark-bright soliton, in the thermodynamic limit, for different dimensionless atom numbers $\bar{N}_2$ represented by plots of different colors. (a), speed of soliton as a function of the depletion of component $|1\rangle$. For each speed there are two different solitons with the same density and atom number in component $|2\rangle$. (b), Inverse dimensionless width, $\bar{\kappa}$, as a function of speed. The soliton reaches its minimum width at $v = 0$, corresponding to a bright soliton at rest and a dark soliton at rest. Conversely, the maximum width is attained when $\kappa = 0$, representing an infinitely diluted component $|1\rangle$ in a bath of component $|2\rangle$ with a flat density profile. (c), Energy as a function of speed; for $v = 0$ the solution at lowest energy has an inverse width $\kappa = 0$. (d), Energy as a function of momentum; the energy is periodic as in the case of the dark soliton.

both components, as is the case in the Manakov limit. Mao *et al.* identified three different solutions depending on the values of the interaction parameters:

- Dark-dark solitons, where both components' wave functions are given by a dark soliton.
- Dark-bright solitons, where one component is a dark soliton and the other a bright one, with the total density featuring a density bump as in the Manakov limit.
- Bright-dark solitons, identical to the dark-bright solitons except that the total density features a hump; this solution is not present in the Manakov limit.

In all three cases, the solutions are more constrained than in the Manakov limit: for the dark-dark soliton, the ratio of background densities is constrained; for the bright-dark and dark-bright solitons, the number of atoms in the bright soliton is constrained by the background density of the dark soliton. The different soliton regimes are shown in fig. 2.5.

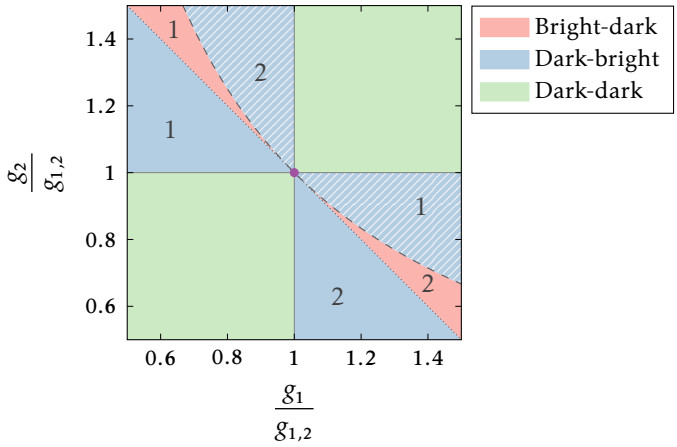

Figure 2.5: Solitons of the two-component GPE for different interaction parameters. In this plot all the interaction parameters are positive. The purple point is the Manakov limit. The dashed line represents the miscibility limit, above this curve the mixture is miscible whereas below it is immiscible. The dotted line are the points for which $g_{1,2} = g_1 + g_2$; on this line the solitons have a constant total density and are called spin solitons. The number inside the domains indicate which component is the bright one. The hatched areas correspond to solitons with a bright component whose extent diverges when submitted to a force, *c.f.* section 3.5.3.

At the border between the dark-bright and bright-dark cases, defined by $2g_{1,2} = g_1 + g_2$, the total density is constant. These solitons are called spin solitons [158, 159] and do not exist in the Manakov limit.

Other types of solutions exist that are not contained in the ansatz used by Mao *et al.* One example is the dark-antidark soliton [160].

2.3.2.3 Experimental realization of dark-bright solitons

The first realization of a dark-bright soliton was achieved by Anderson *et al.* [161]. This was also the first time a soliton was created using wave-function engineering, *i.e.* controlling both the density and the phase. They used ^{87}Rb with hyperfine states that are near the Manakov limit. Their experiment was not conducted in a 1D geometry but in a spherical trap. To create a dark-bright soliton, they start with a BEC in hyperfine state $|1\rangle$ and do a spatially resolved transfer $|1\rangle \rightarrow |2\rangle$. They create a state of two domains of atoms in state $|2\rangle$ separated by a narrow strip of atoms in state $|1\rangle$ with a π phase shift between the domains. This initial condition then evolves into a dark-bright soliton, with $|2\rangle$ forming the dark component. With this technique, only profiles with a total constant density can be imprinted. In addition to creating dark-bright solitons, they were also able to create dark solitons by removing all atoms of component $|1\rangle$.

A subsequent experimental realization reported in ref. [136] employed an immiscible mixture of ^{87}Rb atoms. The soliton generation protocol used a pair of Raman beams with a physical mask imaged onto the atomic cloud, ensuring illumination of only half the sample. Through the application of a 2π pulse, they establish a π phase difference between the two segments of the cloud remaining in the initial state $|1\rangle$. At the mask boundary, coinciding with the cloud's center, the reduced beam intensity results in partial population transfer to state $|2\rangle$. Similar to previous experimental configurations, this approach is constrained to generating density profiles with constant total density.

Dark-bright and dark-dark solitons were also generated with a miscible mixture, in a cigar-shaped trap. In ref. [162, 163], hyperfine states with opposite magnetic moments were used to generate solitons. Starting from a mixture of both species that overlapped spatially due to their miscibility, they applied a magnetic gradient, causing the species to flow in opposite directions. When the flow slightly exceeded a critical velocity v_{cr}, it triggered a modulational instability leading to the generation of dark-bright soliton trains [162]. For faster flows, $\gtrsim 3v_{cr}$ in ref. [163], the modulational instability led to the generation of generalized dark solitons described by eq. (2.33). It should be noted, however, that eq. (2.33) was derived in the Manakov limit, while the interaction parameters in the experiment [163] were outside this limit, though close to it. The authors still used this equation to describe the observed solitons.

2.3.3 Magnetic solitons

This section is adapted from [164]. While the core material remains from the original publication, I have significantly restructured the presentation of it and included supplementary information to better integrate it within the broader framework of the thesis.

We now turn our focus to another type of soliton of the two-component GPE: the magnetic soliton. Unlike the solitons previously mentioned, the magnetic soliton is not a combination of a dark and a bright soliton. Since this is the soliton we have studied experimentally in our group, we will examine it in greater detail. After reviewing its theoretical background, we will present our experimental implementation.

2.3.3.1 The Landau-Lifshitz Equation

Magnetic solitons were first studied in the case of the 1D LLE with uniaxial anisotropy [98, 165]:

$$\frac{\partial \mathbf{M}}{\partial t} = \left(\alpha \frac{\partial^2 \mathbf{M}}{\partial x^2} + \beta \mathbf{e_z}(\mathbf{M}\cdot\mathbf{e_z})\right) \times \mathbf{M}. \tag{2.34}$$

This equation describes the magnetization, $\mathbf{M}$, in a ferromagnetic crystal or spin chain in the long-wavelength approximation, i.e., considering that the spatial variation of $\mathbf{M}$ is slow compared to the lattice spacing. In the microscopic model, the exchange interaction between atomic spins is anisotropic; here we assume there is a symmetry axis z so that the anisotropy is uniaxial. We distinguish different situations according to the sign of β. If $\beta > 0$, the magnetization preferentially aligns along z (the easy-axis case); if $\beta < 0$, the magnetization preferentially lies in the (x, y) plane (the easy-plane case). Obviously, if $\beta = 0$, the system is isotropic. The LLE conserves the total magnetization $\mathbf{M}^2$, which is chosen to be spatially uniform. We set it to 1 to simplify notation. $\mathbf{M}$ can then be parametrized with only two real variables in spherical coordinates θ, φ:

$$\mathbf{M} = -\begin{pmatrix} \sin(\theta)\cos(\varphi) \\ \sin(\theta)\sin(\varphi) \\ \cos(\theta) \end{pmatrix}. \tag{2.35}$$

So that eq. (2.34) becomes

$$\frac{\partial}{\partial t}(\cos(\theta)) = -\alpha\frac{\partial}{\partial x}\left(\sin^2(\theta)\frac{\partial\varphi}{\partial x}\right) \tag{2.36a}$$

$$\sin(\theta)\frac{\partial\varphi}{\partial t} = \alpha\frac{\partial^2\theta}{\partial x^2} - \sin(\theta)\cos(\theta)\left(\beta + \alpha\left(\frac{\partial\varphi}{\partial x}\right)^2\right). \tag{2.36b}$$

2.3.3.2 Link with the Gross-Pitaevskii equation

Physical quantity	Rescaling to obtain physical units
Distance	$\xi_s = \dfrac{\hbar}{\sqrt{2n_0 m\lvert g_s\rvert}}$
Time	$\tau_s = \dfrac{2m\xi_s^2}{\hbar} = \dfrac{\hbar}{n_0\lvert g_s\rvert}$
Atom number in $\lvert 2\rangle$	$n_0\xi_s$
Current	$1/\tau_s = n_0\lvert g_s\rvert/\hbar$
Velocity	$c_s = \xi_s/\tau_s = \sqrt{\dfrac{\lvert g_s\rvert n_0}{2m}}$
Momentum	$\left(\dfrac{\hbar}{\xi_s}\right)(n_o\xi_s) = \hbar n_0$
Energy	$\left(\dfrac{\hbar}{\tau_s}\right)(n_o\xi_s) = n_0\hbar c_s$
Force	$\dfrac{\hbar}{\tau_s\xi_s}$

Table 2.1: Scaling factors to go from dimensionless to physical units. Since the factor $n_0\xi_s$ is dimensionless, the scaling factors are not uniquely defined. This table presents the choices we made for rescaling the different physical quantities.

Let us now consider a two-component BEC described by eq. (2.21). We note that in experiments, the external static and uniform magnetic field B_0 would add a term in both equations of eq. (2.21), leading to a time-dependent and uniform relative phase between the two states. This phase, however, can be eliminated by a unitary transform and does not play any role in the studied phenomena. We assume the two species have symmetric interactions, i.e., $g_1 = g_2 = g$. We define $g_s = g_{1,2} - g$. Furthermore, we consider the mixture to be close to the Manakov limit: $\lvert g_s\rvert \ll g$, which implies $\lvert g_s\rvert \ll g_{1,2}$. In this case[1], the spin modes, describing the evolution of $n_1 - n_2$, are decoupled from the density modes, describing the evolution of $n_1 + n_2$ [166, 167]. We can then make the hypothesis of total constant density, i.e., $\partial n_0/\partial x = 0$. In this case, the spinor describing the mixture can be

[1]This condition is sufficient if neither n_1 nor n_2 get too close to zero. It can be easily satisfied for a miscible mixture, but not for an immiscible one. The hypothesis of constant density is more challenging for the latter case; see eq. (10) of [166]

parametrized with three fields, $\theta(x,t)$, $\varphi(x,t)$,$\Phi(x,t)$:

$$\begin{pmatrix}\psi_1\\ \psi_2\end{pmatrix} = \sqrt{n_0}\,\mathrm{e}^{\mathrm{i}\Phi/2}\begin{pmatrix}\cos(\theta/2)\,\mathrm{e}^{-\mathrm{i}\varphi/2}\\ \sin(\theta/2)\,\mathrm{e}^{+\mathrm{i}\varphi/2}\end{pmatrix}. \tag{2.37}$$

Where $\Phi_1 = (\Phi - \varphi)/2$ and $\Phi_2 = (\Phi + \varphi)/2$ are respectively the phases of ψ_1 and ψ_2. The total particle current is defined as

$$\chi(x,t) = \frac{\hbar}{m}\,\mathcal{I}(\psi_1^*\partial_x\psi_1 + \psi_2^*\partial_x\psi_2), \tag{2.38}$$

where $\mathcal{I}(z)$ is the imaginary part of z. It satisfies the continuity equation:

$$\frac{\partial n_0}{\partial t} + \frac{\partial \chi(x,t)}{\partial x} = 0 \tag{2.39}$$

Under the assumption of constant total density, the continuity equation yields $\partial_x\,\chi = 0$. The total particle current is thus space-independent. We now set the spin healing length $\xi_s = \hbar/\sqrt{2n_0 m|g_s|}$ as the length unit and $\tau_s = \hbar/(n_0|g_s|)$ as the time unit. In the following, we use the $\tilde{\cdot}$ notation for dimensionless quantities. Table 2.1 indicates the scaling of the different physical quantities to go from dimensionless to physical units.

By substituting eq. (2.37) in eq. (2.38), we obtain the following expression for the dimensionless total particle current:

$$\tilde{\chi}(\tilde{x},\tilde{t}) = n_0\xi_s\left[\cos^2(\theta/2)\,(\partial_{\tilde{x}}\Phi - \partial_{\tilde{x}}\varphi) + \sin^2(\theta/2)\,(\partial_{\tilde{x}}\Phi + \partial_{\tilde{x}}\varphi)\right]. \tag{2.40}$$

For convenience, we introduce $\tilde{J} = \tilde{\chi}/(n_0\xi_s)$. Using eq. (2.40), we get the relation

$$\partial_{\tilde{x}}\Phi = \cos(\theta)\,\partial_{\tilde{x}}\varphi + \tilde{J}. \tag{2.41}$$

We can now rewrite the 2-component GPE given in eq. (2.21) as a function of the three variables θ, φ and $\tilde{J}$:

$$\partial_{\tilde{t}}\,\theta = -2\cos(\theta)(\partial_{\tilde{x}}\varphi)(\partial_{\tilde{x}}\theta) - \sin(\theta)\partial_{\tilde{x}}^2\varphi - \tilde{J}\partial_{\tilde{x}}\theta \tag{2.42a}$$

$$\partial_{\tilde{t}}\,\varphi = -\cos(\theta)\left[\mathrm{sign}(g_s) + (\partial_{\tilde{x}}\varphi)^2\right] + \frac{\partial_{\tilde{x}}^2\theta}{\sin(\theta)} - \tilde{J}\partial_{\tilde{x}}\varphi. \tag{2.42b}$$

The previous equation closely resembles the LLE in spherical coordinates eq. (2.36). Indeed, there exists an equivalence between the LLE and the two-component GPE with the constant density hypothesis [166, 168, 169]. If we define the effective spin as

$$\mathbf{M} = -\frac{1}{n_0}\begin{pmatrix}2\mathcal{R}(\psi_2\psi_1^*)\\ 2\mathcal{I}(\psi_2\psi_1^*)\\ |\psi_1|^2 - |\psi_2|^2\end{pmatrix}, \tag{2.43}$$

where $\mathcal{R}(z)$ is the real part of z, then $\mathbf{M}$ satisfies the LLE in a moving frame at speed $\tilde{J}$:

$$\frac{\partial\mathbf{M}}{\partial\tilde{t}} + \tilde{J}\frac{\partial\mathbf{M}}{\partial\tilde{x}} = \left(\frac{\partial^2\mathbf{M}}{\partial\tilde{x}^2} + \mathrm{sign}(g_s)\mathbf{e_z}(\mathbf{M}\cdot\mathbf{e_z})\right)\times\mathbf{M}. \tag{2.44}$$

For a miscible mixture ($g_s < 0$), the mixture is equivalent to an easy-plane ferromagnet, whereas for an immiscible mixture ($g_s > 0$), the mixture is equivalent to an easy-axis ferromagnet.

2.3.3.3 Lagrangian approach and conserved quantities.

Starting from the GP Lagrangian density:

$$\begin{aligned}\mathcal{L} = \mathrm{i}\frac{\hbar}{2}\left(\psi_1^*\frac{\partial\psi_1}{\partial t} + \psi_2^*\frac{\partial\psi_2}{\partial t} - \frac{\partial\psi_1^*}{\partial t}\psi_1 - \frac{\partial\psi_2^*}{\partial t}\psi_2\right) - \frac{\hbar^2}{2m}\left(\left|\frac{\partial\psi_1}{\partial x}\right|^2 + \left|\frac{\partial\psi_2}{\partial x}\right|^2\right) \\ -\frac{g}{2}\left(|\psi_1|^4 + |\psi_2|^4\right) - g_i|\psi_1|^2|\psi_2|^2,\end{aligned} \tag{2.45}$$

and using the parametrization of eq. (2.37) we obtain the following dimensionless Lagrangian density:

$$\begin{aligned}\tilde{\mathcal{L}} = \frac{n_0\xi_s}{2}\left\{\left[\cos(\theta)\frac{\partial\varphi}{\partial\tilde{t}} - \frac{\partial\Phi}{\partial\tilde{t}}\right] - \frac{1}{2}\left[\left(\frac{\partial\theta}{\partial\tilde{x}}\right)^2 + \left(\frac{\partial\varphi}{\partial\tilde{x}}\right)^2 + \left(\frac{\partial\Phi}{\partial\tilde{x}}\right)^2\right] + \cos(\theta)\frac{\partial\Phi}{\partial\tilde{x}}\frac{\partial\varphi}{\partial\tilde{x}} \right. \\ \left. - \frac{1}{2}\sin^2(\theta)\right\}.\end{aligned} \tag{2.46}$$

Euler-Lagrange equations give eq. (2.41) and eq. (2.42). The Lagrangian does not depend explicitly neither on φ, Φ nor on t. From Noether's theorem we derive two conserved quantities [169–171]:

$$\tilde{N} = \frac{1}{2}\int \mathrm{d}\tilde{x}\,[1 - \cos(\theta)] \tag{2.47}$$

$$\tilde{E} = \frac{1}{4}\int \mathrm{d}\tilde{x}\left\{(\partial_{\tilde{x}}\theta)^2 + \sin^2(\theta)\left[1 + (\partial_{\tilde{x}}\varphi)^2\right] + \tilde{J}^2\right\}. \tag{2.48}$$

The quantity $\tilde{N} = N_2/(n_0\xi_s)$ is associated with the atom number in the wave packet. The quantity $\tilde{E}$ corresponds, up to an overall constant term, to the total energy of the system. We also note that the Lagrangian doesn't depend on x, applying Noether's theorem again yields[2]:

$$\frac{\partial\tilde{Q}}{\partial\tilde{t}} = \frac{1}{n_0\xi_s}\left(\tilde{\mathcal{L}}(\tilde{L}/2,\tilde{t}) - \tilde{\mathcal{L}}(-\tilde{L}/2,t)\right), \tag{2.49}$$

with

$$\tilde{Q} = \int_{-\tilde{L}/2}^{\tilde{L}/2}\frac{\tilde{J}}{2}\mathrm{d}\tilde{x} = \frac{\tilde{J}}{2\tilde{L}} \tag{2.50}$$

$\tilde{Q}$ corresponds to the dimensionless momentum given by the GPE:

$$\tilde{Q} = \frac{1}{\mathrm{i}n_0}\int_{-\tilde{L}/2}^{\tilde{L}/2}(\psi_1^*\partial_{\tilde{x}}\psi_1 + \psi_2^*\partial_{\tilde{x}}\psi_2)\,\mathrm{d}\tilde{x} \tag{2.51}$$

We emphasize that $\tilde{Q}$, is not necessarily a conserved quantity due to boundary effects.

2.3.3.4 Soliton solution

Magnetic solitons in cold atoms were first studied for miscible mixtures [167]. The first experimental realization was also conducted in a miscible mixture of ^{23}Na in ref. [172], where they created a pair of magnetic solitons via phase imprinting.

[2]When applying Noether's theorem, we do not forget to take into account boundary terms that do not necessarily vanish.

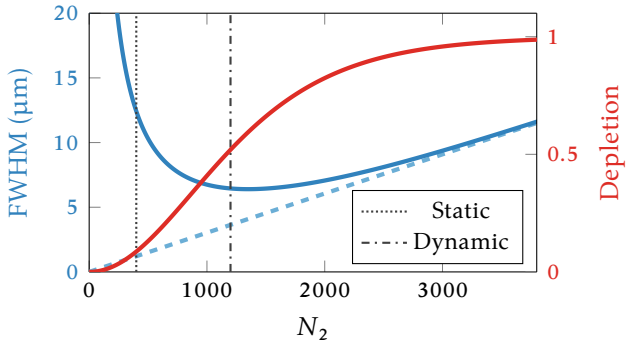

Figure 2.6: FWHM and depletion of a magnetic soliton. We focus on the soliton at rest ($\tilde{v} = 0$ and $\tilde{J} = 0$). This graph is plotted using typical parameters of the experiment: $n_0 = 330\,\mu\text{m}^{-1}$ and $\xi_s = 2\,\mu\text{m}$. The dashed blue line represents the limit of a spin domain. The two vertical gray lines represent the typical atom number used experimentally in the case of a static or moving soliton.

For the following discussion, we will focus on the immiscible case ($g_s > 0$). It is important to mention that the solitonic solutions presented herein, while requiring interactions to operate within the Manakov limit, cannot exist precisely at the Manakov limit where $g_s = 0$.

We consider a system of size $\tilde{L}$, assumed to be much larger than the soliton's size. We seek solitonic solutions of eq. (2.42), where component $|2\rangle$ is localized. This implies $\lim_{\tilde{x}\to\pm\tilde{L}/2} \sin(\theta/2) = 0$ and $\lim_{x\to\pm L/2} \left|\partial\varphi/\partial\tilde{x}\right| = 0$. Additionally, traveling wave solutions are desired, expressed as: $\theta(\tilde{x},\tilde{t}) = \theta(\tilde{x} - \tilde{v}\tilde{t})$, $\varphi(\tilde{x},\tilde{t}) = \Omega\tilde{t} + \bar{\phi}(\tilde{x} - \tilde{v}\tilde{t})$, where $\tilde{v}$ represents the soliton's velocity in the laboratory frame. This family of solutions, parametrized by $(\Omega, \tilde{v})$, is called magnetic solitons. It has been studied, for instance, in ref. [99] for the case $\tilde{J} = 0$. For arbitrary values of $\tilde{J}$, it can be shown that:

$$\cos[\theta(\tilde{x})] = 1 - \frac{4\kappa^2}{2 + \Omega + \sqrt{\Omega^2 + \tilde{u}^2}\cosh(2\kappa\tilde{x})} \tag{2.52a}$$

$$\bar{\phi}(\tilde{x}) = \frac{1}{2}\tilde{u}\tilde{x} + \arctan\left[\frac{2\Omega - \tilde{u}^2 + 2\sqrt{\Omega^2 + \tilde{u}^2}}{2\kappa\tilde{u}}\tanh(\kappa\tilde{x})\right], \tag{2.52b}$$

where $\tilde{u} = \tilde{v} - \tilde{J}$ is the velocity of the soliton in the frame moving with the current in the bath and $\kappa = \sqrt{1 + \Omega - \tilde{u}^2/4}$. These solitonic solutions exist provided that $1 + \Omega > \tilde{u}^2/4$. We notice that the function $\bar{\phi}$ is not defined for $\tilde{u} = 0, \Omega > 0$. Indeed, we have

$$\lim_{\tilde{u}\to 0^+,\ \Omega>0} \bar{\phi} = -\lim_{\tilde{u}\to 0^-,\ \Omega>0} \bar{\phi} = -\frac{\pi}{2} + \pi H(\tilde{x}), \tag{2.53}$$

where H is the Heaviside function. These two solutions describe the same physical situation as shown in fig. 2.9. At this point the bath is fully depleted at the position of the soliton and Φ_1 features a $\pm\pi$ phase jump.

We illustrate the properties of the soliton at rest by showing in fig. 2.6 the evolution of the Full Width at Half Maximum (FWHM) size of the wave packet in $|2\rangle$ as a function of N_2 for our typical experimental parameters. The associated depletion of the bath, corresponding to $1 - \min_x [n_1(x)/n_0]$ is also plotted on the same graph. In the limit $\tilde{N} \gg 1$, the soliton becomes a spin domain of size N_2/n_0 in physical units.

The expressions for the conserved quantities $\tilde{N}$ and $\tilde{E}$ in terms of the parameters Ω

and $\tilde{u}$ are given by:

$$\tilde{N} = \ln\left(\frac{2+\Omega+2\kappa}{\sqrt{\Omega^2+\tilde{u}^2}}\right) \quad \text{or equivalently} \quad \sinh(\tilde{N}) = \frac{2\kappa}{\Omega^2+\tilde{u}^2} \tag{2.54}$$

$$\tilde{E} = 2\kappa + \int \mathrm{d}\tilde{x}\, \frac{\tilde{J}^2}{4}. \tag{2.55}$$

With some algebra we obtain from eq. (2.54):

$$\frac{\sinh^2(\tilde{N})}{4}\left[u^2 + \tanh^2(\tilde{N})\left(\Omega - \frac{2}{\sinh^2(\tilde{N})}\right)^2\right] = 1. \tag{2.56}$$

From the previous equation we see that in the $(\tilde{u}, \Omega)$ plane the soliton solutions with constant $\tilde{N}$ lie on an ellipse, displayed in fig. 2.9 for the case $\tilde{N} = 2$. Like for the dark-bright soliton to each speed correspond two different solutions.

Starting from eq. (2.41), we can derive the following equation:

$$\Delta\Phi_1 + \frac{\tilde{J}\tilde{L}}{2} = \frac{1}{2}\int (1-\cos(\theta))\,\frac{\partial\bar{\phi}}{\partial\tilde{x}}\,\mathrm{d}\tilde{x} = \arctan\left(\frac{\kappa\tilde{u}}{\sqrt{\Omega^2+\tilde{u}^2}-\Omega+\frac{\tilde{u}^2}{2}}\right), \tag{2.57}$$

where $\Delta\Phi_1 = \Phi_1(-\tilde{L}/2) - \Phi_1(\tilde{L}/2)$. Combining eq. (2.54) and eq. (2.55) with the previous equation, we obtain the following equation for the energy of the soliton

$$\tilde{E} = 2\tanh(\tilde{N}/2) + 4\frac{\sin^2(\Delta\Phi_1/2 + \tilde{J}\tilde{L}/4)}{\sinh(\tilde{N})} + \int \frac{\tilde{J}^2}{4}\,\mathrm{d}\tilde{x}\,. \tag{2.58}$$

2.3.3.5 Two different geometries

We now describe the situation with two different boundary conditions, both were realized experimentally in our setup.

Periodic boundary conditions The system is a ring, this is the geometry we used to derive the momentum and energy of the dark and dark-bright soliton. For a system with periodic boundary conditions, the wave-function is single-valued at $x = \pm L/2$ implying: $\Phi_1(-L/2) = \Phi_1(L/2) \pmod{2\pi}$. With periodic boundary conditions we have $\tilde{\mathcal{L}}(L/2) = \tilde{\mathcal{L}}(-L/2)$, eq. (2.49) then implies that $\tilde{Q}$ is a conserved quantity. $\tilde{Q}$ is the canonical momentum of the soliton $\tilde{P}$:

$$\tilde{P} = \tilde{Q} = \tilde{J}\tilde{L}/2. \tag{2.59}$$

Inserting this expression in eq. (2.58), we obtain

$$\tilde{E}(\tilde{N}, \tilde{P}) = 2\tanh(\tilde{N}/2) + 4\frac{\sin^2(\tilde{P}/2)}{\sinh(\tilde{N})} + \frac{\tilde{P}^2}{\tilde{L}}. \tag{2.60}$$

The energy is plotted in fig. 2.7b.

Due to the presence of the last term, the energy is thus not a periodic function of $\tilde{P}$ in finite systems. As with the dark and dark-bright cases, this last term represents the backflow energy, which vanishes in the thermodynamic limit, thereby restoring the energy's periodicity.

Strict boundary conditions Since the system is confined within a segment, the strict boundary conditions require that the total current $\tilde{J}(t)$ remains zero at all times, such that eq. (2.41) becomes:

$$\partial_{\tilde{x}}\Phi = \cos(\theta)\,\partial_{\tilde{x}}\varphi. \tag{2.61}$$

We can thus rewrite the Lagrangian of the system given in eq. (2.46) using only two fields: $\theta(x,t)$, $\varphi(x,t)$. Keeping in mind that the Lagrangian can be defined up to a total derivative, the Lagrangian density of the system with strict boundary conditions can be written as:

$$\tilde{\mathcal{L}}_{\mathrm{SBC}} = \frac{n_0\xi_s}{2}\left\{[\cos(\theta)-1]\,\frac{\partial\varphi}{\partial\tilde{t}} - \frac{1}{2}\left[\left(\frac{\partial\theta}{\partial\tilde{x}}\right)^2 + \left(\frac{\partial\varphi}{\partial\tilde{x}}\right)^2\right] + \frac{1}{2}\cos^2(\theta)\left(\frac{\partial\varphi}{\partial\tilde{x}}\right)^2 - \frac{1}{2}\sin^2(\theta)\right\}. \tag{2.62}$$

We previously assumed the segment was large compared to the extent of the soliton, so that $\cos\theta(\pm L/2) = 1$, $\partial_{\tilde{x}}\theta\big|_{x=\pm L/2} = 0$, and $\partial_{\tilde{x}}\varphi\big|_{x=\pm L/2} = 0$, yielding:

$$\tilde{\mathcal{L}}_{\mathrm{SBC}}(\tilde{L}/2,t) = \tilde{\mathcal{L}}_{\mathrm{SBC}}(-\tilde{L}/2,t). \tag{2.63}$$

The Lagrangian density $\tilde{\mathcal{L}}_{\mathrm{SBC}}$ does not explicitly depend on $\tilde{x}$. Applying Noether's theorem, and noting that the boundary terms vanish as stated above, we derive the following conservation law:

$$\frac{\partial\tilde{P}}{\partial\tilde{t}} = 0, \tag{2.64}$$

where

$$\tilde{P} = \frac{1}{2}\int[1-\cos\theta(x)]\,\frac{\partial\varphi}{\partial\tilde{x}}\,\mathrm{d}\tilde{x}\,. \tag{2.65}$$

The quantity $\tilde{P}$ is the momentum of the soliton, which is conserved. Using eq. (2.61) and remembering that $\Phi_1 = (\Phi-\varphi)/2$, we can rewrite it:

$$\tilde{P} = \Delta\Phi_1, \tag{2.66}$$

such that the dimensionless momentum of the soliton is given by the phase difference between to the ends of the bath: $\Delta\Phi_1 = \Phi_1(-\tilde{L}/2) - \Phi_1(\tilde{L}/2)$. Moreover, under the assumption of zero total current, the phase of the bath is uniform away from the localized wave packet of the minority component, *i.e.* when $\cos(\theta) = 0$, as can be seen using the continuity equation eq. (2.39). The phase difference $\Delta\Phi_1$, can then be evaluated by choosing any two points far from the center of the soliton, not necessarily at the system's edge. We notice that unlike the case with periodic boundary, $\tilde{P} \neq \tilde{P}_{\mathrm{GPE}}$.

The energy of the soliton, given by eq. (2.58) reads:

$$\tilde{E}(\tilde{N},\tilde{P}) = 2\tanh\!\left(\tilde{N}/2\right) + 4\frac{\sin^2(\tilde{P}/2)}{\sinh\!\left(\tilde{N}\right)}. \tag{2.67}$$

This relation is periodic in $\tilde{P} = \Delta\Phi_1$. We note that the energy for the system with strict boundary conditions and finite size is the same as the one with periodic boundary conditions at the thermodynamic limit. The energy is plotted in fig. 2.7a.

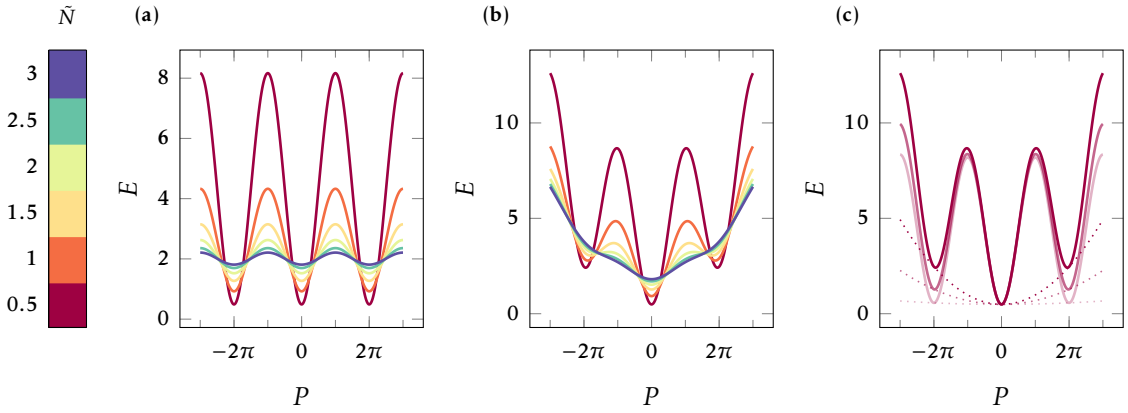

Figure 2.7: Dimensionless energy as a function of dimensionless momentum for the magnetic soliton. For different $\tilde{N}$ and a system of dimensionless size $\tilde{L} = 20$, (a), with strict boundary conditions, (b), with periodic boundary conditions. For finite-size systems the energy is a periodic function of the momentum in the first case but not in the second. (c), The solid lines are the dimensionless energies for $\tilde{N} = 0.5$, and $\tilde{L} \in \{20, 50, 100\}$, the darker the curve, the smaller the system. The dotted lines are $\tilde{E}(0) + \tilde{P}^2/\tilde{L}$, the energy of the backflow offset by the energy of the system at rest.

Link between periodic and strict boundary conditions. At a given $(\tilde{N}, \tilde{P})$ the solution for periodic or strict boundary conditions give the same density profile for both components but a different phase profile. This is because the solution are linked by a change of reference frame. Starting with a soliton with strict boundary conditions in a reference frame $\mathcal{R}$, we can obtain the profile of a soliton with periodic boundary condition by doing a change of reference frame to a frame $\mathcal{R}'$ moving at a relative speed:

$$\tilde{v}_{\mathcal{R}'/\mathcal{R}} = \frac{2\Delta\Phi_{1,\mathcal{R}}}{\tilde{L}} + \frac{4\pi}{\tilde{L}} w, \tag{2.68}$$

$$\text{with} \quad w = \frac{1}{2\pi} \int_{-\tilde{L}/2}^{\tilde{L}/2} \partial\Phi_1 \tilde{x} \, \mathrm{d}\tilde{x} \, .$$

The integer w is called the phase winding number. In the new frame we have $\Phi_{1,\mathcal{R}'}(L/2) = \Phi_{1,\mathcal{R}'}(-L/2) + 2\pi w$, ensuring periodic boundary conditions. The fast phase jump around the central position of the soliton in frame $\mathcal{R}$, $\Delta\Phi_{1,\mathcal{R}}$, is compensated in frame $\mathcal{R}'$ by a slow linear variation of the phase. This slope in the phase manifests itself physically by the presence of a backflow [148], a current of atoms in the bath given by:

$$\tilde{J}_{\mathcal{R}'} = 2\left(\frac{\Delta\Phi_{1,\mathcal{R}}}{\tilde{L}} + \frac{2\pi w}{\tilde{L}}\right). \tag{2.69}$$

In the frame $\mathcal{R}'$ with periodic boundary conditions the momentum $\tilde{P}_{\mathcal{R}'}$ of the soliton is $\tilde{J}_{\mathcal{R}'} L/2$. So we find:

$$\tilde{P}_{\mathcal{R}'} = \tilde{P}_{\mathcal{R}} + 2\pi w. \tag{2.70}$$

This explains that at a given N and $P \pmod{2\pi}$ a magnetic soliton will have the same density profile for both components, whether it obeys periodic or strict boundary conditions. The phase profiles however differ, as can be seen in fig. 2.8, where the phase profiles of

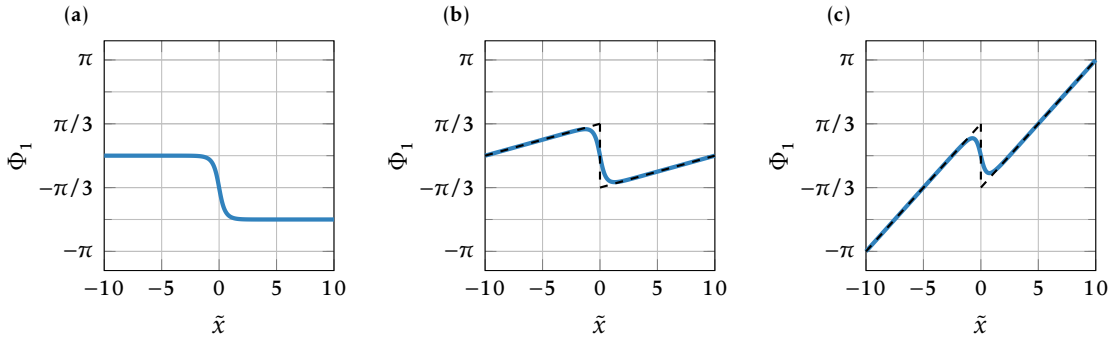

Figure 2.8: Bath phase profile for a soliton with $\tilde{N} = 2$. (a), $\tilde{P} = 2\pi/3$, with strict boundary conditions. (b), $\tilde{P} = 2\pi/3$ with periodic boundary conditions, here the winding number $w = 0$. (c), $\tilde{P} = 2\pi/3 + 2\pi$ with periodic boundary conditions, here the winding number $w = 1$. The black dotted line has a slope $\tilde{P}/L$ and jumps of a value: $\tilde{P} - 2\pi w$ at $\tilde{x} = 0$, the central position of soliton. The density profiles of components $|1\rangle$ and $|2\rangle$ remain unchanged in each of the three cases described here.

the bath in frame $\mathcal{R}$ and in frame $\mathcal{R}'$ are plotted. The previous reasoning is reminiscent of the case of the dark or dark-bright soliton where we also did a change of reference frame to have a solution obeying periodic boundary conditions. The energy difference between the soliton on fig. 2.8b and fig. 2.8a is

$$\frac{(\tilde{v}_{\mathcal{R}'/\mathcal{R}})^2}{2} = \frac{\tilde{P}_{\mathcal{R}'}^2}{\tilde{L}}, \tag{2.71}$$

the energy of the backflow current.

We conclude by mentioning that in both cases the momentum of the soliton is given by [169–171]:

$$\tan(\tilde{P}/2) = \frac{\kappa\tilde{u}}{\sqrt{\Omega^2 + \tilde{u}^2} - \Omega + \frac{\tilde{u}^2}{2}}. \tag{2.72}$$

We also have for both boundary conditions:

$$\tilde{u} = 2\frac{\sin\tilde{P}}{\sinh\tilde{N}} = \left.\frac{\partial\tilde{E}}{\partial\tilde{P}}\right|_{\tilde{N}}. \tag{2.73}$$

This confirms that the quantity $\tilde{P}$ verifies the definition of a canonical momentum.

Summary for strict boundary conditions. In fig. 2.9, we summarize our results for the strict boundary conditions. The soliton with $\tilde{v} = 0$, $\Omega < 0$ exhibits a flat bath phase, has zero momentum, and minimizes the energy. Conversely, the solution at $\tilde{v} = 0$, $\Omega > 0$ features complete depletion of component $|1\rangle$ and a π phase jump in Φ_1. This solution has momentum $\tilde{P} = \pi$ and maximizes the energy.

2.3.3.6 Our experimental realization of a magnetic soliton at rest

In this subsection, we demonstrate the experimental realization of a stationary magnetic soliton in a segment. This is the first realization of a magnetic soliton in an immiscible system. Notably, in contrast to the experiments discussed earlier, that relied on cigar-

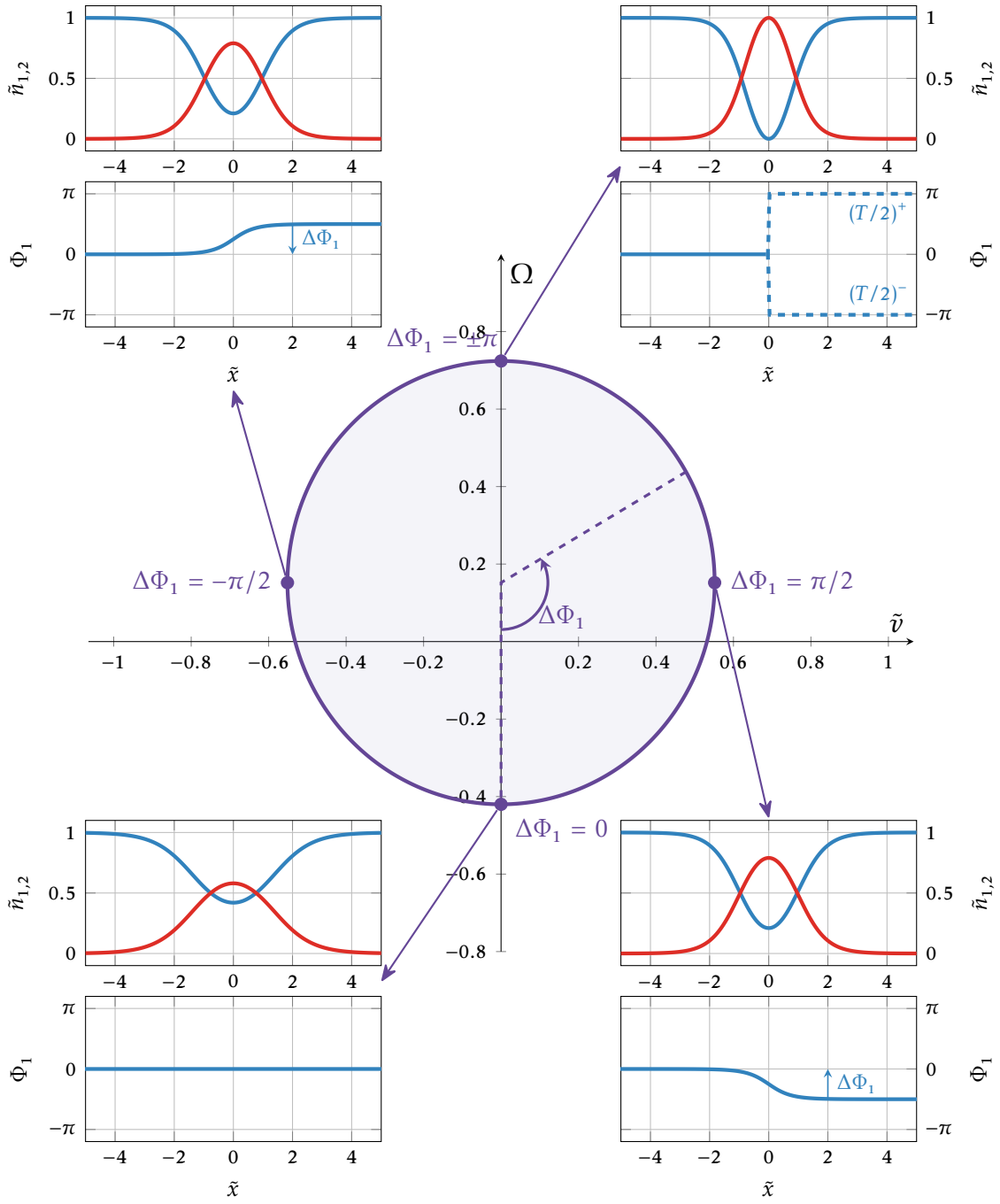

Figure 2.9: Magnetic solitons with strict boundary conditions. The ellipse in the $(\tilde{v}, \Omega)$ plane represents all soliton solutions for $\tilde{N} = 2$. The polar coordinate on this ellipse corresponds to the bath phase jump $\Delta\Phi_1$, or equivalently, the soliton momentum. The four insets correspond to solitons with the minimum and maximum speeds in absolute value. In each inset, the top graph shows the density of component $|1\rangle$ in blue and $|2\rangle$ in red, while the bottom graph displays the phase of component $|1\rangle$.

shaped traps, axial confinement is completely absent in our setup. To the best of our knowledge, the only other instance of a matter-wave soliton realized without residual harmonic confinement is the Townes soliton [152], a two-dimensional soliton. Additionally, we directly imprint the soliton's wave function, a method rarely employed in previous experiments. Among all the experiments cited earlier, only [139] directly imprinted the soliton profile. In all others, solitons typically emerged from an evolving initial profile rather than being imprinted directly. We imprint a soliton with $v = 0$, $\Omega < 0$ so with zero momentum, corresponding to the bottom point of fig. 2.9, where the phases of both components are flat.

We generate a soliton with a large size such that we remain in the low depletion limit. In this limit, i.e., $N_2 \to 0$, we have $\Omega \to 0$. From eq. (2.52a) and eq. (2.37), we find that the stationary profile of the minority component is given by:

$$n_2(x) = N_s/[2\sigma \cosh^2(x/\sigma)], \tag{2.74}$$

where N_s is defined as the stationary atom number and $\sigma = \hbar^2/(m g_s N_s)$ is the corresponding width. We recover the shape of a bright soliton given in eq. (2.7). This is not surprising because, as we saw in section 2.3.1.2, at low depletion the two-component GPE can be mapped to an effective one-component model. To first order in g_s, the effective interaction parameter becomes $g_e \sim -2g_s$, establishing the correspondence between eq. (2.74) and eq. (2.7). Interestingly, in this regime, the soliton shape remains independent of the atom number, in contrast to the general case as seen in eq. (2.52).

The soliton is realized using the mixture $|1\rangle = |F = 1, m_F = -1\rangle$, $|2\rangle = |F = 1, m_F = 1\rangle$. By symmetry, $|1\rangle$ and $|2\rangle$ have the same intra-species scattering length $a_1 = (100.4 - 0.18)\, a_0$, where a_0 is the Bohr radius. The interspecies scattering length is $a_i = (101.3 + 0.18)\, a_0$ [173]. For both scattering lengths, we have added the correction due to magnetic dipole-dipole interactions [174], which are non-negligible in this geometry because of the strong confinement along the z direction. This mixture is thus weakly immiscible ($a_i > a_1$). Its immiscibility is enhanced by magnetic dipole-dipole interactions compared to the case of ref. [175], where demixing dynamics have been studied in a 3D geometry. The precise value of g_s depends on the detailed shape of the trapping potential along y and its calibration is discussed below.

We prepare a single tube of $N_1 \approx 2 \times 10^4$ atoms in an optical dipole trap. The tube, with a length of $L = 60\,\mu$m and uniform linear density $n_0 = N_1/L = 330\,\mu\text{m}^{-1}$, is derived from a horizontal uniform planar 2D Bose gas. The atoms are initially confined within a rectangular box potential. A series of 50 interpolated images, displayed every 10 ms on DMD1, gradually transforms the box potential into a segment geometry. The final transverse confinement is achieved using a flat-bottom optical potential of full width $\sigma_y = 3\,\mu$m, smoothed by the projection system's resolution of 1 µm. For this experiment, the vertical lattice trapping frequency $\omega_z = 2\pi \times 4.3(1)\,$kHz corresponds to a ground-state wave function size of $\approx 160\,$nm. The initial gas temperature is below 20 nK, placing it in the weakly interacting regime with a Lieb-Liniger parameter [3] [176] $\gamma \approx 10^{-4}$.

The soliton is generated using a two-step process from a cloud initially in state $|1\rangle$. The first step is a spatially-resolved two-photon transfer from state $|1\rangle$ to state $|3\rangle = |F = 2, m_F = 0\rangle$. To do so, we use a pair of Raman beams at a wavelength of 790 nm, in between the $D1$ and $D2$ transitions and close to the tune-out wavelength, to limit the effect of dipole forces. In the absence of dipole forces, the phase of both components is unaffected by the Raman beams and remains flat. The Raman beams are shaped using DMD3 to imprint the desired solitonic profile $n_3(x)$. The pulse duration is $\approx 20\,\mu$s, adjusted to

[3] This value of γ should be considered with care because we are not strictly in the 1D regime.

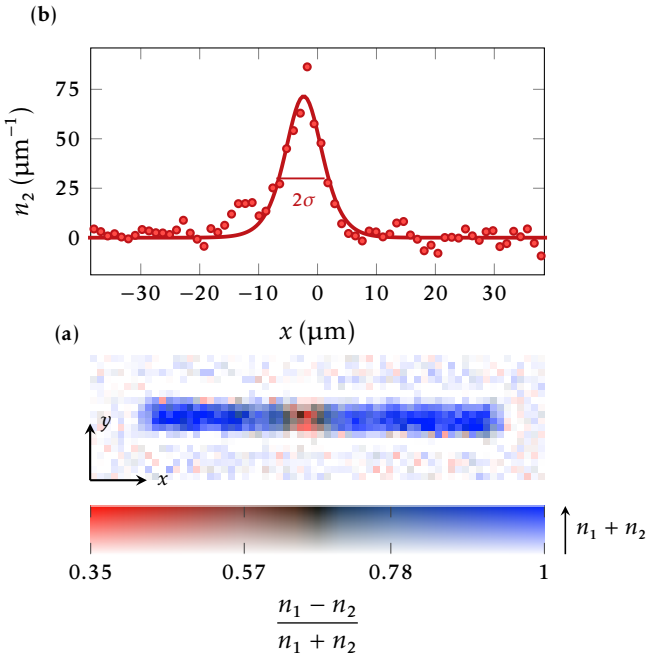

Figure 2.10: (a), Reconstructed absorption image of the initial density profiles in both $|1\rangle$ and $|2\rangle$. The colors represent the relative weight of the atomic densities n_1 and n_2 of both components. The opacity of the image is proportional to the total density of the system. (b), Integrated density profile of component $|2\rangle$ along the transverse direction of the absorption image. The solid line is a fit of the data to a $1/\cosh^2$ function, which corresponds to the expected shape of the soliton in the limit of low values of n_2/n_1 at the soliton position.

control the soliton amplitude. The total density $n_0 = n_1(x) + n_3(x)$ remains unaffected by the transfer, because of the low dipole force exerted by the Raman beams combined with their short pulse duration. Because the soliton shape is independent of N_2 in this regime, the pattern on DMD3 remains the same for all atom numbers. In the second step, immediately after the first one, a microwave transfer completes the state preparation by transferring all atoms in $|3\rangle$ to state $|2\rangle$, without affecting atoms in $|1\rangle$. The microwave pulse is of the order of 10 µs and is performed immediately after the Raman pulse, such that the mixture $|1\rangle, |3\rangle$ remains static. This two-step procedure is more efficient than a direct two-photon transition with $\Delta m = 2$, whose amplitude cancels in the limit of a detuning larger than the hyperfine splitting. With this technique we don't modify the phase of either component.

An example of a soliton generated with the aforementioned protocol is displayed in fig. 2.10. We measure the soliton expansion and determine the stationary atom number N_s. By varying N_2 and analyzing the short-term evolution of the soliton width, we confirm that for $N_2 \approx 400$, the soliton remains stationary over 30 ms as shown in fig. 2.11a. To quantitatively determine N_s, we fit the expansion data to $t \mapsto \sigma_0 + \alpha t^2$ as shown in fig. 2.11b. The stationary soliton condition corresponds to $\alpha = 0$, yielding $N_s \approx 370(60)$ and an interaction parameter of $g_s \approx 4.0(6) \times 10^{-41}$ J m^{-1}, in agreement with theoretical predictions for our geometry. This yields $\xi_s \approx 1.7$ µm, which is close to σ_y, the full width of the tube. This confirms that the system is 1D with respect to the spin degree of freedom, even though it is not for the total density, as $\sigma_y \gg \xi$.

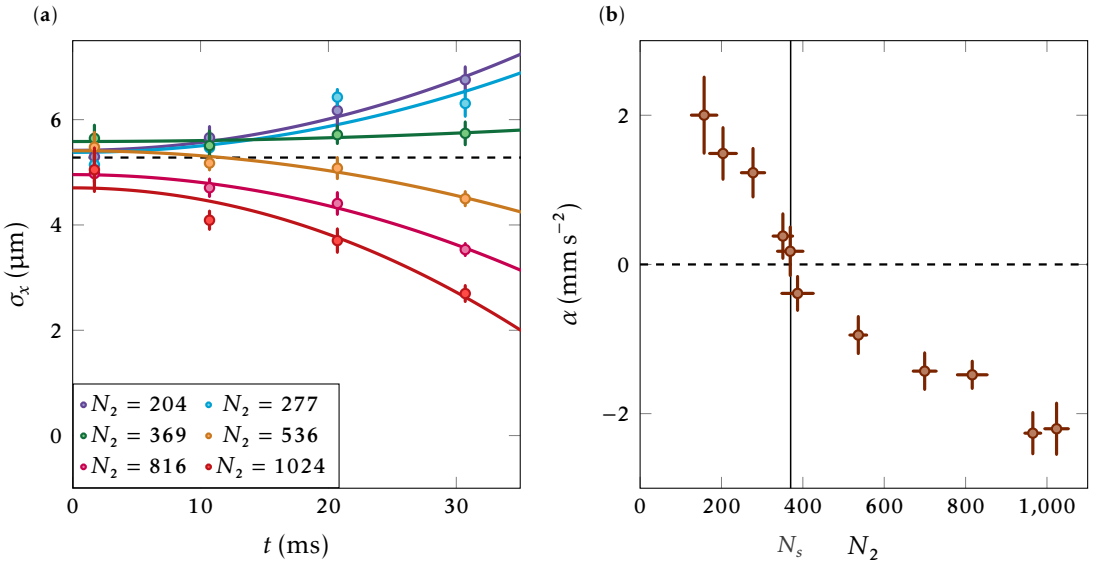

Figure 2.11: (a), We vary the atom number transferred to the minority component and monitor the short-time evolution of the size of the wave packet. Solid lines are fits of the function $t \mapsto \sigma_0 + \alpha t^2$ to the data. The error bars correspond to the statistical error obtained from the fit of the density profiles. (b), Evolution of the expansion coefficient α as a function of the atom number N_2. The value N_s corresponds to the atom number for which the wave packet is stationary. This experiment thus demonstrates the realization of a magnetic soliton at rest.

Conclusion

In this chapter, we established a definition of solitary waves and solitons and provided an overview of matter-wave solitons. We examined the theoretical framework and experimental realizations of matter-wave solitons, starting with bright and dark solitons described by the scalar GPE. Moving beyond single-component systems, we explored dark-bright solitons in two-component BECs, considering both the integrable Manakov regime, with a single interaction parameter, and beyond.

Building on this foundation, we introduced the theoretical framework for magnetic solitons, which constitute the main focus of our experimental work. We then detailed our experimental realization of a magnetic soliton at rest, presenting the first realization of a magnetic soliton in an immiscible mixture.

While this chapter has focused on the static properties of solitons, the next chapter will address the dynamics of magnetic solitons when submitted to a force. A recurring theme throughout this chapter has been the periodicity of energy in momentum, a property that will be at the origin of the remarkable dynamical behavior of magnetic solitons: BOs.

CHAPTER 3

Solitons in motion

Outline of the current chapter

This chapter is adapted from [164]. While the core material remains from the original publication, I have significantly restructured the presentation of it and included supplementary information to better integrate it within the broader framework of the thesis.

Introduction

This chapter explores the dynamics of magnetic solitons in two different geometries: a segment and a ring. In both cases, applying a constant force to the soliton leads to a surprising effect: the oscillation of its position.

We begin by examining solitons in harmonic traps (section 3.1), where they undergo oscillations. This behavior is expected, and it is fundamentally different from the oscillations exhibited by magnetic solitons in the subsequent sections.

We then develop the theoretical framework to describe magnetic solitons under a constant force (section 3.2) and derive a particle-like model for their dynamics. Finally, we present our experimental implementation and calibration of such a force.

We then study the dynamics of a soliton, first, in a segment under a uniform constant force (section 3.3). A parallel is drawn between this situation and Bloch oscillations of a particle in a periodic potential. We then present our experimental observation of soliton CoM oscillations, with matter-wave interference revealing the underlying phase dynamics of the bath.

Next, we investigate the dynamics in a ring geometry, where the behavior becomes even richer (section 3.4). The interplay between oscillatory motion and backflow effects leads to complex phenomena, including the pumping and depumping of topological superfluid currents. We explore both single and multiple soliton configurations, revealing that the generation of topological currents is suppressed in the latter case. Here too, the CoM motion is observed experimentally while matter-wave interference is used to measure quantized supercurrents in the bath.

We conclude by situating our findings within the broader context of one-dimensional systems (section 3.5). Almost all 1D systems presented in this chapter and the previous one exhibit an energy that is periodic in momentum. We prove here that this is a general property of 1D systems in the thermodynamic limit. Since Bloch oscillations stem from this periodicity, they are expected in many such systems. However, they do not necessarily occur in all cases, and we discuss the specific conditions required for their observation.

3.1 Solitons in harmonic traps

3.1.1 Solitons oscillations in harmonic traps

All the dark, bright and dark-bright solitons presented in chapter 2 were realized in traps with a residual axial confinement $V(x) = m\omega^2 x^2/2$, where ω is the trap frequency. For solitons with a dark component, this harmonic potential modifies the functional form of the soliton. In the case of a dark soliton in a harmonic trap, the solution at zero velocity is displayed in fig. 3.1. On top of the modifying the underlying density, if the soliton is not at the center of the trap the harmonic potential exerts a force on it.

The bright soliton is the most straightforward case, as it behaves like a classical particle (*c.f.* section 2.2.2.1) by oscillating at a frequency ω. Bright soliton oscillations have been observed experimentally [121, 122, 124, 129]. For dark solitons, the dynamics are more complex to derive. Provided that the width of the soliton is much smaller than the size of the condensate the soliton oscillates at a frequency $\omega/\sqrt{2}$ [154, 177]. There were

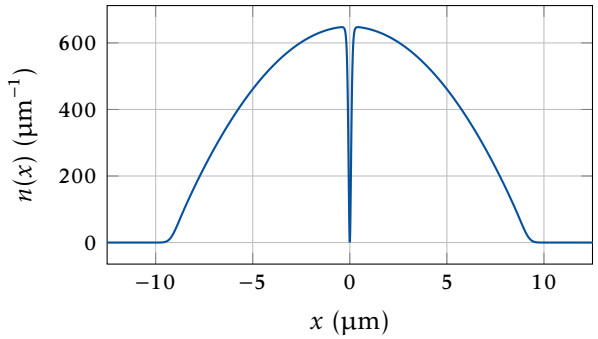

Figure 3.1: Dark soliton in harmonic trap. We plot the density for ^{87}Rb in a cigar-shaped trap with a transverse frequency of $2\pi \times 2$ kHz and longitudinal frequency of $2\pi \times 193$ Hz.

several experimental observations of such oscillations [136, 137, 139, 140, 142]. For dark-bright solitons the dynamics are richer, they are described in ref. [154] and were observed experimentally in ref. [136].

3.1.2 Soliton collisions

When several solitons are placed in a harmonic trap they will collide. Soliton collisions were studied experimentally for bright and bright collisions [121, 124], dark and dark collisions [137, 142], and dark and dark-bright collisions [136]. We recall that in the literature, the term soliton is often used to describe solitary waves, so their shape can be altered by collisions. For example remaining 3D effects can make bright solitons collapse or merge [121, 128, 130]. To the best of our knowledge, collisions between dark-bright solitons have never been studied experimentally, they are studied theoretically in ref. [154, 178–180].

The following sections examine soliton behavior under constant external forces, without harmonic trapping potentials. Unlike the oscillations in harmonic traps discussed previously, the phenomena explored here arise from fundamentally different physical mechanisms and exhibit remarkable properties with an entirely different origin and nature.

3.2 Magnetic soliton submitted to a force

3.2.1 Theory of the magnetic soliton in the presence of a force

We now extend the description of the magnetic soliton from the previous chapter by introducing two forces: $f_1(x)$ and $f_2(x)$ acting respectively on $|1\rangle$ and $|2\rangle$. We define $U_1(x)$ and $U_2(x)$ as the potentials associated respectively to $f_1(x)$ and $f_2(x)$. Rewriting the coupled GPEs including the potentials yields:

$$\mathrm{i}\hbar\frac{\partial\psi_1}{\partial t} = -\frac{\hbar^2}{2m}\frac{\partial^2\psi_1}{\partial x^2} + gn_1\psi_1 + g_i n_2\psi_1 + U_1\psi_1 \tag{3.1a}$$

$$\mathrm{i}\hbar\frac{\partial\psi_2}{\partial t} = -\frac{\hbar^2}{2m}\frac{\partial^2\psi_2}{\partial x^2} + gn_2\psi_2 + g_i n_1\psi_2 + U_2\psi_2. \tag{3.1b}$$

We obtain the associated equations on (θ, φ), eq. (2.42), but with additional terms due to the potentials:

$$\partial_{\tilde{t}}\,\theta = -2\cos(\theta)(\partial_{\tilde{x}}\varphi)(\partial_{\tilde{x}}\theta) - \sin(\theta)\partial_{\tilde{x}}^2\varphi - \tilde{J}\partial_{\tilde{x}}\theta \tag{3.2a}$$

$$\partial_{\tilde{t}}\,\varphi = -\cos(\theta)\left[1 + (\partial_{\tilde{x}}\varphi)^2\right] + \frac{\partial_{\tilde{x}}^2\theta}{\sin(\theta)} - \tilde{J}\partial_{\tilde{x}}\varphi + n_0\xi_s\left(\tilde{U}_2 - \tilde{U}_1\right). \tag{3.2b}$$

Only the second equation has an additional term due to the presence of the forces. Moreover, the dynamics only depend on the relative potential $U = U_2 - U_1$. We also define $f = f_2 - f_1$, the relative force. We do not attempt to solve eq. (3.2) analytically due its complexity. Instead, to study the influence of the force on the soliton we make the adiabatic approximation, that supposes that all the atoms in the soliton feel the same potential, *i.e.* $F\sigma \ll gn_0$, σ being the size of the soliton. This condition is given by Kosevich *et al.* in ref. [181] and is equivalent to assuming that the work done by the force across the wave packet extension is much smaller than the spin interaction energy scale. On top of that, we assume the system size L satisfies $L \ll ct_{\text{char}}$, where t_{char} is the characteristic timescale of soliton dynamics and $c = \sqrt{gn_0/m}$ is the speed of sound for density modes. Since density perturbations equilibrate through phonons over a time $\tau = L/c$, our assumption ensures $\tau \ll t_{\text{char}}$. Consequently, on the slow timescale of spin dynamics, the bath (including its phase) remains in quasi-static equilibrium, which justifies our initial assumption of decoupled density and spin modes and thus a space-independent total current. These two assumptions guarantee that even with the presence of the forces, the solution remains a soliton described by eq. (2.52). Because of the force, Ω and $\tilde{u}$ are time-dependent. However, $\tilde{N}$ remains constant, such that Ω and $\tilde{u}$ vary along the ellipse described in fig. 2.9. To study the dynamics we rely on a Hamiltonian approach. The energy of the soliton given in eq. (2.58) has[1], in the presence of the forces, the following additional term:

$$\begin{aligned}\int \tilde{U}_1(\tilde{x})\cos^2\left(\frac{\theta(x)}{2}\right) + \tilde{U}_2(\tilde{x})\sin^2\left(\frac{\theta(x)}{2}\right)\mathrm{d}\tilde{x} &= \int \tilde{U}_1(\tilde{x}) + \left(\tilde{U}_2(\tilde{x}) - \tilde{U}_1(\tilde{x})\right)\sin^2\left(\frac{\theta(x)}{2}\right)\mathrm{d}\tilde{x} \\ &\approx \int \tilde{U}_1(\tilde{x})\mathrm{d}\tilde{x} + \tilde{U}(\tilde{X})\tilde{N},\end{aligned} \tag{3.3}$$

where $\tilde{X}$ is the position of the center of the soliton. In the last equality, we used the adiabatic approximation to neglect the potential variation over the extent of the soliton. The first term of the rhs of the last equation is constant, we can offset the energy to get rid of it. The energy of the soliton in the presence of the force then reads:

$$\tilde{E}(\tilde{N}, \tilde{P}, \tilde{X}) = 2\tanh(\tilde{N}/2) + 4\frac{\sin^2(\tilde{P}/2)}{\sinh(\tilde{N})} + \int \mathrm{d}\tilde{x}\,\tilde{J}^2/4 + \tilde{N}\tilde{U}(\tilde{X}). \tag{3.4}$$

$\tilde{E}$ is, like $\tilde{N}$, a conserved quantity and can be seen as the Hamiltonian of the magnetic soliton. In this particle-like model, the soliton is viewed as a single particle with position $\tilde{X}$ and momentum $\tilde{P}$, with dynamics governed by the Hamiltonian $E(\tilde{N}, \tilde{P}, \tilde{X})$. Using the Hamilton-Jacobi equations we find that $\tilde{P}$ is not conserved in the presence of the forces and evolves according to:

$$\frac{\mathrm{d}\tilde{P}}{\mathrm{d}\tilde{t}} = -\tilde{N}\left.\frac{\mathrm{d}\tilde{U}}{\mathrm{d}\tilde{x}}\right|_{\tilde{X}} \tag{3.5}$$

[1]This expression remains valid because we supposed that the profile remains a magnetic soliton.

which is simply Newton's law:

$$\frac{\mathrm{d}\tilde{P}}{\mathrm{d}\tilde{t}} = \tilde{\mathcal{F}}, \tag{3.6}$$

where $\tilde{\mathcal{F}} = \tilde{N}\tilde{f}$.

3.2.2 Experimental implementation of the force

3.2.2.1 Magnetic gradient

We apply a constant, uniform force to the system using an external magnetic field with a linear variation along x. This magnetic field gradient b', of typical amplitude $1\,\mathrm{G\,m^{-1}}$, is switched on slowly before the partial transfer of atoms to the minority component. The associated force is opposite for the states $|1\rangle$ and $|2\rangle$ because of their opposite magnetic moments $\pm\mu_B/2$, with μ_B the Bohr magneton. The differential force between the two species is thus $f = \mu_B b' \sim 1 \times 10^{-27}$ N. The associated energy difference between both ends of the system is $\sim \mu_B b' L \sim 1$nK, which is small compared to all other relevant energy scales in the problem. We transfer part of the atoms from $|1\rangle$ to $|2\rangle$ at time $t = 0$. Atoms in state $|2\rangle$ thus experience an abrupt application of the force. We verified numerically that in the range of parameters explored in this work, the dynamics of the wave packet is given by the difference of force f between the two components as predicted by section 3.2.1.

3.2.2.2 Calibration of the force

We calibrate the magnetic field gradient b' by performing Ramsey spectroscopy. We use a microwave field at a frequency of $\approx 6.8\,\mathrm{GHz}$, resonant with the $|F = 1, m_1 = -1\rangle \rightarrow |F = 2, m_2 = -2\rangle$ transition. This transition being magnetic-field-sensitive, the magnetic field gradient causes a spatial dependence of the transition frequency. We measure it performing two identical microwave pulses, separated by a wait time t_w. We then image the $|F = 1, m_1 = -1\rangle$ component and observe interference fringes with a spatial period Λ. The magnetic gradient is given by:

$$|b'| = \left| \frac{h}{\Lambda t_w \mu_B (g_1 m_1 - g_2 m_2)} \right| = \left| \frac{2h}{3\Lambda t_w \mu_B} \right|, \tag{3.7}$$

where h is the Planck constant and $g_{1,2} = \pm 1/2$ the Landé factors [86].

3.3 Bloch Oscillations of a magnetic soliton in a segment geometry

We will start by studying the dynamics with strict boundary conditions. For the segment geometry the force $\tilde{f}$ is assumed to be uniform. Prior to returning to our analysis of magnetic solitons, we will digress briefly to introduce the physical phenomenon of Bloch oscillations, which provides essential context for the subsequent theoretical and experimental development.

3.3.1 Bloch Oscillations in the presence of a periodic potential

A single isolated particle moving in a lattice with spatial period a and subjected to a constant force f exhibits BOs [58, 59] with a period:

$$T_B = \frac{h}{af}. \tag{3.8}$$

This peculiar motion is due to the periodicity of the lattice band structure. The dynamics in momentum space correspond to periodic Bragg reflections of the particle when its wavelength matches the period of the lattice. The observation of BOs requires phase coherence during the oscillations and a force weak enough to ensure the adiabatic following of the lowest energy band. It has been observed in ultracold atom platforms [63, 64, 182] as well as in semiconductor structures with large lattice periods [61].

BOs at the single-particle level are extensively used in cold atom experiments for precision measurements [66, 70, 72, 73] and for characterizing the topological properties of band structures [74, 75]. Classical analogues of BOs have also been realized with optical [183, 184] and acoustic waves [185] and in plasmonic waveguide arrays [186].

While BOs are well understood for single particles, their generalization to an ensemble of interacting particles remains largely unexplored. In such systems, interactions often lead to unwanted damping of the oscillations [187–190]. Studies of BOs of a weakly-bounded ensemble of interacting particles have been limited to the two-particle case, where the oscillation period is halved compared to the single-particle case. This behavior has been observed both with repulsively-bound dimers [191] and in photonic simulations using waveguide arrays [192]. Recent work has also explored the role of quantum anyonic statistics through electrical circuit simulations [193]. In the following sections, we extend these studies by observing the position oscillations of a mesoscopic solitonic wave packet containing approximately 1000 atoms.

3.3.2 Theory of the dynamics

3.3.2.1 Equations of motion

We have already written one of the Hamilton-Jacobi equations that can be derived from eq. (3.4) in eq. (3.5). For strict boundary conditions we remind that $\tilde{f}$ vanishes at all times so that $\tilde{P} = \Delta\Phi_1$ and eq. (3.5) becomes :

$$\frac{\mathrm{d}\Phi_1}{\mathrm{d}\tilde{t}} = \tilde{\mathcal{F}}. \tag{3.9}$$

With the second Hamilton-Jacobi equation, we find $\partial_t \tilde{X}$, and by integration:

$$\tilde{X}(\tilde{t}) = \tilde{X}(0) + 2\frac{1-\cos\left(\tilde{\mathcal{F}}\tilde{t}\right)}{\tilde{\mathcal{F}}\sinh\left(\tilde{N}\right)}. \tag{3.10}$$

Equation (3.10) describes a situation analogous to the above-mentioned BOs: when the soliton is submitted to a constant force $\tilde{f}$ it oscillates; with the key difference that the periodic potential is absent in this case.

Concerning the evolution of the spatial profile of the soliton, eq. (3.9) tells us that during the dynamics, the ellipse of fig. 2.9 is explored at a constant angular velocity, and Ω, v are periodic functions of time. In the experiment we start at time $t = 0$ with the solution $\Omega < 0, v = 0$ (at the bottom of the ellipse) so at every odd-numbered half-period the soliton is described by the solution $\Omega > 0, v = 0$ (at the top the ellipse) which features a

full depletion of the bath and a π phase jump of Φ_1. At every even-numbered half-period the spatial profile is the same as the initial one.

The period and full amplitude of the oscillation are given by:

$$\tilde{T} = \frac{2\pi}{\tilde{\mathcal{F}}} \tag{3.11}$$

$$\tilde{\mathcal{A}} = \frac{4}{\tilde{\mathcal{F}}\sinh(\tilde{N})}, \tag{3.12}$$

converted to physical units using table 2.1, they read [169, 194]:

$$T = \frac{n_0 h}{N_2 f} \tag{3.13}$$

$$\mathcal{A} = \frac{4 g_s n_0^2 \xi_s}{N_2 f \sinh\left(N_2/(n_0\xi_s)\right)}. \tag{3.14}$$

Equation (3.13) is reminiscent of eq. (3.8) but with two major differences: (i) the lattice period a is replaced by the inverse of the linear bath density n_0 and (ii) in our case, T depends on the total force $\mathcal{F} = N_2 f$ acting on the atoms of the wave packet.

BOs of a single particle in a periodic potential and the oscillations of a magnetic soliton in a segment derive from one peculiar property that both systems have in common: the periodicity of E with respect to P. For this reason we decide to use the term Bloch Oscillation also for the magnetic soliton dynamics. However, in this case the oscillation period scales inversely with the atom number, thus revealing its collective nature and generalizing the two-particle case where a halving of the frequency was observed [191, 192].

3.3.2.2 Josephson junction analogy

We have shown previously that the equations of motion of the soliton can be derived from a Hamiltonian approach. In this subsection, we present a physical interpretation of the dynamics of the magnetic soliton in a segment geometry through an analogy with Josephson junctions [169, 195]. While this analogy is not as rigorous as the Hamiltonian formulation, we believe it offers a more intuitive perspective on the phenomenon. The physical situation is described in fig. 3.2. Thanks to the decoupling of the density and spin modes, a quasi-static equilibrium is reached on a timescale associated with the propagation of sound at a velocity $c = \sqrt{g n_0/M}$ corresponding typically to $L/c \approx 20\,\mathrm{ms}$, much smaller than the Bloch oscillation period. The total density is thus uniform at all times and the phase of the bath is quasi-uniform on either side of the wave packet. Equivalently, there is no current flowing in the system outside the region of the wave packet, as we saw in section 2.3.3.5. The minority component wave packet moves with a velocity $v(t)$ as a response to the external force $\mathcal{F}$. This leads to a change of the density distribution of the bath associated with the current $I(t) = -n_0 v(t)$. As we have seen previously, the momentum of the soliton is linked to the phase difference $\Delta\Phi_1 = \Phi_{1,L} - \Phi_{1,R}$ in the bath between the two ends of the wave packet through $P(t) = n_0 \hbar \varphi$. Finally, applying Newton's law, we have $\mathrm{d}P/\mathrm{d}t = \mathcal{F}$, and we obtain

$$\hbar \frac{\mathrm{d}\Delta\Phi_1}{\mathrm{d}t} = \frac{\dot{P}(t)}{n_0} = \frac{\mathcal{F}}{n_0}. \tag{3.15}$$

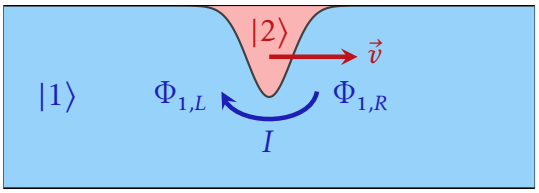

Figure 3.2: Principle of the experiment. A two-component system with total constant density is driven by a constant force which imparts to the wave packet of atoms in $|2\rangle$ a velocity $\boldsymbol{v}$. The motion of this wave-packet induces a current I in the bath to keep the total density constant. This current is associated to a phase difference $\Delta\Phi = \Phi_{1,L} - \Phi_{1,R}$ in the bath.

In addition, as we saw previously, for strict boundary conditions the energy of the soliton is periodic in momentum. This property ensures that the velocity $v(t) = \partial E/\partial P$ is a periodic function of P, or equivalently of $\Delta\Phi_1$. For the studied soliton, this dependence is sinusoidal and given by

$$v(t) = v_c \sin[\Delta\Phi_1(t)] = v_c \sin\left(\frac{\mathcal{F}t}{\hbar n_0}\right). \tag{3.16}$$

This is similar to the current/phase relationship of a Josephson junction where $v_c = 2c_s/\sinh(N_2/n_0\xi_s)$ and $c_s = \sqrt{g_s n_0/(2M)}$ can be found using the Hamiltonian approach [169]. This system is thus analogous to a Josephson junction where the wave packet plays the role of a mobile tunnel barrier between two superfluids of order parameter $\sqrt{n_0}\,e^{i\Phi_{1,R/L}}$, and the force analogous to a potential drop drives a phase difference between them. Remarkably, the energy $n_0\hbar v_c$, equivalent to a tunneling energy, is independent of the time-varying shape of the wave packet. From the 2π periodicity of $\Delta\Phi_1(t)$ and eq. (3.15), we also recover the oscillation period introduced in eq. (3.13).

3.3.3 Experimental observation of Bloch Oscillations

3.3.3.1 Center-of-Mass dynamics

We study the response of the magnetic soliton to a state-selective constant force f, focusing first on the CoM dynamics of the wave packet. We report the observation of BOs in fig. 3.3 for a wave packet of 1300(50) atoms subjected to a force of $f = 9.0(7)\times10^{-28}\,\mathrm{N} = 6.4(5)\times10^{-4}\,Ma_G$, where a_G is the acceleration of gravity. The measured period $T = 219(3)\,\mathrm{ms}$ agrees well with the expected value of 210(16) ms. Similar BOs are observed for different values of N_2 and f and the measured period shown in fig. 3.4a matches the predicted $1/(N_2 f)$ scaling of eq. (3.13) without any fitting parameter. The agreement of the measured amplitude with its prediction, given by eq. (3.14) is shown in fig. 3.4b. It is interesting to emphasize that the period T is independent of the interaction parameters g and g_i, thus making it a robust observable. We verify that the adiabatic approximation is justified in our case : $f\sigma/(g_s n_0) \sim 0.1$ and that $L/c \approx 20\,\mathrm{ms}$ is smaller than the typical Bloch oscillation period for our system. Note that the typical value of N_s used for the static soliton experiment (≈ 400) is different from the one used here (≈ 1200) in order to make the system behavior (expansion or contraction) less sensitive to the variation in atom number (see fig. 2.6).

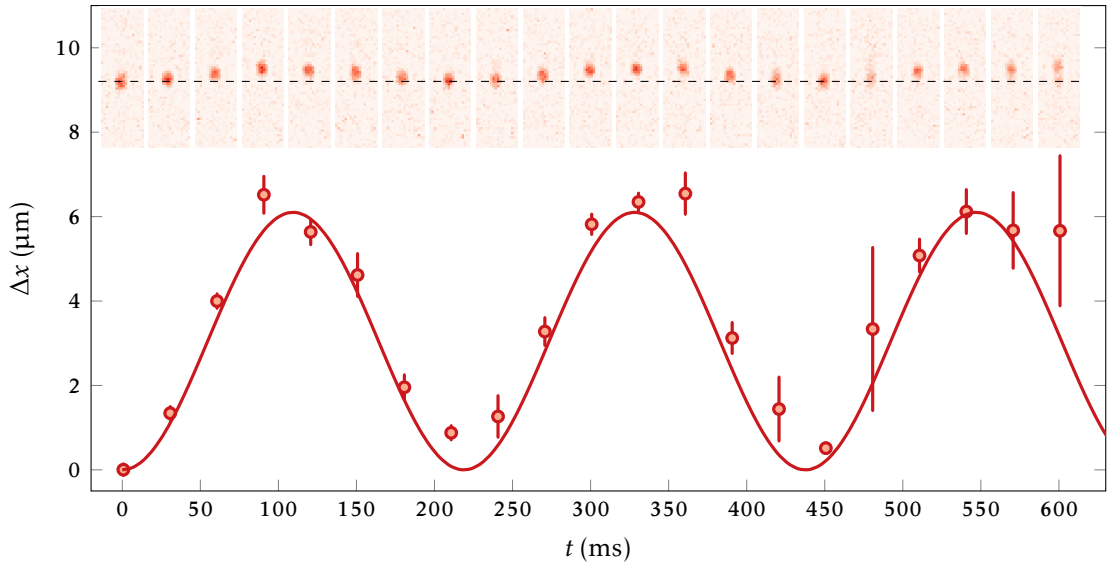

Figure 3.3: Time evolution of the minority component in $|2\rangle$ for $N_2 = 1300(50)$ atoms, $n_0 \approx 350\,\mu\text{m}^{-1}$ and under the action of a uniform differential force of $f = 9.0(7) \times 10^{-28}$ N, showing the phenomenon of Bloch oscillations. The error bars correspond to the statistical deviation obtained from 10 repetitions of each experiment. The solid line is a sinusoidal fit to the data. Absorption images are shown every 30 ms from the initial preparation of the wave packet. The dashed line is a guide to the eye to mark the initial position of the wave packet.

3.3.3.2 Bath phase

We experimentally confirm the role of the bath phase Φ_1 using matter-wave interference [196–198] (see fig. 3.5). We prepare a second reference cloud next to the cloud of interest, the edges of the two clouds are 4 µm apart. This cloud is identical to the first one, but it contains only atoms in $|1\rangle$ and constitutes a suitable uniform phase reference for the low-temperature regime studied here. After releasing the two clouds from the trap and allowing them to expand and overlap, we obtain matter-wave interference images. Several examples of those interferograms are displayed in fig. 3.5, we mention that to increase the signal-to-noise ratio of the fringes we saturate the imaging. The ToF sequence optimizing the fringe visibility is the following. We first reduce the power of the vertical lattice by a factor 7, 160 µs after, the in-plane box-like confinement is turned off, and the cloud expands with the vertical lattice still on during 3 ms. Finally, the vertical lattice is switched off and the cloud freely expands during 4 ms.

At time $t \approx 0$, we expect both clouds to have a uniform phase, which is confirmed by the observation of straight and parallel fringes. At times $t \approx T/2$ and $t \approx 3T/2$, conversely, we observe a contrasted density hole in the vicinity of the wave packet position associated with a discontinuity in the fringes. This is consistent with the expected full depletion of the bath density at this position and the π phase jump at these times. Thus, we have realized the second zero-velocity soliton of the family of magnetic solitons, *i.e.* the one at the top of the ellipse in fig. 2.9.

The phase difference $\Delta\Phi_1$ can be quantitatively measured from the interferograms. We first process the images using a Goldstein filter [199] to reduce noise, then apply a Hilbert transform to extract the phase information row by row. The region exhibiting the most rapid phase variation corresponds to the location of the atoms in state $|2\rangle$, when $\Delta\Phi_1$ is

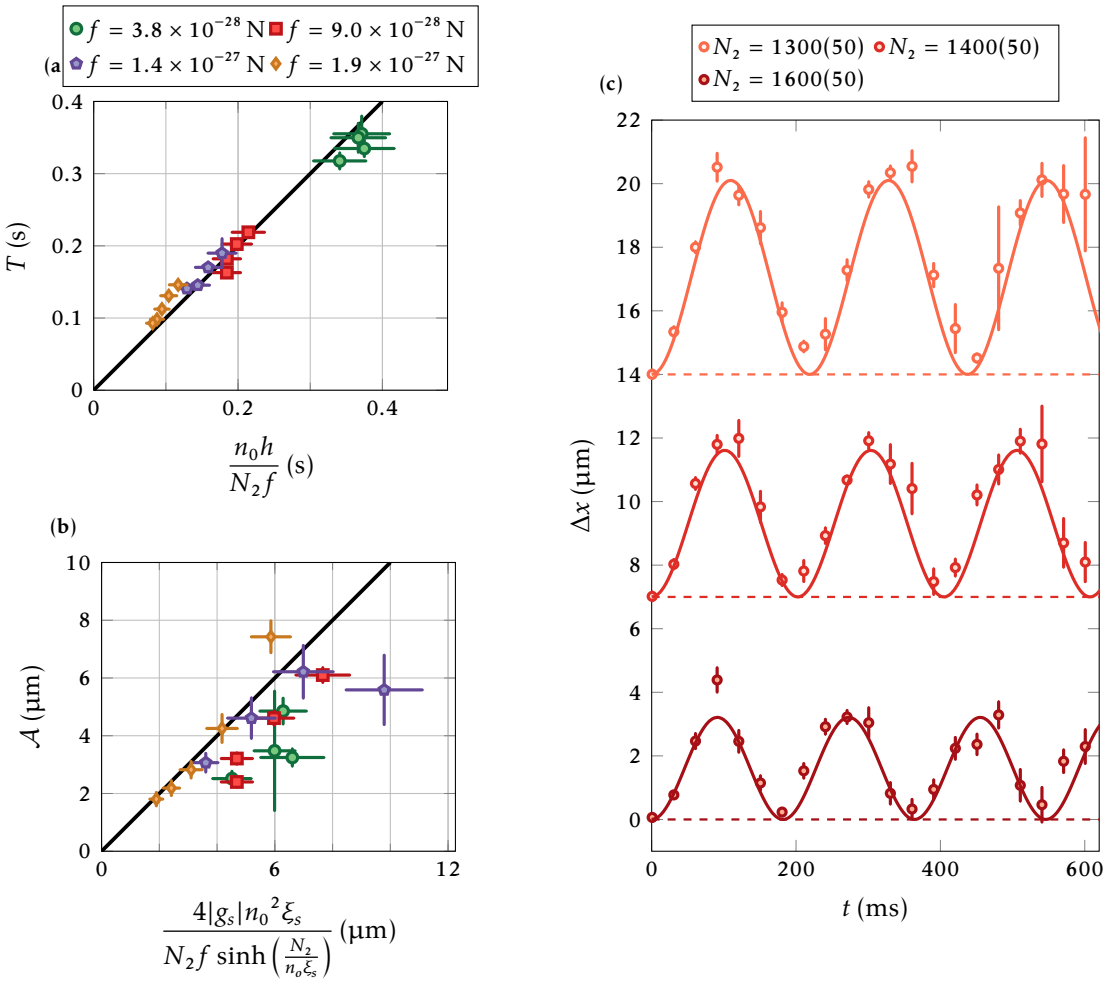

Figure 3.4: (a), Measured Bloch period and (b) amplitude when varying N_2 and the applied magnetic field gradient b', which creates the force $f = \mu_B b'$. The different colors correspond to different forces applied on the soliton. The linear bath density n_0 is fixed. The solid black line is the prediction of eq. (3.13) without any free parameter. (c), CoM oscillations of component $|2\rangle$ with a fixed force $f = 9.0 \times 10^{-28}$ N and n_0 and varying N_2. As N_2 increases the period and amplitude of oscillations decrease.

sufficiently large. By computing the phase difference across this region, we obtain the results displayed in fig. 3.5b.

3.4 Bloch Oscillations of a magnetic soliton in a ring geometry

We now study the dynamics of a soliton placed inside a ring. The transition from a segment geometry to a ring geometry introduces two significant modifications. First, the boundary conditions change from strict to periodic, as a direct consequence of the closed ring structure, allowing an overall current to flow. Second, while we maintain a uniform force in the plane as for the segment, its projection along the ring is no longer uniform. The force experienced by the atoms thus changes. Specifically, the projection of the force along the direction of motion is expressed as $f(\alpha) = f_0 \cos(\alpha)$, where α is the angle describing the position of the wave packet, so that the position is given by $X = \frac{\alpha}{2\pi} L$. The perimeter of the ring is set to $L = 150\,\mu\text{m}$.

3.4.1 Theory of the dynamics

3.4.1.1 Equation of motion

The energy of the system in the presence of the force for the ring reads:

$$\tilde{E}(\tilde{N}, \tilde{P}, \tilde{X}) = 2\tanh(\tilde{N}/2) + 4\frac{\sin^2(\tilde{P}/2)}{\sinh(\tilde{N})} + \frac{\tilde{P}^2}{\tilde{L}} - \tilde{f}_0 \tilde{N} \frac{\tilde{L}}{2\pi} \sin(2\pi\tilde{X}/\tilde{L}). \tag{3.17}$$

The Hamilton-Jacobi equations read:

$$\frac{\mathrm{d}\tilde{P}}{\mathrm{d}\tilde{t}} = \tilde{N}\tilde{f}_0 \cos\left(\frac{2\pi\tilde{X}}{\tilde{L}}\right) \tag{3.18a}$$

$$\frac{\mathrm{d}\tilde{X}}{\mathrm{d}\tilde{t}} = \frac{2\sin(\tilde{P})}{\sinh(\tilde{N})} + \frac{2\tilde{P}}{\tilde{L}}, \tag{3.18b}$$

the first equation being simply Newton's law. Unlike the segment case, the coupled differential equations have no easy analytical solutions, we will solve them numerically. To benchmark the particle-like model, we conducted numerical simulations. Figure 3.6 presents a quantitative comparison between this model in a ring geometry and the numerical solution of the GPE. The excellent agreement between these two models confirms, in the range of parameters studied in this work, the validity of describing the solitonic wave packet motion through the particle-like model within the adiabatic approximation.

3.4.1.2 The role of the backflow

As we have seen in section 2.3.3.5, the strong spatial variation of the phase of the bath across the wave packet position is compensated by a slow linear variation over the rest of the ring. It leads to a so-called backflow current, which carries the total momentum $\tilde{P} = \hbar\Delta\Phi_1$ of the system as we showed in section 2.3.3.5. This global current was not allowed in the previous case of the segment with hard walls. The second term of the rhs of eq. (3.18b) reflects the acceleration of the wave packet induced by the backflow current and goes to zero in the thermodynamic limit. The adiabatic dynamics under the application of a constant force thus consists in an interplay between an oscillatory behavior and the drag effect induced by the backflow current. The typical evolution of the phase profile obtained from simulations of the GPE is shown in fig. 3.7. Interestingly, after one

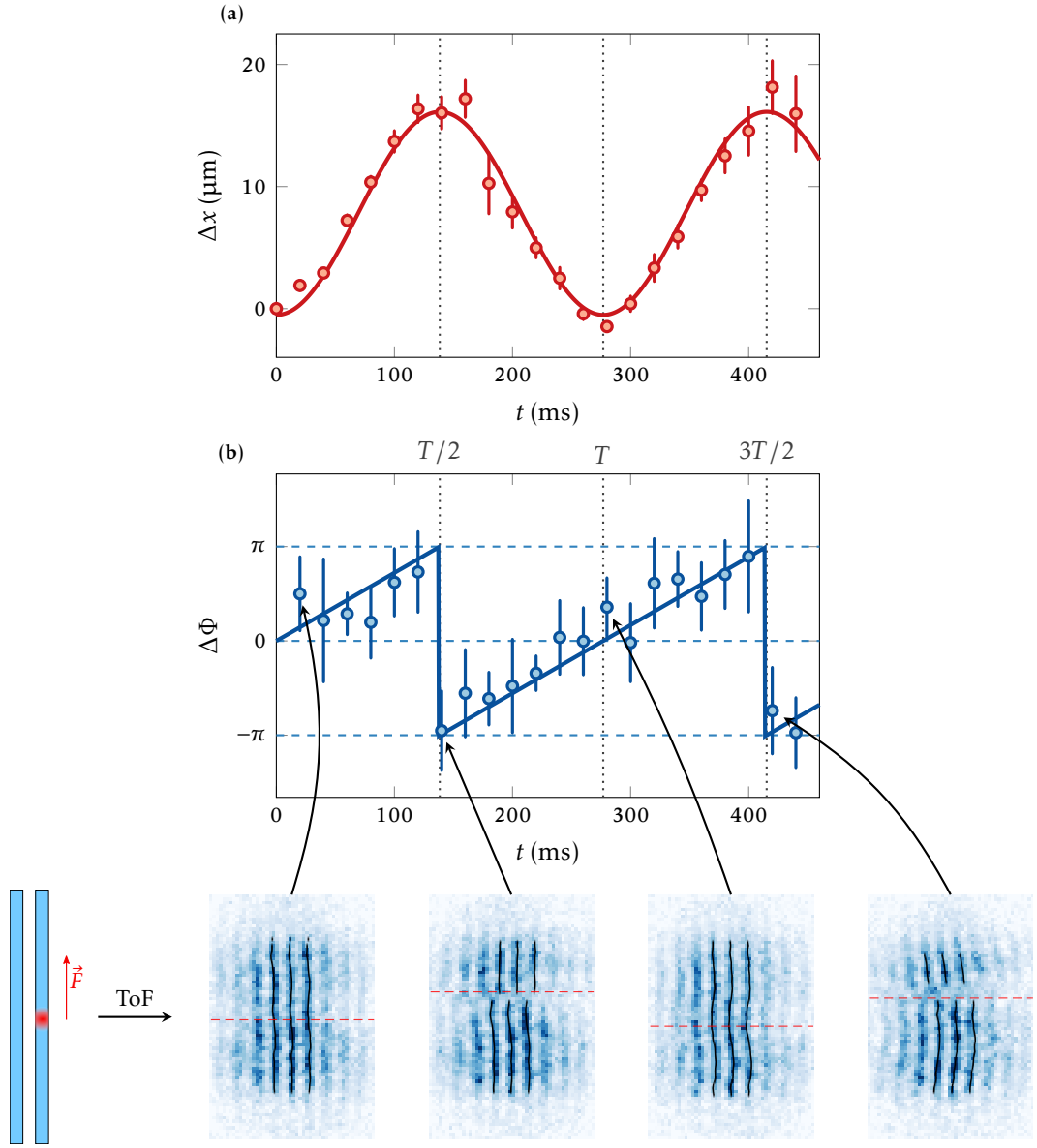

Figure 3.5: Combined evolution of the CoM of the wave packet and the phase difference $\Delta\Phi_1$ in the bath. (a), Evolution of the CoM of component $|2\rangle$ for a force $f = 9.0(7)\times10^{-28}$ N and a typical density. The points are obtained by imaging atoms in $|2\rangle$, the solid line is a sinusoidal fit. (b) shows the corresponding phase jump in $|1\rangle$, obtained by imaging atoms in $|1\rangle$ after performing the expansion sequence described in the text. The phase difference $\Delta\Phi_1$ is computed using the interferograms, the solid line is the linear phase evolution obtained using the fitted frequency from (a). We display below (b) some example images of interferograms. The black lines are the reconstructed positions of the bright fringes. The red dashed lines show the position of the soliton measured independently. A discontinuity of the fringes, corresponding to a π-phase shift of the phase of the bath, is observed at the positions where the wave packet's velocity changes from positive to negative. On both graphs the vertical lines indicate integer multiples of $T/2$, with T being the fitted period of the oscillation in (a).

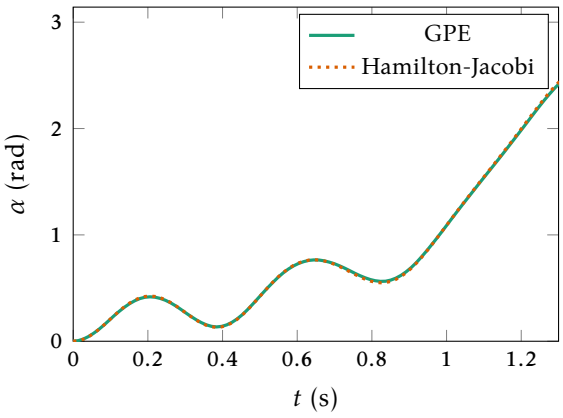

Figure 3.6: Benchmarking of the particle-like model in a ring geometry to the direct solving of the GPE. Time evolution of the position of the CoM of the wave packet when subjected to a constant force with $N_2 = 1100$, $b' = 1\,\mathrm{G\,m^{-1}}$, $n_0 = 330\,\mu\mathrm{m}^{-1}$. The green solid line is the CoM of the wave packet obtained by solving the GPE. The dashed orange line is the prediction of the particle-like model.

half-period the profile winds once around the ring. This corresponds to the creation of a topological superfluid current around the ring, induced by the motion of the wave packet. Our system thus realizes a new example of a vortex pump [200–202].

3.4.2 Experimental observation of short-term dynamics

We start by studying the dynamics for angles $\alpha \ll \pi/2$. In this regime, we can neglect the angular dependence of the force, *i.e.* $f \approx f_0$, and the speed of the soliton is:

$$\tilde{v} \approx \frac{2\sin(\tilde{N}\tilde{f}_0\tilde{t})}{\sinh(\tilde{N})} + \frac{2\tilde{N}\tilde{f}_0\tilde{t}}{\tilde{L}}, \tag{3.19}$$

or in physical units:

$$v \approx \frac{2c_s}{\sinh\left(\frac{N_2}{n_0\xi_s}\right)} \sin\left(\frac{N_2 f_0 t}{\hbar n_0}\right) + \frac{N_2 f_0 t}{L m n_0}. \tag{3.20}$$

So that in this limit the backflow causes a drag at constant speed $v_b = \frac{N_2 f_0}{L m n_0}$

3.4.2.1 Our experimental realization with one soliton

We consider first the dynamics of a single soliton subjected to a uniform force oriented in the plane of the ring. We measure both the position α (*c.f.* fig. 3.8a) of the wave packet and the phase winding number $w = \int_0^{2\pi} \mathrm{d}\alpha\, \partial_\alpha \Phi_1(\alpha)/(2\pi) \in \mathbb{Z}$ of the bath (*c.f.* fig. 3.8b). For the former, we use matter-wave interferometry, as we did for the segment geometry. We use a two-ring geometry. The inner ring serves as a phase reference where all the atoms are in $|1\rangle$ (*c.f.* fig. 3.8c). The soliton is prepared in the outer ring. To create this geometry we start with a 30 µm disk. This disk is then shrunk dynamically by displaying a movie on the DMD. We obtain a ring of inner radius 16 µm and outer radius 25 µm. Then, we split this ring into two rings by adding a 3 µm thick circular barrier with a central radius of 20.5 µm. This procedure is meant to avoid supercurrents in either of the two rings [198].

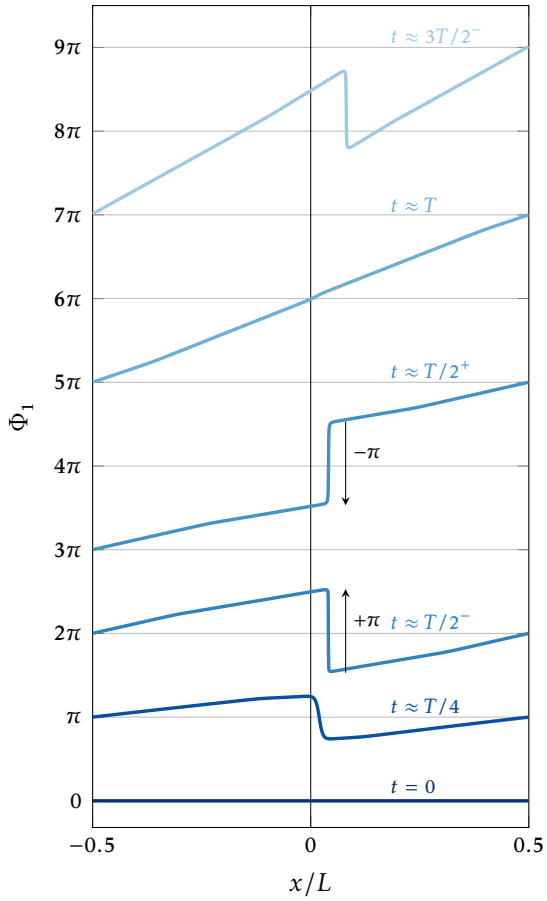

Figure 3.7: Phase of the bath for a soliton in a ring obtained with GPE simulations. The parameters used for the simulation are, $L = 150\,\mu\text{m}$, $g = 2.96 \times 10^{-39}\,\text{J m}^{-1}$, $g_i = 1.0135\,g$, $n_0 = 333\,\mu\text{m}^{-1}$, $N_2 = 1300$ and $b' = 1\,\text{G m}^{-1}$. Periodic boundary conditions impose the same phase on both sides of the ring. Just after $t = T/2$, the phase profile winds once around the ring leading to the creation of a supercurrent in the bath.

We estimate the frequency of unwanted windings around 4%. To obtain the winding number, we make the reference ring interfere with the other ring. We lower the power of the vertical optical lattice by a factor 3, we then switch off the in-plane confinement during 4.5 ms before doing a 1 ms time-of-flight in the absence of the residual vertical confinement. We finally perform absorption imaging to observe the interference patterns and determine the winding number w of the spiral patterns. Examples of such patterns are displayed in fig. 3.8d-f, like in the segment geometry we saturate the imaging to increase the visibility of the fringes.

As expected, the wave packet exhibits an oscillatory motion, accompanied by a constant acceleration induced by the backflow. Each time the wave packet's velocity becomes negative, we observe a jump of one unit in the phase winding of the bath. The solid lines on both $\alpha(t)$ and $w(t)$ are obtained from the equations of motions of the particle-like model deduced from eq. (3.18). They are in excellent agreement with our data. In section 3.4.3 we will extend this study to the long-time dynamics, for which the angular dependence of f_α plays a significant role.

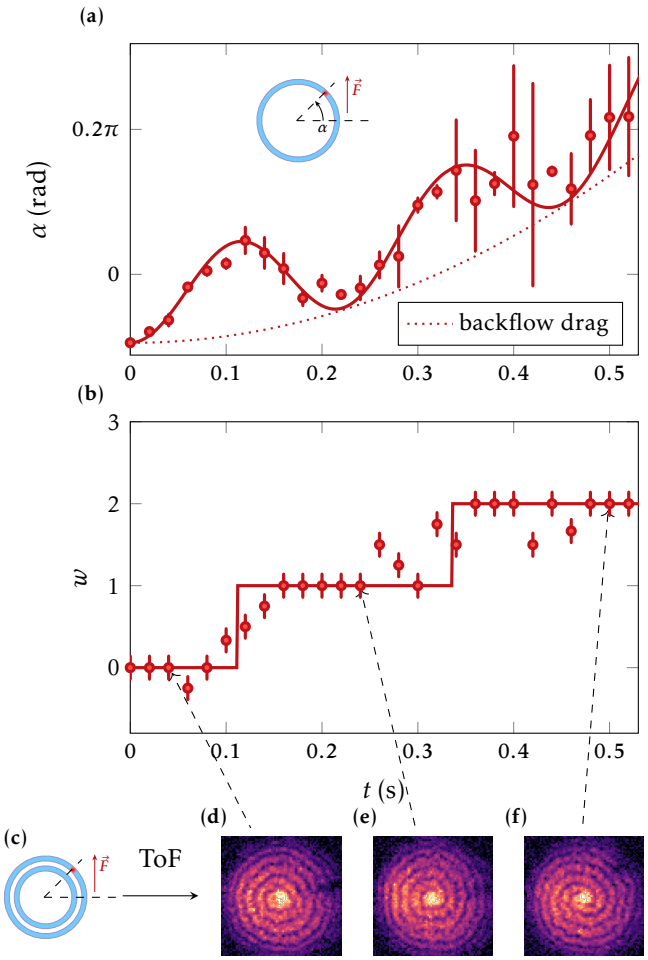

Figure 3.8: Oscillation of a magnetic soliton under a constant force in a ring geometry. (a), Time evolution of the polar angle α associated with the position of the soliton along the ring (see the sketch in the inset) for $N_2 = 1100(60)$, $n_0 = 320(10)\,\mu\text{m}^{-1}$ and $f = 9.0(7)\times10^{-28}$ N. The soliton performs Bloch-like oscillations combined with an additional variation of the CoM position due to the generation of a backflow in the ring. The solid line is the prediction from the particle-like model. The dotted line is $v_b t^2/2$, the drag due to the backflow. (b), Time evolution of the winding number w of the bath phase. The latter is measured using matter-wave interference fringes obtained after an expansion from the configuration sketched in (c) with two concentric rings. Just after $t = T/2$, the phase profile winds once around the ring leading to the creation of a supercurrent in the bath. Absorption images of the fringes at three different times are shown in (d), (e), (f). We observe concentric rings (d), an anticlockwise spiral pattern (e) and an anticlockwise double spiral pattern (f), which we assign to $w = 0$, $w = 1$ and $w = 2$, respectively. The error bars represent the expected statistical errors for 4 repetitions of the experiment when the residual probability to measure a relative winding between the two rings without any soliton in the system has been estimated to be $\approx$ 4%.

3.4.2.2 Our experimental realization with two solitons

To further investigate the soliton dynamics in a ring, we performed an experiment with two identical solitons, initially positioned diametrically opposed to one another. Their positions are defined by the angles α_L and α_R with respect to their initial positions. As illustrated in fig. 3.9a, the solitons exhibit synchronized oscillations as expected from the relative orientation of the force applied to them. No additional acceleration of the solitons' positions is observed in this case. This is consistent with the measurement of the bath phase winding (*c.f.* fig. 3.9b-d) which shows no significant creation of superfluid currents. This behavior reflects that the current generated by each soliton motion are opposite in sign and thus cancel each other out. We conclude by mentioning that similar dynamics were later predicted for a single or a pair of dark-bright solitons, outside the Manakov limit, in a ring [203].

3.4.3 Experimental observation of long-term dynamics

In this subsection, we discuss the long-time dynamics of a single soliton in a ring, where the angular dependence of f_α now plays a role. The position of the wave packet and the winding evolution are shown in fig. 3.10a and fig. 3.10b, respectively. The time range studied experimentally is limited to ≈ 1 s by atom losses and finite temperature effects. Oscillations with a drift are also observed, and the winding number increases up to $w = 3$. The additional feature with respect to the situation explored in the previous subsection is the decrease of the winding number w when $\alpha > \pi/2$. Indeed, in this range, $f_\alpha < 0$ and Bloch-like oscillations induce a depumping of the topological current. These observations are in excellent agreement with the predicted equations of motion of the particle-like model shown as a solid line.

We extend the study of the long-time evolution theoretically using the phase portrait (α, P) shown in fig. 3.10c. The motion of the wave packet, represented by the violet line, corresponds to a constant energy curve. After the first part of the experimentally observed evolution (solid line), the wave packet reaches $\alpha = \pi$ with $w = 0$. The wave packet then returns to $\alpha = 0$ (dashed line) with a winding that first decreases to $w = -3$ and then returns to its initial value of $w = 0$. We thus have a long-time periodic evolution that combines fast Bloch-like oscillations with a slower evolution determined by the angular dependence of the force and the backflow, which finally leads to a global strictly periodic evolution with a period much larger than the Bloch period T.

By varying the initial energy and velocity of the soliton, our study can be extended to qualitatively different adiabatic trajectories of this quantum pendulum. For low kinetic and potential ($\alpha \approx \pi/2$) energies, one recovers the behavior of a classical pendulum, with an elliptical phase portrait trajectory and with $\tilde{P} < \pi$, corresponding to w which is always 0 (see the ellipse in fig. 3.10c). For large initial velocities, open trajectories are expected, corresponding to a wave packet making complete loops in the ring (see the unclosed line in fig. 3.10c).

3.5 Taking a step back

3.5.1 Bloch Oscillations without a lattice in 1D systems

Our experiment is not the first realization of BOs without a lattice. They were first observed by Meinert *et al.* with a single impurity [77]. In this experiment, a spin-polarized gas of ^{133}Cs atoms is confined in a 1D geometry. The spin of a single atom is flipped to create an impurity. When subjected to a force, this impurity exhibits oscillatory motion. However,

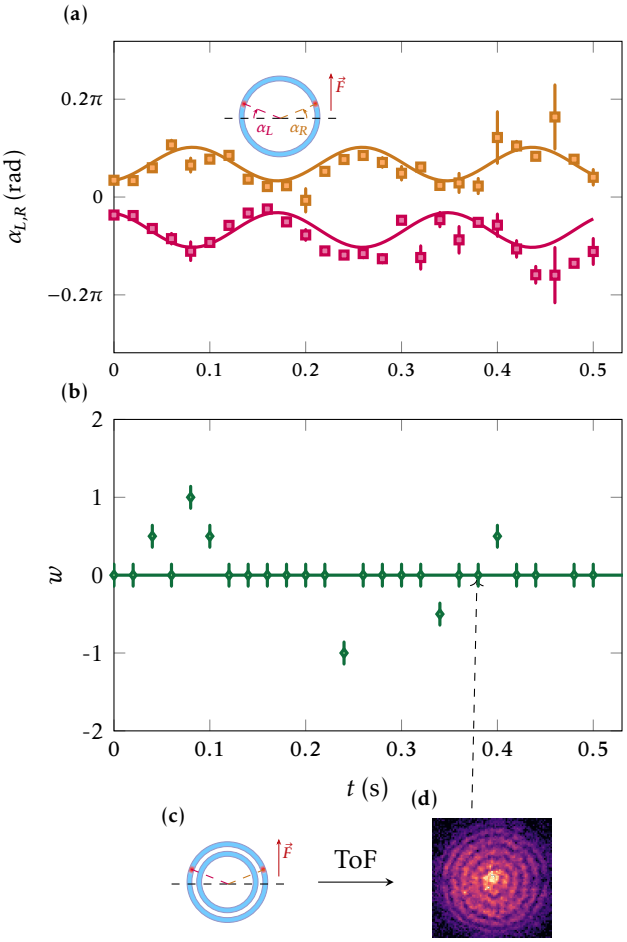

Figure 3.9: Oscillation of two solitons under a constant force in a ring geometry. (a), Same as fig. 3.8a but for two solitons initially at diametrically opposed positions denoted by α_L and α_R. The two solitons have similar initial atom numbers ($\approx$ 1500 atoms). They perform in-phase Bloch oscillations. The solid lines represent a sinusoidal fit to the data with opposite amplitude. (b), Time evolution of the winding number measured with matter-wave interference. The interference pattern is obtained after an expansion from the configuration sketched in (c) with two concentric rings. The data is consistent with no observed winding. (d), Example of measured fringes, corresponding to $w = 0$. The error bars represent the expected statistical errors for 4 repetitions of the experiment when the residual probability to measure a relative winding between the two rings without any soliton in the system has been estimated to be $\approx$ 4%.

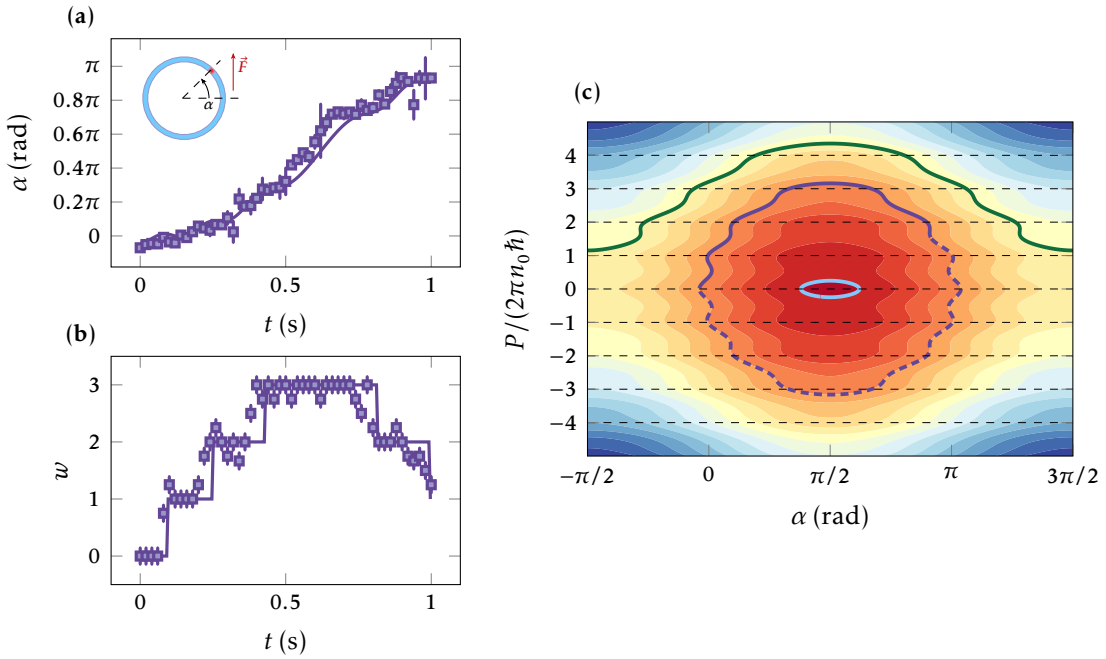

Figure 3.10: Long-time evolution of a soliton in a ring. (a), Angular position of the wave packet moving from one side of the ring to the other for $N_2 = 1600(80)$, $n_0 = 320(10)\,\mu\text{m}^{-1}$ and $f = 6.6(5) \times 10^{-4} M a_G$. (b), Corresponding phase winding of the bath. The winding increases up to +3 and then decreases when $\alpha > \pi/2$. In both plots, the error bars represent the statistical errors obtained from the 4 repetitions of each experiment, and the solid line is the prediction of the particle-like model. (c), Calculated phase portrait (α, P) of the soliton motion starting at $\alpha = P = 0$ (violet line). The evolution is periodic. The first part of the computed motion (solid line part) corresponds to the experimental observation of figures (a), (b). The dashed part of the line shows the expected subsequent evolution. The wave packet reaches the opposite side of the ring ($\alpha = \pi$) with zero momentum and then returns to its initial position with its momentum taking negative values. The two other solid lines correspond to different initial conditions. For $\alpha(t = 0)$ close to $\pi/2$ and with zero initial velocity, we obtain a classical-like trajectory (blue ellipse). For a sufficiently large initial velocity, we obtain open orbits (green solid line). The colored background contour plot is associated with different values of the energy of the system with an arbitrary scale (energy increases from red to blue). The soliton trajectories are associated with iso-energy curves.

these oscillations are strongly damped compared to the ones we observe. The period of the oscillation is $T = n_0 h/f$, where f is the force exerted on the impurity and n_0 is the bath density. This period is consistent with eq. (3.11) when $N_2 = 1$. BOs of such impurities were predicted theoretically [204–207], with the origin of the oscillation being, as in our case, the periodicity of the energy with respect to momentum.

Regarding solitons, BOs have been predicted for other types of solitons, such as spin solitons [159] and dark-bright solitons outside the Manakov limit [208]. In the latter case, the oscillations are not sinusoidal, but in both cases the period matches that of the magnetic soliton. Spinor solitons, such as the ferrodark soliton, also undergo BOs when subjected to a constant force [209]. The occurrence of this behavior across different types of 1D systems stems from a general property of 1D systems: the periodicity of the energy with respect to momentum with a period h/n_0.

3.5.2 Periodicity of the energy for 1D systems

We show in this subsection that the energy of a 1D system with periodic boundary conditions is periodic with respect to the total momentum, in the thermodynamic limit. The following argument is strongly inspired by [76]. We start by considering a 1D system of size L, composed of N particles of mass m, governed by the following Hamiltonian:

$$\hat{H} = \frac{1}{2m}\sum_i \hat{p}_i^2 + \sum_{i<j} V(\hat{x}_i - \hat{x}_j), \tag{3.21}$$

where $(\hat{x}_i, \hat{p}_i)$ are the position and momentum operators of particle i. The Hamiltonian commutes with the total momentum $\hat{P} = \sum_i \hat{p}_i$. An eigenstate of the system can be thus characterized by its total momentum value Q and $N-1$ additional quantum numbers that we label s. We define their energies:

$$\hat{H}\left|\psi_{Q,s}\right\rangle = E_s(Q)\left|\psi_{Q,s}\right\rangle. \tag{3.22}$$

If we do a change of reference frame to the frame of the CoM, this state becomes:

$$\zeta_{Q,s}(x_1 - \bar{x}, \dots, x_n - \bar{x}) = \exp\left(-\mathrm{i}\frac{Q}{\hbar}\bar{x}\right)\psi_{Q,s}(x_1, \dots, x_n), \tag{3.23}$$

where $\bar{x} = \sum_j x_j/N$ is the CoM. The state $\left|\zeta_{Q,s}\right\rangle$ satisfies $\hat{P}\left|\zeta_{Q,s}\right\rangle = 0$ and is also an eigenstate of $\hat{H}$ with energy:

$$\epsilon_s(Q) = E_s(Q) - \frac{Q^2}{2Nm}. \tag{3.24}$$

It is crucial to note that despite having the same quantum numbers ($Q = 0$ and s) the states $\left|\zeta_{Q,s}\right\rangle$ obey different boundary conditions. Indeed, $\left|\psi_{Q,s}\right\rangle$ obeys periodic boundary conditions. So that adding L to any x_i leaves $\psi_{Q,s}$ unchanged, but it is not the case for $\zeta_{Q,s}$ that is multiplied by the factor:

$$f(Q) = \exp\left(-i\frac{QL}{N\hbar}\right), \tag{3.25}$$

so that the state $\left|\zeta_{Q,s}\right\rangle$ obeys twisted boundary conditions. Remarkably $f(Q) = f(Q+Nh/L)$, meaning that $\left|\zeta_{Q,s}\right\rangle$ and $\left|\zeta_{Q+Nh/L,s}\right\rangle$ obey the same boundary conditions on top of being described by the same quantum numbers. This proves that these two states have the same energy, or in other words that $\epsilon(\cdot)$ is a periodic function with period Nh/L. On the other

hand, the energy of the state $|\psi_{Q,s}\rangle$:

$$E_s(Q) = \epsilon_s(Q) + \frac{Q^2}{2Nm}, \tag{3.26}$$

is not periodic for finite size systems. The second term of the rhs of the previous equation is, in the case of a soliton, the energy carried by the backflow. However, in the thermodynamic limit; $L \to \infty$, $N \to \infty$, $L/N \to n_0$; eq. (3.26) reads:

$$E_s(Q) = \epsilon_s(Q), \tag{3.27}$$

proving that the energy of a 1D system is periodic in momentum in the thermodynamic limit with period $n_0 h$.

The previous reasoning dealt with systems having periodic boundary conditions. Nevertheless, we have seen, in the case of the magnetic soliton, that systems with strict boundary conditions can feature an energy periodic in momentum, even at finite size.

3.5.3 Challenges in observing Bloch Oscillations

The presence of a periodic energy structure does not suffice to ensure that a system exhibits Bloch oscillations. We state here some key properties to observe them.

3.5.3.1 Adiabaticity

Dark solitons and dark-bright solitons in the Manakov limit fail to exhibit Bloch oscillations when subjected to a constant force. As their momentum approaches an integer multiple of $2\pi\hbar n_0$, their spatial extent diverges. As a result, near these points, adiabaticity cannot be maintained because the work done by the force over the soliton's extent, $F\sigma$, becomes non-negligible. In fig. 3.11, we present a numerical simulation of a dark-bright soliton in the Manakov limit subjected to a force of comparable magnitude to that applied to the magnetic soliton. The soliton initially moves in the direction opposite to the applied force due to its negative effective mass and then spreads at the turning point without exhibiting oscillatory behavior. A similar behavior is observed for the magnetic soliton when the force is too strong.

For dark-bright solitons outside the Manakov limit, the soliton extent remains finite over a certain range of interaction parameters, as identified by [208]. These parameters correspond to the non-hatched regions in fig. 2.5, where the adiabaticity criterion can be satisfied, thus allowing for the observation of BOs.

3.5.3.2 Quasi-stationarity

Another requirement to observe BOs is that the system, when submitted to a force, explores stationary states. In the case of a magnetic soliton with strict boundary conditions, the stationary soliton state exhibits a flat phase in the bath far from the soliton center. However, the information in the bath propagates at the speed of sound. For a system with $L \gg cT$, signals do not have time to reach the edge of the system over a Bloch period. Therefore, the system evolution cannot be quasi-stationary. In our experiment we only explore the case $L \ll cT$. We show in fig. 3.12 numerical simulations in these two regimes. We see that in the case $L \gg cT$, because of the current in the bath, the evolution of the CoM of the soliton is not periodic anymore. Nonetheless, it still has a distinctive oscillatory motion. This is also observed theoretically in the case of an impurity [195, 207]. On top of that, we see in fig. 3.12b that the current is not space independent anymore: *e.g.* at $t = T$ the

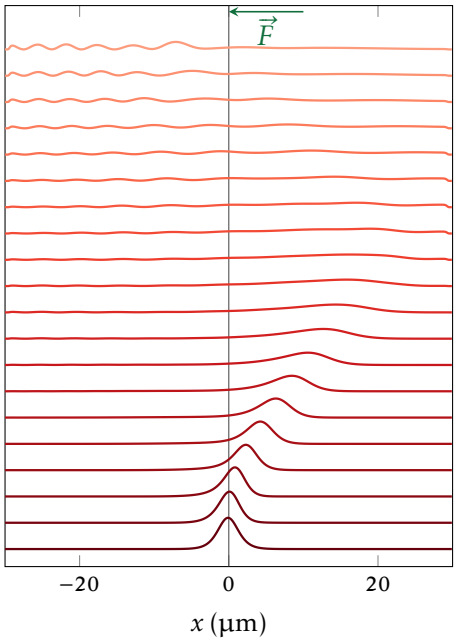

Figure 3.11: Time evolution of a dark-bright soliton in the Manakov limit with strict boundary conditions. Parameters: $L = 60\,\mu\text{m}$, $N_2 = 1300$ atoms, $n_0 = 330\,\mu\text{m}^{-1}$, $b' = 1\,\text{G}\,\text{m}^{-1}$. The evolution is shown from bottom to top, with each curve vertically shifted for clarity. The time difference between consecutive curves is $\approx 10\,\text{ms}$, and the total evolution time corresponds to approximately one Bloch period for the magnetic soliton.

total current in $[-ct, ct]$ is roughly $\hbar n_0 \pi / mct$ whereas outside this region the total current vanishes. This implies that the hypothesis of total constant density is not strictly satisfied anymore.

3.5.4 Finite temperature and beyond mean-field effects

Temperature effects and beyond-mean-field corrections are not included in our treatment of the problem, as we model it using the GPE. To the best of our knowledge, these additional phenomena have not been studied in the context of solitons but only in the case of a single impurity moving in a one-dimensional bath [195, 204, 205, 207, 210, 211].

For an impurity in a 1D bath, the energy exhibits periodicity in momentum, and Bloch oscillations have been observed experimentally by Meinert *et al.* [77]. Notably, the motion of an impurity in the bath leads to the emission of phonons (as is also the case for a soliton). In the case of an infinite system at zero temperature, the coupling between the impurity and the phononic bath leads to BOs superimposed on a constant drift velocity, similarly to the case of the magnetic soliton in an infinite system [195, 205]. At finite temperature, two-phonon interactions induce a temperature-dependent friction force of the form $\kappa(\mathcal{T}, v)v$, where $\mathcal{T}$ is the temperature of the system. In the low-temperature regime, the friction coefficient scales as $\kappa(\mathcal{T}, v) \propto \mathcal{T}^4$ [204, 212]. Notably, this model does not predict damped oscillations, it leads to two distinct regimes. If the applied force is below a threshold value F_{min}, the impurity does not oscillate but simply accelerates until it reaches a terminal velocity. Conversely, if the force exceeds F_{min}, the impurity velocity undergoes oscillations around a value corresponding to the constant drift velocity. In an integrable system, the friction coefficient vanishes. This happens when the impurity mass matches that of a bath atom, and interactions are either in the Manakov limit or infinitely

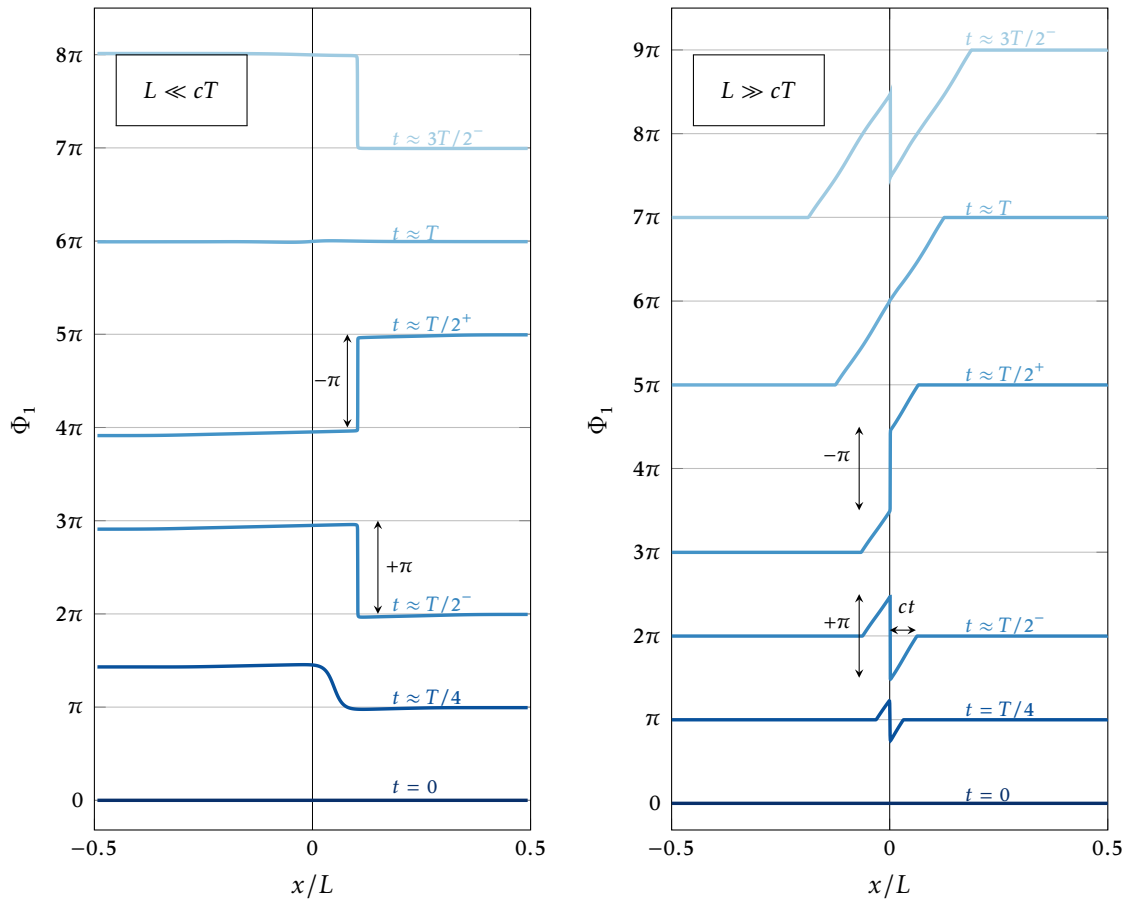

Figure 3.12: Comparison of the evolution of the bath phase for different geometries.(a), Small system configuration, similar to the segment geometry explored in the main text. Boundary effects make the phase profile almost constant on each side of the wave packet. After one oscillation of the wave packet, the phase profile is uniform again leading to periodic BOs. (b), Long system. We observe a linear variation of the phase associated to the backflow over a distance ct. After one period a velocity field is present around the soliton.

strong.

Beyond these two effects, quantum fluctuations at zero temperature induce a dephasing of the oscillations, leading to an algebraic decay of their amplitude of the form $t^{-\alpha}$, where $\alpha \propto F^2$. Whereas, thermal fluctuations cause an exponential decay of the oscillation amplitude, given by $\exp(-\beta t)$, with $\beta \propto F^2 \mathcal{T}$ [195]. A strong damping of oscillations was observed by Meinert *et al.*, where the impurity was subjected to a force comparable to gravity, so over three orders of magnitude larger than in our case. In our setup, no damping of soliton oscillations is observed

Conclusion

In this chapter, we have investigated the dynamics of magnetic solitons subjected to an external force, uncovering oscillatory behaviors fundamentally distinct from those observed with solitons in conventional harmonic traps.

We first established the theoretical framework describing a magnetic soliton submitted to a force, extending the model we derived in the previous chapter. After that, we presented our experimental implementation of such a force using a magnetic gradient, as well as its calibration.

In this chapter, we explored two different geometries: the segment and the ring; revealing different phenomena in each. In the segment geometry, BOs of a magnetic soliton were predicted theoretically, and we observe them experimentally. This phenomenon, occurring in the absence of an external periodic potential, stems from the inherent periodicity of the soliton's energy with respect to its momentum, a feature linked to the one-dimensional nature of the system. We drew an analogy with a Josephson junction, providing an intuitive picture where the soliton acts as a mobile barrier driven by a potential difference created by the force. Our experimental measurements quantitatively confirmed the predicted scaling of the oscillation period, notably revealing its collective nature through the inverse scaling on the number of atoms in the soliton, N_2. Furthermore, we directly measured the associated bath phase dynamics, through matter-wave interferometry revealing characteristic π-phase jumps synchronized with the soliton's turning points at odd numbers of half-periods.

Transitioning to the ring geometry introduced richer dynamics, that, to the best of our knowledge, were unexplored until now, both theoretically and experimentally. These dynamics are the result of the interplay between the oscillatory motion and the backflow current, allowed by periodic boundary conditions. This led to the pumping and depumping of quantized topological superfluid currents in the bath, a phenomenon we directly observed through measurements of the bath's phase winding number. The study of single-soliton long-term dynamics revealed complex trajectories where periodicity is recovered at a larger timescale than the Bloch oscillation period, much like a quantum pendulum. In contrast, experiments with two solitons demonstrated the suppression of net current generation due to cancellation effects between the two solitons, further underscoring the role of the backflow in the dynamics for the single soliton case.

Finally, we placed our findings in the broader context of one-dimensional systems. We justified the generality of the periodicity of energy in momentum in the thermodynamic limit for such systems, explaining why Bloch-like oscillations are a potentially widespread phenomenon in one-dimensional systems. However, several phenomena can prevent their direct observation, notably: thermal dephasing of the oscillations, friction originating from two-phonon processes as well as the impossibility to maintain an adiabatic evolution.

Outlook As an outlook several exciting directions can be explored, we highlight here two of them. The first one is the study of interactions and collisions between magnetic solitons, building upon our initial demonstration of creating soliton pairs in the ring geometry. Investigating phase shifts resulting from collisions, as well as a deeper study of interactions mediated by the bath would be particularly insightful. The second one is to bridge the gap between experiments on Bloch oscillations of a single impurity and our observation with solitons containing ~ 1000 atoms. Exploring the few-body regime where the mean-field description is expected to break down, could reveal the role of quantum effects.

Part II

Superfluidity

CHAPTER 4

Superfluid fraction in broken-symmetry systems at $T = 0$: theoretical framework

Outline of the current chapter

Introduction

This chapter introduces the theory of superfluidity, with a particular emphasis on non-spatially uniform systems at zero temperature. It lays the theoretical foundation for the subsequent chapter, which will focus on our experimental work.

In section 4.1, we define superfluidity and the superfluid fraction tensor. After reviewing the experimental discovery of superfluidity in liquid helium, first observed in the late 1930s by Kapitza and Allen and Misener, we provide an intuitive explanation of the superfluid fraction using the rotating bucket thought experiment. We then define the superfluid fraction tensor, which generalizes this concept to cases where the superfluid response is anisotropic.

In section 4.2, we focus on superfluidity at zero temperature. We explain how the breaking of time-reversal symmetry or translational invariance can reduce the superfluid

fraction of a system to values below unity. We place particular emphasis on systems with broken translational invariance and discuss various bounds on the superfluid fraction that can be calculated using only the static density profile of the system.

Finally, section 4.3 presents quantitative examples of how the superfluid fraction behaves when the density is modulated periodically. We place these results in the context of supersolidity, a topic that has recently attracted significant attention, particularly within the cold-atoms community. The chapter concludes by outlining how the superfluid fraction can be determined via the measurement of the speed of sound, after briefly reviewing sound propagation in superfluids.

4.1 Superfluidity and superfluid fraction tensor

4.1.1 What is superfluidity?

A fluid is said to be superfluid if it can flow without resistance [213]. This remarkable property was first observed in ^{4}He, independently by Kapitza [8] and Allen and Misener [9] in 1938. When cooled below the λ-point at 2.2 K, ^{4}He flows through thin capillaries with viscosity below measurable limits. Superfluids also exhibit other distinctive phenomena including quantized vortices, persistent currents, and two distinct sound modes. As a boson, ^{4}He has a finite BEC fraction below the λ-point, as confirmed by experimental measurements [10, 11]; London first suggested the connection between BECn and superfluidity [6]. However, we stress that the condensate fraction and the superfluid fraction, that will be introduced later, are two distinct quantities. Indeed, superfluidity is not limited to bosonic systems. For instance, the fermionic atom ^{3}He displays superfluid behavior when cooled below 2.7 mK [12]. Superfluidity can also emerge at finite temperature in two-dimensional bosonic systems where BECn is absent [16], highlighting the distinction between these two quantum phenomena.

In cold-atom systems, superfluidity was observed in both BECs [214, 215] and degenerate Fermi gases [216]. These gaseous systems exhibit the same superfluid behaviors as liquid helium despite having densities nearly 10 orders of magnitude lower.

4.1.2 The rotating bucket thought experiment

Despite flowing without resistance through thin capillaries, superfluids do not necessarily have zero viscosity. Keesom and MacWood demonstrated this for liquid helium [217] by measuring viscosity with a rotating metal disk. While they observed a sharp viscosity drop at the λ-point, the value remained finite. To explain superfluid behavior quantitatively, we use the concept of superfluid fraction, introduced by Landau [7].

Leggett illustrates this concept with the following thought experiment [46]. Consider a superfluid confined in a cylinder of radius R and thickness $d \ll R$, with free energy F_0 at rest. When the cylinder rotates at angular speed ω, the rough walls drag any viscous fluid within it.

For a classical fluid at equilibrium, the free energy in the rotating cylinder is:

$$F_{\mathrm{cl}}(\omega) = F_0 + \frac{1}{2} N m R^2 \omega^2, \tag{4.1}$$

where N is the number of particles in the fluid and m is their mass. For a superfluid rotating slowly enough such that no persistent currents are created, *i.e.*:

$$\omega \ll \frac{\hbar}{mR^2}, \tag{4.2}$$

but fast enough such that several particles could acquire one quantum of angular momentum, $\hbar$; *i.e.*:

$$\omega \gg \frac{\hbar}{NmR^2}, \tag{4.3}$$

the free energy is reduced compared to a classical fluid:

$$F(\omega) = F_{\mathrm{cl}}(\omega) - \frac{NmR^2}{2} f_s \omega^2. \tag{4.4}$$

The quantity f_s is called the superfluid fraction and quantifies the reduction in the fluid's rotational inertia. This result can be interpreted by dividing the flow into two components: the normal flow with finite viscosity and the superflow with zero viscosity. We deduce that a fraction f_s of the fluid is not dragged by the cylinder walls; it contributes to the superflow which, in the laboratory reference frame, remains zero.

In the rotating cylinder's reference frame, the free energy of the system is:

$$F_{\mathrm{R}}(\omega) = \frac{NmR^2}{2} f_s \omega^2. \tag{4.5}$$

In this reference frame, the normal flow vanishes, and the superflow accounts for the entire current. This distinction explains many experimental observations of superfluids, such as liquid helium flowing through thin capillaries without friction; the normal flow is suppressed due to its viscosity, leaving only the superflow [98].

Having established the concept of superfluid fraction through the rotating bucket experiment, we will now generalize this approach using linear motion in Cartesian coordinates rather than rotation, which provides an equivalent but mathematically more convenient framework.

4.1.3 Definition of the superfluid fraction tensor

We will now formalize the previous concept and provide a more comprehensive definition of f_s. While the superfluid fraction was scalar in the rotating bucket experiment due to the system's one-dimensional nature, in this section we define the superfluid fraction for three-dimensional systems, where it becomes a tensor. We consider a three-dimensional system with dimensions L_x, L_y, and L_z along the respective coordinate directions, with periodic boundary conditions applied to all directions. The system, containing N particles of mass m, is at finite temperature. Although the formalism presented here applies equally well to one and two dimensions at zero temperature, finite-temperature behavior in lower dimensions introduces additional complexities due to enhanced phase fluctuations [218]. The system is subjected to a moving external potential V_{ext} with velocity $\mathbf{v}$, analogous to the rotating walls of the cylinder in our previous thought experiment.

4.1.3.1 Three points of view

In the absence of external potential we consider the system is governed by the following Hamiltonian:

$$\hat{H}_0 = \sum_i \frac{\hat{\mathbf{p}}_i^2}{2m} + \sum_{i<j} V(\hat{\mathbf{x}}_i - \hat{\mathbf{x}}_j). \tag{4.6}$$

Point of view	Hamiltonian	Boundary conditions
1	$\hat{H}_0 + \sum_i V_{\text{ext}}(\hat{\mathbf{x}}_i - \mathbf{v}t)$	Periodic: $\psi(x_1 + L_x, \dots, z_N) = \psi(x_1, \dots, z_N)$
2	$\hat{H}_0 + \sum_i V_{\text{ext}}(\hat{\mathbf{x}}_i) - \mathbf{v} \cdot \hat{\mathbf{P}}$	Periodic: $\psi(x_1 + L_x, \dots, z_N) = \psi(x_1, \dots, z_N)$
3	$\hat{H}_0 + \sum_i V_{\text{ext}}(\hat{\mathbf{x}}_i)$	Twisted: $\psi(x_1 + L_x, \dots, z_N) = \mathrm{e}^{i\Delta\theta_x}\, \psi(x_1, \dots, z_N)$

Table 4.1: Summary of the three different points of view, adapted from [219]. Concerning the boundary conditions, we write them for coordinate x_1, but they apply to all $3N$ coordinates, with the phase twist changing to $\Delta\theta_y$, $\Delta\theta_z$ for y and z coordinates, respectively.

We present here three points of view to describe the system, [219]. In the first one, we describe our system in the laboratory frame using the following Hamiltonian:

$$\hat{H}_1 = \hat{H}_0 + \sum_i V_{\text{ext}}(\hat{\mathbf{x}}_i - \mathbf{v}t). \tag{4.7}$$

In this point of view, the wave function ψ_1 of the system obeys periodic boundary conditions. We can eliminate the time dependence of $\hat{H}_1$ using the following unitary transformation:

$$\hat{U}_{1\to 2} = \exp\left(\mathrm{i}\frac{\mathbf{v} \cdot \hat{\mathbf{P}} t}{\hbar}\right), \tag{4.8}$$

where $\hat{\mathbf{P}} = \sum_i \hat{\mathbf{p}}_i$ is the total momentum of the system. We obtain the following Hamiltonian:

$$\hat{H}_2 = \hat{H}_0 + \sum_i V_{\text{ext}}(\hat{\mathbf{x}}_i) - \mathbf{v} \cdot \hat{\mathbf{P}}. \tag{4.9}$$

The state $|\psi_2\rangle = \hat{U}_{1\to 2} |\psi_1\rangle$ still obeys periodic boundary conditions. This unitary transformation represents a change of reference frame to one where V_{ext} is at rest.

We can eliminate the term $\mathbf{v} \cdot \hat{\mathbf{P}}$ in eq. (4.9) by applying the following transformation:

$$\hat{U}_{2\to 3} = \exp\left(-\mathrm{i}\frac{m}{\hbar}\mathbf{v} \cdot \sum_j \hat{\mathbf{x}}_j + \mathrm{i}\frac{N m \mathbf{v}^2}{2\hbar} t\right). \tag{4.10}$$

We then obtain the following Hamiltonian:

$$\hat{H}_3 = \hat{H}_0 + \sum_i V_{\text{ext}}(\hat{\mathbf{x}}_i). \tag{4.11}$$

This time, the state $|\psi_3\rangle = \hat{U}_{2\to 3} |\psi_2\rangle$ does not obey periodic boundary conditions, but twisted boundary conditions, meaning that for any particle k:

$$\psi_3(\dots, x_k + L_x, y_k, z_k, \dots) = \exp(\mathrm{i}\Delta\theta_x)\psi_3(\dots, x_k, y_k, z_k, \dots) \tag{4.12a}$$
$$\psi_3(\dots, x_k, y_k + L_y, z_k, \dots) = \exp(\mathrm{i}\Delta\theta_y)\psi_3(\dots, x_k, y_k, z_k, \dots) \tag{4.12b}$$
$$\psi_3(\dots, x_k, y_k, z_k + L_z, \dots) = \exp(\mathrm{i}\Delta\theta_z)\psi_3(\dots, x_k, y_k, z_k, \dots), \tag{4.12c}$$

where $\Delta\theta_\alpha = -m v_\alpha L_\alpha / \hbar$. Table 4.1 summarizes the three points of view.

4.1.3.2 Superfluid fraction from free energy

After establishing the different points of view, we can give a definition of the superfluid fraction tensor. To compute the superfluid fraction of a system obeying periodic boundary conditions and governed by a Hamiltonian $\hat{H}$, we apply a small perturbation: $-\mathbf{v}\cdot\hat{\mathbf{P}}$ and examine ΔF_2, the difference in free energy between the perturbed and unperturbed system. The superfluid fraction tensor is defined as [220]:

$$f_s^{(\alpha,\beta)} = \frac{1}{Nm}\lim_{\substack{v_\alpha\to 0\\ v_\beta\to 0}}\frac{\partial^2\Delta F_2}{\partial v_\alpha \partial v_\beta}, \tag{4.13}$$

This definition relies on point of view 2: the perturbation creates a superflow responsible for the energy increase. This is analogous to looking at the rotating bucket in the reference frame of the moving walls.

Similarly, taking point of view 3, instead of applying a perturbation to the Hamiltonian, we change the boundary conditions from periodic to twisted boundary conditions. The phase twists along directions x, y, z are respectively $\Delta\theta_x$, $\Delta\theta_y$, $\Delta\theta_z$. We define ΔF_3 as the free energy difference between the system with twisted and periodic boundary conditions. The superfluid fraction tensor is defined as [220]:

$$f_s^{(\alpha,\beta)} = \frac{mL_\alpha L_\beta}{N\hbar^2}\lim_{\substack{\Delta\theta_\alpha\to 0\\ \Delta\theta_\beta\to 0}}\frac{\partial^2\Delta F_3}{\partial\Delta\theta_\alpha\partial\Delta\theta_\beta}. \tag{4.14}$$

This equation reveals that f_s quantifies the phase rigidity of a system, *i.e.* the energy cost of changing the phase at the boundary of the system.

In light of section 4.1.3.1, the two definitions of f_s are equivalent.

4.1.3.3 Superfluid fraction from particle current

We can also define the superfluid fraction using the particle current instead of the energy. We do this using point of view 2. Noticing that $\hat{U}_{1\to 2}\hat{\mathbf{P}}\hat{U}_{1\to 2}^\dagger = \hat{\mathbf{P}}$, we deduce that the particle current in the laboratory frame, and hence the normal flow, is proportional to $\langle\hat{\mathbf{P}}\rangle_2$, where $\langle\cdot\rangle_2$ denotes the thermal average in point of view 2. For sufficiently small $\mathbf{v}$:

$$\langle\hat{P}_\alpha\rangle_2 \sim Nm\sum_\beta\left(\delta_{\alpha,\beta} - f_s^{\alpha,\beta}\right)v_\beta \tag{4.15}$$

We can therefore define f_s as [220]:

$$f_s^{(\alpha,\beta)} = \delta_{\alpha,\beta} - \lim_{v_\beta\to 0}\frac{\langle P_\alpha\rangle_2}{Nmv_\beta}. \tag{4.16}$$

This is a convenient definition of f_s as it depends, at lowest order, linearly on $\mathbf{v}$ instead of quadratically. As stated previously, these results are also valid in the case of a two-dimensional system at zero temperature, which will be the focus of the remaining part of this chapter.

4.2 Superfluid fraction at zero temperature

4.2.1 The role of symmetries on the superfluid fraction

4.2.1.1 Fully superfluid systems at zero temperature

The superfluid fraction is a temperature-dependent quantity. Finite temperature typically reduces the superfluid fraction compared to the zero temperature case. What, then, can be said about the superfluid fraction of a system at zero temperature? Under certain conditions, at zero temperature, the superfluid fraction of the system equals one. According to Leggett [221] a sufficient set of conditions for a system of identical bosonic particles with finite interactions to have a unit superfluid fraction at zero temperature are:

- The Hamiltonian and the ground state have translational invariance, *i.e.* for all vectors $\mathbf{r} \in \mathbb{R}^3$, the wave function of the ground state satisfies $\Psi_0(\mathbf{r}_1 + \mathbf{r}, \dots, \mathbf{r}_k + \mathbf{r}, \dots, \mathbf{r}_N + \mathbf{r}) = \Psi_0(\mathbf{r}_1, \dots, \mathbf{r}_k, \dots, \mathbf{r}_N)$.

- The Hamiltonian and the ground state have time-reversal symmetry, *i.e.* the wave function of the ground state satisfies $\Psi_0(\mathbf{r}_1, \dots, \mathbf{r}_N) = \Psi_0^*(\mathbf{r}_1, \dots, \mathbf{r}_N)$, so the wave function is real-valued.

For fermionic systems, an additional condition applies: given a direction $\mathbf{e}_j \in \{\mathbf{e}_x, \mathbf{e}_y, \mathbf{e}_z\}$, it must be possible to find a path for every particle k:

$$(\mathbf{r}_1, \dots, \mathbf{r}_k, \dots, \mathbf{r}_N) \longrightarrow (\mathbf{r}_1, \dots, \mathbf{r}_k + L_j \mathbf{e}_j, \dots, \mathbf{r}_N), \tag{4.17}$$

along which the wave function of the ground state remains bounded from below by a constant independent of N and L_j. This condition is automatically satisfied for bosonic systems since, if the ground state has time-reversal symmetry, the wave function of the ground state is positive definite (see [222] or corollary 3.1 of [223]). We point out that the existence of such a one-particle path is not a necessary condition, as the existence of two-particle paths is also sufficient.

4.2.1.2 Some examples of systems with sub-unity superfluid fraction at zero temperature

If at least one of the previous conditions is not satisfied, the system does not necessarily have a superfluid fraction of 1 even at zero temperature. Consider the well-known superfluid to Mott insulator transition [32, 224, 225], where the superfluid fraction can vanish completely at zero temperature. In this case, translational invariance is broken by an external periodic potential. Even without the Mott-Insulator transition, the presence of periodic [226–229] or disordered [230–232] external potentials reduces the superfluid fraction. In supersolids, that will be discussed in section 4.3.1, translational invariance is broken spontaneously, also resulting in a sub-unity superfluid fraction at zero temperature [46, 220, 233–238], as measured in ref. [239]. A similar situation emerges in astrophysics in the context of neutron stars where the periodic lattice of nuclei influences the superfluid density in the inner crust [240, 241]. Spin-orbit coupling breaks time-reversal symmetry, and a reduction in the superfluid fraction at zero temperature in a spin-orbit coupled BEC has been predicted [242].

4.2.2 Bounds on the superfluid fraction at zero temperature

4.2.2.1 Deriving an upper bound

In his seminal work, Leggett [46] provided an upper bound for the superfluid fraction of a system at zero temperature, relying only on the system's density profile. His remarkable result proves that a system with a non-uniform density profile has a superfluid fraction strictly below one. To better understand this phenomenon, we summarize Leggett's approach below, focusing on a two-dimensional system to match the dimensionality of the experiments discussed in the next chapter.

We consider a many-body system with periodic boundary conditions. We assume its Hamiltonian $\hat{H}$ is invariant under time reversal and that its ground state $|\Psi_0\rangle$ does not break this symmetry. The wave function Ψ_0 can thus be chosen as real. To estimate the superfluid fraction, we use twisted boundary conditions with a twist $\Delta\theta_\alpha \ll 2\pi$ along direction α. To simplify the notation, we define $\mathbf{R} = (\mathbf{r}_1, \dots, \mathbf{r}_N)$ as the $2N$-dimensional vector of the particles' coordinates. To find an upper bound of the ground state energy, we rely on a variational approach. With twisted boundary conditions, at lowest order in $\Delta\theta_\alpha$ the ground state wave function reads:

$$\Psi(\mathbf{R}) = \exp\left(\mathrm{i}\varphi\left(\mathbf{R}\right)\right)\Psi_0(\mathbf{R}), \tag{4.18}$$

where $\varphi(\mathbf{R})$ is a real function (see paragraph below). Depending on the particle statistics, Ψ_0 and Ψ are either symmetric or antisymmetric with respect to particle exchange, which implies that φ is a symmetric function. The function φ obeys the following boundary conditions: for all indices k, $\varphi(\cdots, \mathbf{r_k} + L_x\mathbf{e}_x, \cdots) = \varphi(\cdots, \mathbf{r_k}, \cdots) + \Delta\theta_x$, $\varphi(\cdots, \mathbf{r_k} + L_y\mathbf{e}_y, \cdots) = \varphi(\cdots, \mathbf{r_k}, \cdots) + \Delta\theta_y$. We define E_0 as the energy of the state $|\Psi_0\rangle$; the energy of the state $|\Psi\rangle$ is:

$$E = E_0 + \frac{\hbar^2}{2m}\sum_{j=1}^{N}\int(\boldsymbol{\nabla}_j\varphi(\mathbf{R}))^2\Psi_0^2(\mathbf{R})\mathrm{d}\mathbf{R}. \tag{4.19}$$

To derive this expression, we used the fact that Ψ_0 is real-valued, so the current:

$$\frac{\hbar}{m}\mathcal{I}(\Psi_0^*\boldsymbol{\nabla}_j\Psi_0), \tag{4.20}$$

vanishes everywhere. The next step is to find φ that minimizes E to obtain the tightest possible bound using eq. (4.14). To do so, we use a variational approach; we minimize E by assuming the function φ obeys:

$$\varphi(\mathbf{R}) = \sum_{j=1}^{N}\phi(\mathbf{r}_j), \tag{4.21}$$

where $\phi(\mathbf{r} + L_x\mathbf{e}_x) = \phi(\mathbf{r}) + \Delta\theta_x$ and $\phi(\mathbf{r} + L_y\mathbf{e}_y) = \phi(\mathbf{r}) + \Delta\theta_y$. With this assumption, eq. (4.19) becomes:

$$E_{\text{trial}} = E_0 + \frac{\hbar^2}{2m}\int\rho(\mathbf{r})\left(\boldsymbol{\nabla}\phi(\mathbf{r})\right)^2\mathrm{d}\mathbf{r}\,, \tag{4.22}$$

where $\rho(\mathbf{r}) = N\int\Psi_0^2(\mathbf{r}, \mathbf{r}_2, \dots, \mathbf{r}_N)\,\mathrm{d}\mathbf{r}_2 \dots \mathrm{d}\mathbf{r}_N$ is the particle density. Because E_{trial} is the energy obtained using the variational ansatz of eq. (4.21), it is an upper bound for the energy of the ground state with twisted boundary conditions. The function ϕ minimizing the integral on the rhs of eq. (4.22) is found by solving its associated Euler-Lagrange

equation:

$$\boldsymbol{\nabla} \cdot (\rho \boldsymbol{\nabla} \phi) = 0. \tag{4.23}$$

We will derive two upper bounds for the superfluid fraction. The first one, originally derived by Leggett, is simpler but less tight than the second one.

Proof of eq. (4.18) To see that the wave function with twisted boundary conditions is of the form given by eq. (4.18) at lowest order in $\Delta\theta_\alpha$, we switch to point of view 2. We examine the ground state $|\Psi_1\rangle$ of:

$$\hat{H}_2 = \hat{H}_1 - \mathbf{v} \cdot \hat{\mathbf{P}}, \tag{4.24}$$

where the second term of the rhs is treated as a perturbation. Thanks to time-reversal symmetry, all the eigenstates of $\hat{H}_1$, $|\Psi_\lambda\rangle$, can be taken as real-valued functions. The matrix elements $\langle \Psi_\lambda | \, \mathbf{v} \cdot \hat{\mathbf{P}} \, | \Psi_0 \rangle$ are thus all imaginary numbers. According to perturbation theory, at first order in v we can write the perturbed ground state wave function as:

$$\Psi_1(\mathbf{R}) = \Psi_0(\mathbf{R}) + \mathrm{i}\delta\Psi(\mathbf{R}), \tag{4.25}$$

with $\delta\Psi$ a real-valued function. Again at first order in v:

$$\Psi_1(\mathbf{R}) = \Psi_0(\mathbf{R}) + \mathrm{i}\delta\Psi(\mathbf{R}) \approx \Psi_0(\mathbf{R}) \exp\left(\mathrm{i}\varphi_1(\mathbf{R})\right). \tag{4.26}$$

Equation (4.18) is then obtained by returning to point of view 3, which is accomplished by applying the unitary transformation given in eq. (4.10) to Ψ_1.

4.2.2.2 Leggett's original upper bound

Leggett provided an upper bound for the diagonal components of the superfluid fraction tensor. The calculations are performed, without loss of generality, for $f_s^{(x,x)}$, so we set $\Delta\theta_y = 0$. To derive the Leggett upper bound, we add a condition to our variational ansatz: we assume that ϕ is a function of x only. In this case, eq. (4.23) becomes:

$$\frac{\partial}{\partial x}\left(\rho(x,y)\frac{\mathrm{d}\phi}{\mathrm{d}x}\right) = 0. \tag{4.27}$$

By integrating the last equation we obtain:

$$\frac{\mathrm{d}\phi}{\mathrm{d}x} = \frac{A}{\int \rho(x,y)\,\mathrm{d}y}, \tag{4.28}$$

where A is an integration constant. It is important to note that this solution generally does not satisfy eq. (4.23). Therefore, the solution obtained does not necessarily minimize E_{trial}. However, when the density is separable, *i.e.* $\rho(x,y) = f(x)g(y)$ with positive functions f and g, the solution given in eq. (4.28) does satisfy eq. (4.23). To simplify notation, we use the spatial average over direction α: $\langle\cdot\rangle_\alpha = \int \mathrm{d}\alpha \cdot / L_\alpha$. By integrating eq. (4.28) between 0 and L_x, and using the boundary conditions of ϕ, $\phi(L_x) - \phi(0) = \Delta\theta_x$, we obtain:

$$\Delta\theta_x = \frac{A}{L_y} L_x \left\langle \frac{1}{\langle\rho\rangle_y} \right\rangle_x \tag{4.29}$$

Solving the previous equation for A and substituting back into eq. (4.28) yields:

$$\frac{\partial \phi}{\partial x} = \frac{\Delta\theta_x}{\left\langle \frac{1}{\langle\rho\rangle_y} \right\rangle_x \langle\rho\rangle_y L_x}. \tag{4.30}$$

We compute the associated energy using eq. (4.22):

$$E_{\text{trial}} = E_0 + \Delta\theta_x^2 \frac{\hbar^2}{2m} \left(\left\langle \frac{1}{\langle\rho\rangle_y} \right\rangle_x \right)^{-1} \tag{4.31}$$

Since we used a variational approach, the energy of the ground state with twisted boundary conditions is smaller than E_{trial}. Leggett's upper bound on the superfluid fraction follows from eq. (4.14):

$$f_s^{(x,x)} \leq f_+^{(x,x)}, \tag{4.32}$$

with

$$f_+^{(x,x)} = \frac{1}{\langle\rho\rangle} \left(\left\langle \frac{1}{\langle\rho\rangle_y} \right\rangle_x \right)^{-1}, \tag{4.33}$$

where $\langle\rho\rangle = N/L_x L_y$ is the mean density. Similarly:

$$f_s^{(y,y)} \leq f_+^{(y,y)} = \frac{1}{\langle\rho\rangle} \left(\left\langle \frac{1}{\langle\rho\rangle_x} \right\rangle_y \right)^{-1}. \tag{4.34}$$

4.2.2.3 A more refined upper bound

A few years later, Saslow published a more refined upper bound [243] (see also [244]) that, while more complicated to compute, provides tighter constraints. It relies on solving eq. (4.23) to find $\boldsymbol{\nabla}\phi$. We define

$$\tilde{\phi} = \phi - \frac{\Delta\theta_x}{L_x} x - \frac{\Delta\theta_y}{L_y} y \tag{4.35}$$

$$\mathbf{u} = \frac{\Delta\theta_x}{L_x} \mathbf{e}_x + \frac{\Delta\theta_y}{L_y} \mathbf{e}_y, \tag{4.36}$$

so that $\tilde{\phi}$ obeys periodic boundary conditions. Substituting these definitions into eq. (4.23) gives:

$$\boldsymbol{\nabla} \cdot \left(\rho \boldsymbol{\nabla} \tilde{\phi} \right) = -\boldsymbol{\nabla} \cdot (\rho \mathbf{u}). \tag{4.37}$$

To solve this equation, we proceed as in refs. [220, 245–248] by introducing an auxiliary field $\mathbf{K}(x,y) = (K^{(x)}(x,y), K^{(y)}(x,y))$, defined by $\tilde{\phi}(x,y) = \mathbf{K}(x,y) \cdot \mathbf{u}$. Substituting this in eq. (4.37) yields:

$$\boldsymbol{\nabla} \cdot [\rho \boldsymbol{\nabla} (\mathbf{K} \cdot \mathbf{u})] = -\boldsymbol{\nabla} \cdot (\rho \mathbf{u}). \tag{4.38}$$

With this, we can derive the superfluid fraction by computing the trial energy:

$$E_{\text{trial}} = E_0 + \frac{\hbar^2 N}{2m}\left(\frac{\Delta\theta_x^2}{L_x^2} + \frac{\Delta\theta_y^2}{L_y^2}\right) + \frac{\hbar^2}{m}\int \rho\mathbf{u}\cdot\boldsymbol{\nabla}(\mathbf{K}\cdot\mathbf{u})\,\mathrm{d}\mathbf{r} + \frac{\hbar^2}{2m}\int \rho\left[\boldsymbol{\nabla}(\mathbf{K}\cdot\mathbf{u})\right]^2\mathrm{d}\mathbf{r}\,. \quad (4.39)$$

By integrating by parts and using eq. (4.38) the last integral can be written:

$$\int \rho\left[\boldsymbol{\nabla}(\mathbf{K}\cdot\mathbf{u})\right]^2\mathrm{d}\mathbf{r} = \int (\mathbf{K}\cdot\mathbf{u})\boldsymbol{\nabla}(\rho\mathbf{u})\,\mathrm{d}\mathbf{r} = -\int \rho\mathbf{u}\cdot\boldsymbol{\nabla}(\mathbf{K}\cdot\mathbf{u})\,\mathrm{d}\mathbf{r}\,, \quad (4.40)$$

where the boundary terms of integration by parts cancel as all functions obey periodic boundary conditions. Substituting the above equation into eq. (4.39), we find:

$$E_{\text{trial}} = E_0 + \frac{\hbar^2 N}{2m}\left(\frac{\Delta\theta_x^2}{L_x^2} + \frac{\Delta\theta_y^2}{L_y^2}\right) + \frac{\hbar^2}{2m}\int \rho\mathbf{u}\cdot\boldsymbol{\nabla}(\mathbf{K}\cdot\mathbf{u})\,\mathrm{d}\mathbf{r}\,. \quad (4.41)$$

Using eqs. (4.14) and (4.36), we derive Saslow's more precise upper bound for the superfluid fraction tensor (with an opposite sign convention for $\mathbf{K}$ compared to [220]):

$$S_+^{(i,j)} = \delta^{(i,j)} + \frac{1}{N}\int \rho\partial_i K^{(j)}\,\mathrm{d}\mathbf{r}\,, \quad (4.42)$$

where δ is the Kronecker delta and $\mathbf{K}(x,y)$ is found by solving eq. (4.38)

4.2.2.4 Summary and saturation of the bounds

We have derived two upper bounds on the superfluid fraction tensor using variational ansätze. If the ground state of the system satisfies the variational assumptions made to derive a bound, the bound is saturated. This means its value equals the superfluid fraction. The conditions under which each bound is saturated are the following.

Saslow's upper bound, given by eq. (4.42), is saturated if:

- The Hamiltonian of the system and the ground state have time-reversal symmetry.
- The function $\varphi(\mathbf{R})$ has the form given by eq. (4.21).

For a system governed by the GPE and with time-reversal symmetry, the first condition is naturally satisfied, and the second one follows from the Hartree ansatz. Thus, for such a system:

$$f_s^{(i,j)} = S_+^{(i,j)}. \quad (4.43)$$

This result is remarkable: the superfluid fraction, a quantity describing the dynamic behavior of a system, can be characterized solely by the density profile, which is a purely static quantity.

Leggett's upper bound is saturated if the two conditions for the saturation of Saslow's bound are satisfied along with:

- The density is separable, *i.e.* $\rho(x,y) = f(x)g(y)$, where f and g are functions that are positive everywhere.

For a system governed by the GPE and with time-reversal symmetry, if the density is separable, we obtain an even simpler expression for the superfluid fraction:

$$f_s^{(i,i)} = f_+^{(i,i)} = \frac{1}{\langle\rho\rangle}\left(\left\langle\frac{1}{\langle\rho\rangle_j}\right\rangle_i\right)^{-1}, \quad (4.44)$$

In this case, the off-diagonal components of the superfluid fraction vanish.

4.2.2.5 Leggett's lower bound

Leggett provided a lower bound on the superfluid fraction in a subsequent article [221]. As with the upper bound, we assume that the Hamiltonian and the ground state obey time-reversal symmetry, so that the wave function Ψ_0 is real-valued. We will also assume in the rest of this subsection that the function Ψ_0 does not vanish. At lowest order when twisting the boundary conditions, the wave function takes the form given by eq. (4.18):

$$\Psi(\mathbf{R}) = \exp\left(\mathrm{i}\varphi\left(\mathbf{R}\right)\right)\Psi_0(\mathbf{R}), \tag{4.45}$$

The energy of the ground state is given by eq. (4.19):

$$E = E_0 + \frac{\hbar^2}{2m}\sum_{j=1}^{N}\int \left(\boldsymbol{\nabla}_j\varphi\left(\mathbf{R}\right)\right)^2\Psi_0^2(\mathbf{R})\mathrm{d}\mathbf{R}. \tag{4.46}$$

To find a lower bound on the superfluid fraction, we minimize this energy. The second term of the rhs of the previous equation is a sum of N positive terms, so it is bounded from below by N times the minimum term. Since the functions φ and Ψ_0^2 are symmetric with respect to particle exchange (as noted earlier), we can relabel the particles such that the minimum term of the sum corresponds to the first particle: $\int(\boldsymbol{\nabla}_1\varphi(\mathbf{R}))^2\Psi_0^2(\mathbf{R})\mathrm{d}\mathbf{R}$. The lower bound on the energy E_- thus obtained is:

$$E_- = E_0 + \frac{\hbar^2 N}{2m}\int(\boldsymbol{\nabla}_1\varphi)^2\Psi_0^2(\mathbf{R})\,\mathrm{d}\mathbf{R}\,. \tag{4.47}$$

To simplify the minimization, we split the energy difference into two parts:

$$E_- - E_0 = \frac{\hbar^2 N}{2m}\int\left(\frac{\partial\varphi}{\partial x_1}\right)^2\Psi_0^2(\mathbf{R})\,\mathrm{d}\mathbf{R} + \frac{\hbar^2 N}{2m}\int\left(\frac{\partial\varphi}{\partial y_1}\right)^2\Psi_0^2(\mathbf{R})\,\mathrm{d}\mathbf{R}\,, \tag{4.48}$$

and define

$$E_x = \frac{\hbar^2 N}{2m}\int\left(\frac{\partial\varphi}{\partial x_1}\right)^2\Psi_0^2(\mathbf{R})\,\mathrm{d}\mathbf{R} \tag{4.49}$$

$$E_y = \frac{\hbar^2 N}{2m}\int\left(\frac{\partial\varphi}{\partial y_1}\right)^2\Psi_0^2(\mathbf{R})\,\mathrm{d}\mathbf{R}\,, \tag{4.50}$$

where E_x and E_y are both positive. To obtain a lower bound on $f_s^{(x,x)}$, we minimize E_x and use the fact that $E_- - E_0 \geq E_x$. The Euler-Lagrange equation for the phase φ minimizing E_x is:

$$\frac{\partial}{\partial x_1}\left(\frac{\partial\varphi}{\partial x_1}\Psi_0^2\right) = 0. \tag{4.51}$$

By integrating the last equation with respect to x_1, we obtain:

$$\frac{\partial\varphi}{\partial x_1}\Psi_0^2 = A(y_1, \mathbf{r}_2, \ldots, \mathbf{r}_N), \tag{4.52}$$

where A is an integration constant that depends on all coordinates except x_1. Integrating once more with respect to x_1 from 0 to L_x, and applying the boundary conditions for φ:

$$\varphi(L_x, y_1, \mathbf{r}_2, \dots, \mathbf{r}_N) = \Delta\theta_x + \varphi(0, y_1, \mathbf{r}_2, \dots, \mathbf{r}_N), \tag{4.53}$$

we obtain the following constraint on the integration constant A:

$$\Delta\theta_x = A(y_1, \mathbf{r}_2, \dots, \mathbf{r}_N) \int_0^{L_x} \frac{\mathrm{d}x_1}{\Psi_0^2(\mathbf{R})}. \tag{4.54}$$

Solving for A and substituting back into eq. (4.52) yields:

$$\frac{\partial\varphi}{\partial x_1} = \frac{\Delta\theta_x}{\Psi_0^2} \left(\int_0^{L_x} \frac{\mathrm{d}x_1}{\Psi_0^2} \right)^{-1}. \tag{4.55}$$

Substituting this into the definition of E_x (eq. (4.49)), we obtain the following lower bound for the energy:

$$E_- - E_0 \geq \Delta\theta_x^2 \frac{\hbar^2 N}{2m} \int \mathrm{d}y_1 \, \mathrm{d}\mathbf{r}_2 \dots \mathrm{d}\mathbf{r}_\mathbf{N} \left(\int_0^{L_x} \frac{\mathrm{d}x_1}{\Psi_0^2(\mathbf{R})} \right)^{-1}. \tag{4.56}$$

This gives us a lower bound on the diagonal component of the superfluid fraction tensor:

$$f_s^{(x,x)} \geq f_-^{(x,x)} = L_x L_y \int \mathrm{d}y_1 \, \mathrm{d}\mathbf{r}_2 \dots \mathrm{d}\mathbf{r}_N \left(\int_0^{L_x} \frac{\mathrm{d}x_1}{\Psi_0^2(\mathbf{R})} \right)^{-1} \tag{4.57}$$

For a wave function obeying the Hartree ansatz, where each particle is described by the same single-particle wave function f_0:

$$\Psi_0(\mathbf{r}_1, \dots, \mathbf{r}_N) = \prod_{i=1}^{N} f_0(\mathbf{r}_i), \tag{4.58}$$

$$\text{with} \quad \int f_0^2(\mathbf{r}) \, \mathrm{d}\mathbf{r} = 1, \ \rho(\mathbf{r}) = N f_0^2(\mathbf{r}), \tag{4.59}$$

e.g. in the case of the GPE, the many-body integral simplifies, yielding:

$$f_-^{(x,x)} = \frac{1}{\langle\rho\rangle} \left\langle \left\langle \frac{1}{\rho} \right\rangle_x^{-1} \right\rangle_y \tag{4.60}$$

Similarly, the bound in the y direction is:

$$f_-^{(y,y)} = \frac{1}{\langle\rho\rangle} \left\langle \left\langle \frac{1}{\rho} \right\rangle_y^{-1} \right\rangle_x \tag{4.61}$$

4.3 Measurement of the superfluid fraction in spatially modulated systems

We saw in the previous section that breaking translational invariance produces a reduction of the superfluid fraction at zero temperature. The study of superfluidity in spatially

modulated systems is particularly relevant for supersolids, a rapidly growing research topic since their first experimental realization in recent years.

4.3.1 Supersolids

The existence of supersolidity, a counter-intuitive state of matter combining the properties of a solid and a superfluid, was debated at length. It was first suggested that a solid ^{4}He crystal with vacancies could feature such properties [249]; however, supersolidity was never observed in helium. A supersolid is defined as a system with a finite superfluid fraction and with spontaneously broken translational invariance, where these two properties are associated with two distinct order parameters [45]. Supersolids were first observed in ultracold atoms through various approaches: in BECs with cavity-mediated interactions [50, 51], in spin-orbit coupled BECs [52, 53], in periodically driven BECs [54], and in BECs with strong magnetic dipole-dipole interactions [55–57], where they have been studied most extensively. Dipolar supersolids were first realized along one dimension before being realized along two dimensions [250]. More recently, first signatures of supersolidity were observed in another platform: an exciton-polariton BEC [251].

Two-dimensional dipolar supersolids can crystallize in different phases, notably: the stripe phase, where only one direction is modulated; the triangular phase; and the honeycomb phase [236]. With our current experimental setup, we cannot produce a supersolid; however, we can create density-modulated superfluids by applying an external periodic potential to a BEC. In the next section, we quantitatively analyze how superfluidity is affected by different lattice geometries.

4.3.2 Superfluid fraction for different profiles

4.3.2.1 Profiles studied and simulation parameters

In this subsection, we provide illustrative examples of the behavior of the superfluid fraction in two-dimensional systems with three different density modulation profiles: a one-dimensional sinusoidal lattice, a square lattice, and a triangular lattice. We study these three cases by numerically solving the GPE:

$$i\hbar\frac{\partial\psi}{\partial t} = -\frac{\hbar^2}{2m}\nabla^2\psi + g\left|\psi\right|^2\psi + V(x,y)\psi, \tag{4.62}$$

where $V(x,y)$ is the lattice potential. For all cases, we define p as the period of the lattice and V_0 as the peak-to-peak amplitude of the potential. All simulations presented below were conducted with the following parameters:

- a mean density, $\langle\rho\rangle = 50\,\mu\text{m}^{-2}$.
- an interaction parameter, $g = 0.158 \times \hbar^2/m$.
- a lattice period, $p = 6\,\mu\text{m}$.

The superfluid fraction and bounds are calculated by simulating the system over a unit cell. To compute the superfluid fraction, we examine the energy increase induced by a phase twist and apply eq. (4.14). To calculate the Leggett and Saslow bounds, we use the ground state density profile with periodic boundary conditions over a unit cell. Because we describe our system using the GPE, the Saslow upper bound is saturated.

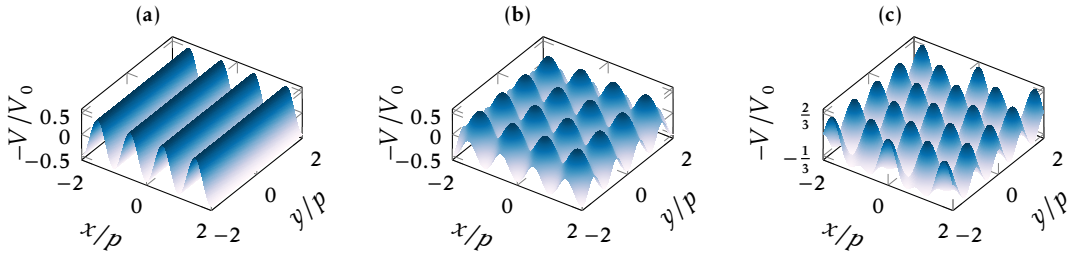

Figure 4.1: Three-dimensional plots of the potentials studied. We plot the opposite of the potential, so the maxima of the density correspond to the maxima of the plot. (a), one-dimensional sinusoidal lattice; (b), square lattice; and (c), triangular lattice.

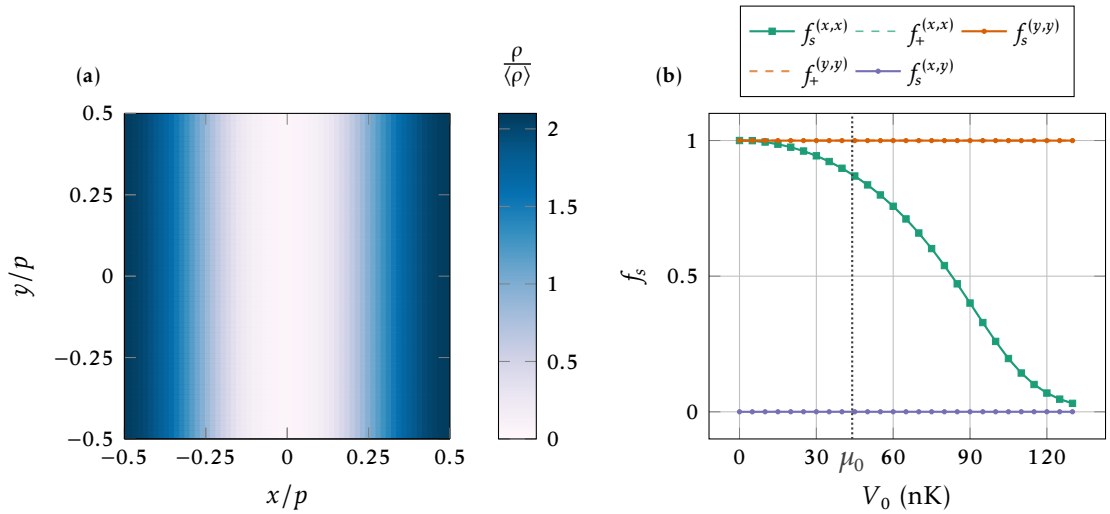

Figure 4.2: Numerical simulation results for a one-dimensional sinusoidal lattice. (a), Density profile for $V_0 = 100\,\text{nK}$ over a square unit cell. (b) The superfluid fraction tensor components are plotted in solid lines. The Leggett upper bounds in the x and y directions are saturated, causing the curves to overlap with the superfluid fraction. The vertical gray dotted line indicates the chemical potential for $V_0 = 0$.

4.3.2.2 One-dimensional lattice

The one-dimensional sinusoidal potential is given by:

$$V(x,y) = \frac{V_0}{2}\cos\left(\frac{2\pi}{p}x\right). \tag{4.63}$$

The superfluid fraction is diagonal in the x, y basis but not isotropic. In this case, the density is separable and the Leggett upper bound is saturated, as shown in fig. 4.2. Therefore, the superfluid fraction can be estimated from the static density profile using eqs. (4.33) and (4.34). The superfluid fraction along y remains unaffected by the lattice and equals 1.

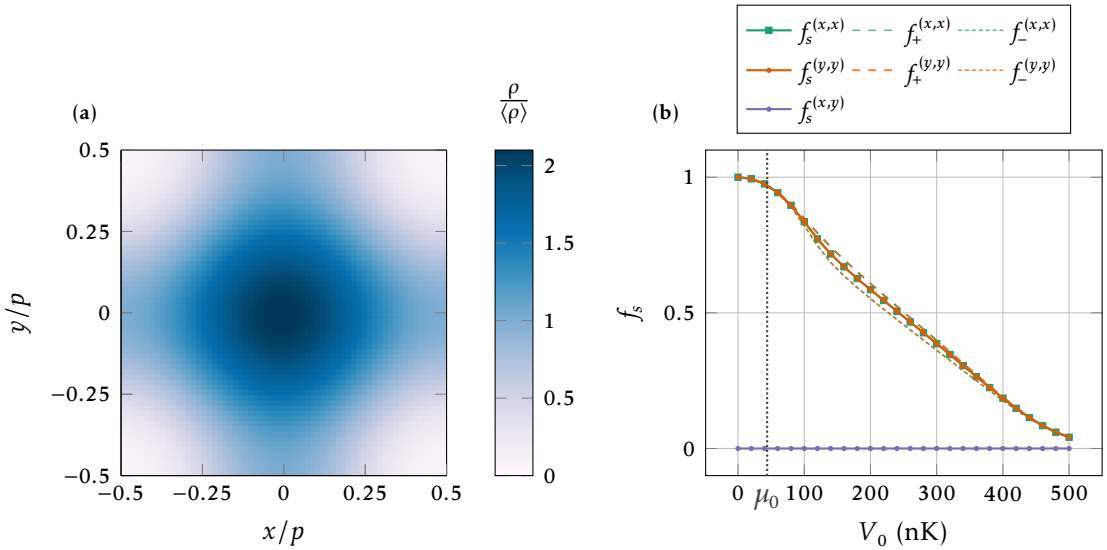

Figure 4.3: Numerical simulation results for a square lattice. (a), Density profile for $V_0 = 100\,\mathrm{nK}$ over a square unit cell. (b) The superfluid fraction tensor components are plotted in solid lines. The curves for the Leggett upper bound in the x and y directions overlap, as do the curves for the Leggett lower bound. The superfluid fraction diagonal components are equal and the off-diagonal elements vanish, making the tensor proportional to the identity matrix. The vertical gray dotted line indicates the chemical potential for $V_0 = 0$.

4.3.2.3 Square lattice

The square lattice potential is given by:

$$V(x,y) = -\frac{V_0}{4}\left[\cos\left(\frac{2\pi}{p}x\right) + \cos\left(\frac{2\pi}{p}y\right)\right]. \tag{4.64}$$

The density is not separable in this case (it would be without the $g|\psi|^2\psi$ term in eq. (4.62)), so the Leggett bounds are not saturated. However, they provide a good estimate of the superfluid fraction, as shown in fig. 4.3. The superfluid fraction is isotropic, making the superfluid fraction tensor proportional to the identity matrix.

4.3.2.4 Triangular lattice

The triangular lattice potential is given by:

$$V(x,y) = -\frac{2V_0}{9}\left[\cos\left(\frac{4\pi}{\sqrt{3}p}x\right) + \cos\left(\frac{2\pi}{\sqrt{3}p}x + \frac{2\pi}{p}y\right) + \cos\left(-\frac{2\pi}{\sqrt{3}p}x + \frac{2\pi}{p}y\right)\right], \tag{4.65}$$

or equivalently:

$$V(\mathbf{r}) = -\frac{2V_0}{9}\sum_{j=1}^{3}\cos(\mathbf{k}_j\cdot\mathbf{r}) \tag{4.66a}$$

$$\text{with}\quad \mathbf{k_j} = \frac{4\pi}{\sqrt{3}p}\begin{pmatrix}\cos\left[(j-1)\pi/3\right]\\ \sin\left[(j-1)\pi/3\right]\end{pmatrix}. \tag{4.66b}$$

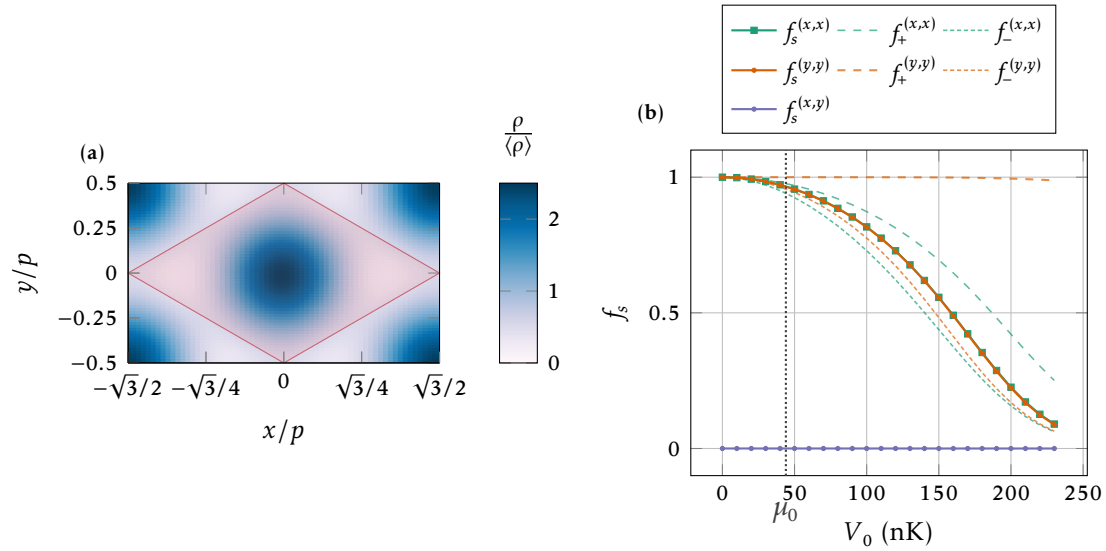

Figure 4.4: Numerical simulation results for a triangular lattice. (a), Density profile for $V_0 = 100\,\mathrm{nK}$ over a rectangular unit cell. The primitive cell is outlined in red. (b) The superfluid fraction tensor components are plotted in solid lines. The superfluid fraction tensor diagonal components are equal and the off-diagonal elements vanish such that the tensor is proportional to the identity matrix. Unlike the square lattice, the Leggett bounds along x and y differ. The vertical gray dotted line indicates the chemical potential for $V_0 = 0$.

The primitive cell is a rhombus, as shown in fig. 4.4a. For convenience, we compute the superfluid fraction and bounds over a rectangular unit cell, larger than the primitive cell. The results are shown in fig. 4.4. The superfluid fraction tensor is proportional to the identity matrix, as seen in fig. 4.4b. However, the Leggett bounds along x and y directions differ. Notably, $f_+^{(y,y)}$ stays close to unity across the range of parameters explored in fig. 4.4b. This can be explained by observing that the average of the potential along direction x cancels out, meaning that in the linear regime, when the density modulation is proportional to the potential, $f_+^{(y,y)} = 1$. In special cases like this where the superfluid fraction tensor is diagonal in all bases, the upper and lower bounds can be refined by taking the minimum (for upper) or maximum (for lower) Leggett bound over all directions. When doing so, we find that the tightest lower bound is $f_-^{(y,y)}$ and the tightest upper bound is $f_+^{(x,x)}$.

While not plotted in the graphs above, we numerically computed the Saslow bound for the square and triangular lattices and confirmed that it matches the superfluid fraction obtained with twisted boundary conditions to our numerical accuracy.

4.3.3 Sound in superfluids

After establishing theoretical bounds on the superfluid fraction based on static density profiles, we now turn to a dynamic method for experimentally measuring this quantity. In our experimental work described in the next chapter, we determine the superfluid fraction through speed of sound measurements. In this subsection we quickly review sound propagation in superfluids with a focus on systems with broken translational invariance.

Landau predicted the existence of two sound modes in superfluid helium [7]. In helium, first sound is an "ordinary" density wave, while second sound is a pure entropy wave. Both

have been observed experimentally in liquid ^{4}He [252]. In cold atom systems, superfluidity is also linked to the existence of two sound modes, but unlike in liquid helium, these sounds generally do not correspond to pure entropy or density waves. Sound propagation has been extensively studied experimentally in cold atoms, both in bosonic gases [253–260] and fermionic gases [261–263].

In a uniform BEC, second sound at zero temperature is linked to the gapless Bogoliubov excitation spectrum. At low momenta, the excitation spectrum features a phononic branch $\epsilon(k) \underset{k\to 0}{\sim} ck$ with:

$$c = \sqrt{\frac{g\rho}{m}}, \tag{4.67}$$

where c is the second sound speed or Bogoliubov speed of sound. This phonon branch corresponds to the Goldstone mode of the spontaneously broken U(1) symmetry. In the more complex case of a supersolid, the additional Goldstone modes associated with broken translational invariance give rise to a richer excitation spectrum. Specifically, a supersolid with D-dimensional modulation features $D+1$ phononic excitation branches [264]. Analytical formulas for the associated sound speeds have been derived for the $D=1$ [265] and $D=2$ cases [238, 266]. The two Goldstone modes of a supersolid with a one-dimensional density modulation were observed in a dipolar supersolid in a harmonic trap [267, 268]. Recently, Liebster et al. measured two different sound speeds corresponding to two different phononic branches of a periodically driven supersolid in a flat-bottom trap [54].

Taking the limit of an infinitely rigid lattice in these formulas yields a single speed of sound along each direction:

$$c_i^2 = \frac{f_s^{(i,i)}}{\kappa m}, \tag{4.68}$$

where:

$$\kappa = \frac{\partial \rho}{\partial P} = \frac{1}{\rho}\frac{\partial \rho}{\partial \mu}, \tag{4.69}$$

is the compressibility and μ is the chemical potential. Equation (4.68) is thus valid for a BEC at zero temperature with an externally imposed modulation, and we recover eq. (4.67) for a uniform BEC. Therefore, by measuring compressibility and speed of sound along a direction, we can determine the superfluid fraction at zero temperature along that direction. For a one-dimensional modulation, the superfluid fraction along the direction perpendicular to the modulation is 1. We can therefore determine the superfluid fraction along the modulation direction by measuring $c_\perp$ and $c_{/\!/}$, the transverse and longitudinal sound speeds relative to the modulation direction:

$$f_s^{/\!/} = \frac{c_{/\!/}^2}{c_\perp^2}. \tag{4.70}$$

Speed of sound measurements provide a powerful method for determining the superfluid fraction in uniform systems at finite temperature. This technique has been applied to measure the superfluid fraction in three-dimensional Fermi gases [261] and in both two-dimensional [260] and three-dimensional [259] BECs. Alternative measurement methods include the scissors mode frequency [56, 228] and, in supersolids, the frequency of Josephson-like oscillations between density peaks [239].

Conclusion

This chapter reviewed the concept of superfluidity, beginning with its initial observation in liquid helium. We discussed how observed phenomena can be explained by considering the flow is made of two components: a superflow with zero viscosity and a normal flow analogous to that of a classical fluid. The rotating bucket thought experiment illustrates how, within a rotating container, only the normal component is dragged by the walls. This motivates the definition of the superfluid fraction as the factor quantifying the reduction in the system's response to rotation compared to a classical fluid.

Subsequently, we presented a more general definition of the superfluid fraction tensor, characterizing it through the system's response either to twisted boundary conditions or, equivalently, to a small Hamiltonian perturbation of the form $-\mathbf{v} \cdot \hat{\mathbf{P}}$.

We then focused on superfluidity at zero temperature, demonstrating that bosonic systems possessing both time-reversal symmetry and translational invariance exhibit a unit superfluid fraction at zero temperature. We explained, however, that breaking either of these symmetries leads to a reduction of the superfluid fraction below unity, even at $T = 0$.

Focusing on systems with broken translational invariance, we examined upper and lower bounds on the superfluid fraction. We detailed the origin of Leggett's bounds and Saslow's subsequent refinement of the upper bound, which provides a tighter constraint but requires a more complex calculation. Crucially, these bounds depend solely on the system's static density profile. In the specific case of a BEC, the Saslow upper bound is saturated, meaning the superfluid fraction is entirely determined by the density profile. These bounds are particularly relevant for supersolids, where translational invariance is broken spontaneously.

Looking ahead, the subsequent chapter will experimentally investigate the effect of periodic modulation on the superfluid fraction at zero temperature. These experiments utilize a BEC subjected to an external periodic potential, providing a controllable platform to study broken translational invariance, as realizing a supersolid state itself is not the focus of our current experimental work. The theoretical analysis presented earlier in this chapter examined this specific scenario to illustrate how periodic modulation affects the superfluid fraction and what information the bounds provide. Examples, including the 1D sinusoidal modulation and the triangular lattice geometries realized experimentally in the subsequent chapter, were discussed. Finally, we briefly reviewed sound propagation in superfluids and supersolids, explaining how measurements of the speed of sound, combined with the compressibility, give access to the superfluid fraction experimentally. Measuring these quantities, as well as calculating the bounds from density profiles, will be the experimental approach employed in the next chapter.

CHAPTER 5

Probing superfluidity experimentally in a spatially-modulated Bose-Einstein Condensate

Outline of the current chapter

The results presented in this chapter are preliminary and have not yet been published in a peer-reviewed journal. The corresponding manuscript is currently in preparation

Introduction

After describing in the previous chapter the theoretical framework used for studying spatially-modulated superfluids at zero temperature, this chapter presents our experimental work dedicated to studying the superfluid fraction of a BEC subjected to an externally imposed periodic modulation. This chapter primarily focuses on the case of a triangular lattice modulation, although experiments were also performed with one-dimensional sinusoidal modulations; for the latter, we only present the final results.

In section 5.1, we present the experimental platform used for this work, with particular emphasis on explaining how the lattice potential is generated using a DMD. We also provide the relevant experimental parameters.

In section 5.2, we detail the characterization of the potential used for the experiment. We also discuss the calibration of the imaging system and its importance for reliably characterizing the different bounds on the superfluid fraction from the measured density profile.

Finally, in section 5.3, we present our measurements of both the speed of sound and the compressibility of the atomic cloud, which allow us to compute the superfluid fraction. We also detail the measurement of Saslow's bound (which is saturated in our system) and Leggett's bounds, derived from the measured density profile. This section concludes with the results obtained for a one-dimensional modulation.

5.1 Experimental platform

5.1.1 Two sets of experimental parameters

As stated in the previous chapter we conduct an experimental investigation of the influence of a density modulation, here imposed externally using an optical potential, on the superfluid fraction of our two-dimensional cloud. We study two lattice geometries: the one-dimensional sinusoidal lattice and the triangular lattice. The two experiments were done two years apart, and the experimental parameters differ, but the experimental methods are roughly the same. One key difference is that for the one-dimensional lattice, the compressibility is not measured directly; the superfluid fraction is accessed by measuring the speed of sound along two directions and applying eq. (4.68). However, in the case of the triangular lattice, we measure both the speed of sound and compressibility. The experimental parameters for both lattices are given in table 5.1. The temperature of our cloud is below 20 nK, so we consider our gas to be at zero temperature. In both cases, we define V_0 the peak-to-peak depth of the lattice potential, as in section 4.3.2. Throughout this chapter, we often express V_0 in units of the chemical potential in the absence of the lattice, $\mu_0 = g\langle\rho\rangle$, where $\langle\rho\rangle$ is the mean density.

Parameters	One-dimensional lattice	Triangular lattice
Mean density (μm^{-2})	60(3)	51(2)
Lattice period (µm)	3.93(4)	6.0(1)
Box size (µm)	40.0(13)	42.0(8)
2D interaction parameter ($\times\hbar^2/m$)	0.15(1)	0.16(1)

Table 5.1: Experimental parameters for the two lattice geometries studied

For the remainder of the chapter, we will focus on the case of the triangular lattice. The one-dimensional case was already treated in previous PhD theses in our group [85, 86]. We will return to the one-dimensional lattice at the very end, where we will present only the final results.

5.1.2 Trap and lattice potentials

The experiment uses a two-dimensional Bose gas, trapped inside a box potential. The box is a square of size 42 µm, containing 7 lattice periods along the y direction.

As stated in chapter 1, the periodic potential is generated by a far off-resonant blue-detuned laser-beam at a wavelength of $\lambda = 532$ nm. The laser beam is shaped using DMD2

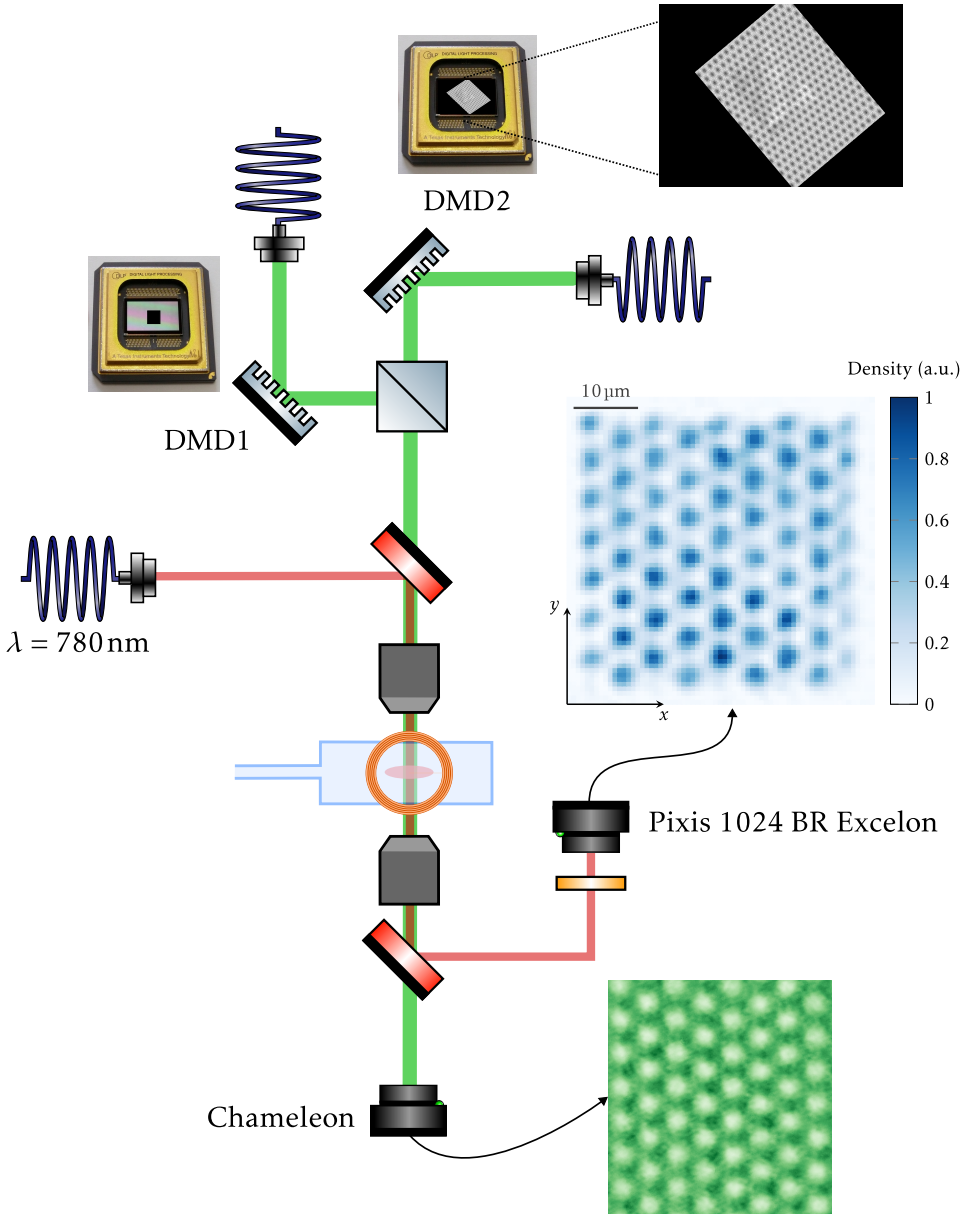

Figure 5.1: Layout of the experimental setup. Two DMDs are used for this project, both illuminated with blue-detuned light at a wavelength $\lambda = 532\,\mathrm{nm}$. DMD1 is used to generate the box potential whereas DMD2 is used to imprint the periodic lattice potential, in this case a triangular lattice. The picture loaded on DMD2 is displayed, consisting of a dithered triangular lattice pattern multiplied by the result of the feedback loop as explained in the main text. Both DMDs are imaged through a microscope objective onto the atomic cloud. The light is then collected by an identical microscope objective and imaged on the control camera (Chameleon). The atomic cloud is imaged using absorption imaging at $\lambda = 780\,\mathrm{nm}$, with a PIXIS camera. We display an absorption image of the cloud taken for a lattice potential depth $V_0 \approx 4.3\,\mu_0$, averaged 40 times, we also display the corresponding intensity profile taken by the control camera. The atoms are in a magnetic-field sensitive state ($|F = 1, m_F = -1\rangle$), and the MOT coils generate a magnetic field gradient, used for both speed of sound and compressibility measurements.

and imaged onto the atomic cloud. Most cold-atom experiments generate optical lattices by making several beams interfere. Using a DMD offers high versatility in generating optical potentials without changing the optical setup. For a given lattice geometry, the image displayed on DMD2 remains the same; the depth of the lattice is varied by changing the incident laser intensity on the DMD, I_{DMD}. The density of the cloud is measured through absorption imaging. We also have a CCD camera in a plane conjugated to the atomic plane that specifically monitors the light coming from the DMD; this camera is referred to as the control camera.

A layout of the experimental setup is presented in fig. 5.1.

5.1.3 Profile on DMD

We determined that imprinting a triangular lattice profile directly on the DMD resulted in an inhomogeneous lattice on the atoms. These inhomogeneities arise from both the non-uniformities of the incident laser beam on the DMD and the defects introduced during the propagation between DMD2 and the atomic plane.

To solve this problem, we use a feedback loop developed earlier in our team [269]. The loop computes the distance between the absorption images of the cloud and a desired target, then adjusts the profile displayed on the DMD. Rather than targeting a triangular lattice profile (since beyond the Local Density Approximation (LDA) regime, density modulation is a non-linear function of the lattice potential), we use a flat density profile as our target. To correct only the defects of the DMD, we set as a target for the feedback loop a profile obtained by averaging 40 absorption images of the cloud without any light on DMD2. We set I_{DMD} to a value approximately 4 times higher than the maximal value used for the triangular lattice, thereby maximizing the error signal of the feedback loop. To estimate the convergence of the loop, we use the following root-mean-square deviation from the target:

$$\mathcal{F}_m = \frac{\sqrt{\sum_{(i,j)\in \mathrm{Im}} \left[\mathrm{OD}(i,j) - t(i,j)\right]^2}}{\sum_{(i,j)\in \mathrm{Im}} \mathrm{OD}(i,j)}, \tag{5.1}$$

where $(i,j) \in \mathrm{Im}$ denotes the pixels of the image, $t(\cdot)$ is the target profile and $\mathrm{OD}(\cdot)$ the measured optical density of the cloud. The optical density profile is obtained by averaging 10 absorption images. Figure 5.2 shows the difference between the optical density and the target profile before and after the loop, along with the reduction in the figure of merit through iterations of the feedback loop. After the convergence of the loop, we obtain a DMD profile $c(x,y)$.

We want to imprint a triangular lattice on the atoms, so a potential proportional to:

$$v(x,y) = -\left[\cos\left(\frac{4\pi}{\sqrt{3}p}x\right) + \cos\left(\frac{2\pi}{\sqrt{3}p}x + \frac{2\pi}{p}y\right) + \cos\left(-\frac{2\pi}{\sqrt{3}p}x + \frac{2\pi}{p}y\right)\right], \tag{5.2}$$

where $p = 6\,\mu\mathrm{m}$ represents the period of the lattice. To generate a homogeneous lattice, we modify the pattern displayed on the DMD by incorporating the correction profile obtained from the feedback loop. The function ultimately imprinted on the DMD is thus:

$$g(x,y) = c(x,y)\sqrt{A + Bv(x,y)}, \tag{5.3}$$

where the numerical coefficients A and $B > 0$ are adjusted to ensure that $0.1 \leq g^2(x,y) \leq 1$ for all values of x and y (see section 1.2.5).

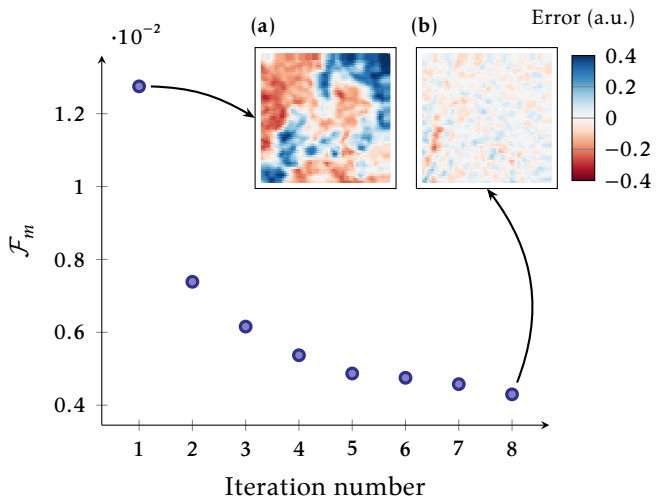

Figure 5.2: Feedback loop for DMD2, using the measured atomic profile with DMD2 turned off as target. The figure of merit is plotted as a function of loop iteration. Iteration number 1 corresponds to the initial state before any correction. After 7 iterations, the loop converges to a profile with a figure of merit more than three times smaller than the initial one. Insets (a) and (b) represent the difference between the measured atomic profile and the target profile for iterations 1 and 8, respectively.

5.2 Calibration of the system

5.2.1 Optical characterization of the lattice potential

To characterize the potential imprinted by DMD2 on the atoms, we use the intensity profiles recorded on the control camera. The potential seen by the atoms is proportional to the light intensity (see section 1.2.2) with a positive proportionality coefficient. Therefore, the lattice potential is proportional to the intensity profile on the control camera[1]. To characterize the potential, we fit the intensity profile on the control camera using the following function:

$$I_{\text{fit}}(\mathbf{r}) = C_0 - C_1 \cos\left(\mathbf{k}_1 \cdot \mathbf{r} - \phi_1\right) - C_2 \cos\left(\mathbf{k}_2 \cdot \mathbf{r} - \phi_2\right) - C_3 \cos\left(\mathbf{k}_2 \cdot \mathbf{r} - \mathbf{k}_1 \cdot \mathbf{r} - \phi_3\right), \quad (5.4)$$

where C_1, C_2 and C_3 are positive. The fit parameters are $C_0, \ldots, C_3$, ϕ_1, ϕ_2, ϕ_3 and $\mathbf{k}_1, \mathbf{k}_2$, totaling 11 scalar parameters. The function above describes a broader range of potentials than the ideal triangular lattice studied in the previous chapter. For eq. (5.4) to represent an ideal triangular lattice, the following conditions must be satisfied:

- $C_1 = C_2 = C_3$.
- $\theta_{1,2} = \pi/3$, where $\theta_{1,2}$ is the angle between vectors $\mathbf{k}_1$ and $\mathbf{k}_2$.
- $\|\mathbf{k}_1\| = \|\mathbf{k}_2\|$.
- $\varphi = \phi_1 - \phi_2 + \phi_3 = 0$.

Note that changing the relative phase of the three cosines while keeping φ constant offsets the position of the lattice without altering its shape, such that only the parameter φ is relevant.

[1]We will discuss this assertion later.

Our fit results are:

- $C_2/C_1 = 1.00(2)$, $C_3/C_1 = 0.98(2)$.
- $\theta_{1,2} = 58.5(1)°$.
- $\|\mathbf{k}_1\|/\|\mathbf{k}_2\| = 1.03(1)$.
- $\varphi = -37.5(15)°$.

The fit results show that the first three conditions for an ideal triangular lattice are almost satisfied, but the last condition, on φ, is not. We therefore model the potential seen by the atoms as a generalized triangular lattice:

$$V(\mathbf{r}) = -\frac{2V_0}{9}\left[\cos(\mathbf{k}_1\cdot\mathbf{r}) + \cos(\mathbf{k}_2\cdot\mathbf{r}) + \cos(\mathbf{k}_3\cdot\mathbf{r} - \varphi)\right] \tag{5.5a}$$

$$\text{with} \quad \mathbf{k}_j = k\begin{pmatrix}\cos\left[(j-1)\pi/3\right]\\ \sin\left[(j-1)\pi/3\right]\end{pmatrix}, \quad k = \frac{4\pi}{\sqrt{3}p}, \tag{5.5b}$$

where the period of the lattice is $p = 6\,\mu\text{m}$ and the phase is $\varphi = -37.5°$. The potential described by eq. (5.5) corresponds to the triangular lattice potential introduced in eq. (4.66), with the addition of a relative phase φ in the third term. All the GPE simulation results presented in this chapter were obtained using this potential and these parameters.

We confirm the value of φ by examining the atomic response at low potential depth, where the density modulation is proportional to the potential. By fitting the density modulation of the cloud with the function in eq. (5.4), we find $\varphi_{\text{at}} = -41.0(15)°$.

Changing the parameter φ affects the superfluid fraction of the system. However, when varying this parameter, the superfluid fraction tensor remains proportional to the identity matrix.

5.2.2 Density response to a lattice potential

After characterizing the lattice on the control camera, we need to calibrate the depth of the potential on the atomic plane. Experimentally, we control I_{DMD}, the incident intensity on DMD2, and aim to determine the corresponding potential depth on the atoms. According to eq. (1.3), this can be achieved by knowing the intensity in the atomic plane. However, this intensity cannot be measured directly, as the atoms are inside the glass cell. Determining the intensity in the atomic plane would require an accurate estimation of the beam waist on the atoms and the losses in our optical system, which cannot be characterized with sufficient precision. Consequently, we rely on the atomic response for calibration.

5.2.3 Calibration of the lattice potential

5.2.3.1 Density response to a lattice potential.

To calibrate the lattice potential, we need to understand the atomic response to such a potential. The GPE reads:

$$\mu\psi = -\frac{\hbar^2}{2m}\nabla^2\psi + g\left|\psi\right|^2\psi + V(x,y)\psi, \tag{5.6}$$

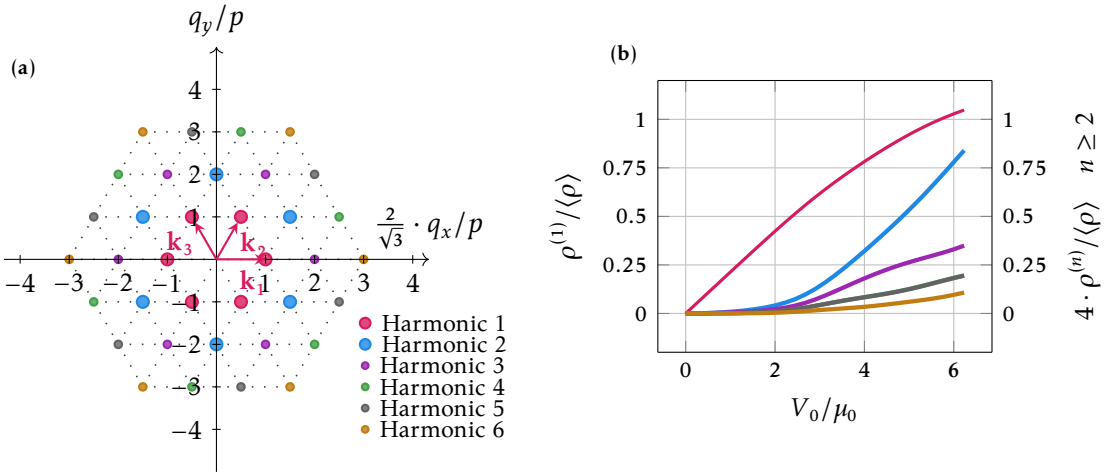

Figure 5.3: Harmonics of the triangular lattice. (a) The locations of the Fourier peaks for different harmonics are plotted. Each color represents a different harmonic; we display the first six harmonics. We also plot the lattice vectors $\mathbf{k}_1$, $\mathbf{k}_2$ and $\mathbf{k}_3$. (b) Amplitude of each harmonic as a function of the potential depth normalized to μ_0, computed from GPE simulations. The weights of harmonics two and above are rescaled by a factor of 4 to enhance readability. The curve for harmonic 4 is not visible because it is underneath the curve for harmonic 5.

where $V(x, y)$ is the external periodic potential. The density $\rho(x, y) = |\psi|^2$ can be expanded in Fourier series. For the generalized triangular lattice given by eq. (5.5), we can write:

$$\rho(\mathbf{r}) = \langle\rho\rangle + \sum_{n>0} \rho^{(n)} h^{(n)}(\mathbf{r}) \tag{5.7}$$

$$\text{with} \quad h^{(n)}(\mathbf{r}) = \left[\cos\left(\mathbf{q}_1^{(n)} \cdot \mathbf{r} - \phi_1^{(n)}\right) + \cos\left(\mathbf{q}_2^{(n)} \cdot \mathbf{r} - \phi_2^{(n)}\right) + \cos\left(\mathbf{q}_3^{(n)} \cdot \mathbf{r} - \phi_3^{(n)}\right)\right], \tag{5.8}$$

where the amplitudes $\rho^{(n)}$ are positive. All harmonics have the shape of generalized triangular lattices, meaning the three vectors $\mathbf{q}_i^{(n)}$ have the same norm $q^{(n)}$ for a given n, and the angle between $\mathbf{q}_1^{(n)}$ and $\mathbf{q}_2^{(n)}$ equals the angle between $\mathbf{q}_2^{(n)}$ and $\mathbf{q}_3^{(n)}$ (which is $\pi/3$). The period of the n-th harmonic is $\sqrt{3}q^{(n)}/4\pi$, with harmonics ordered by decreasing period. The vectors of the first harmonic $\mathbf{q}_1^{(1)}$, $\mathbf{q}_2^{(1)}$ and $\mathbf{q}_3^{(1)}$ correspond to the lattice vectors $\mathbf{k}_1$, $\mathbf{k}_2$ and $\mathbf{k}_3$, respectively. For the second harmonic, $\mathbf{q}_1^{(2)} = \mathbf{k}_1 + \mathbf{k}_2$, with period $p^{(2)} \approx 3.46\,\mu\text{m}$, and for the third harmonic, $\mathbf{q}_1^{(3)} = 2\mathbf{k}_1$ with period $p^{(3)} = 3\,\mu\text{m}$. Figure 5.3a shows the locations of the Fourier peaks for the first 6 harmonics.

5.2.3.2 Characterization of the spatial frequency response

We calibrate the potential depth using the atomic response, specifically by examining the response of the first harmonic $\rho^{(1)}$ in the low potential regime. An expansion of the GPE in powers of V_0 yields:

$$\frac{\rho^{(1)}}{\langle\rho\rangle} = \frac{2V_0}{2\mu_0 + \epsilon_k} + \mathcal{O}(V_0^3), \tag{5.9}$$

with $\epsilon_k = \hbar^2 k^2/2m$ being the recoil energy of the lattice and $\mu_0 = g\langle\rho\rangle$ the chemical potential for the uniform condensate. However, to reliably calibrate V_0, we must account

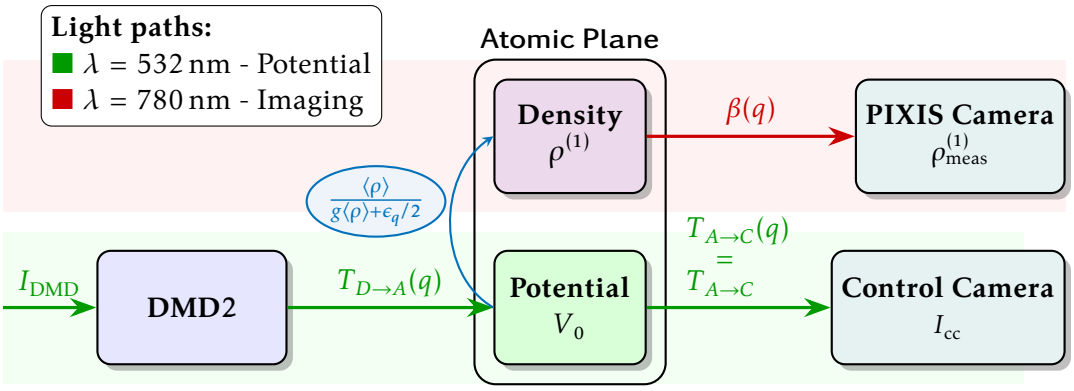

Figure 5.4: Diagram of our model for the optical system, showing the different transfer functions between elements. All transfer functions are assumed to be rotationally invariant, depending only on the wave vector norm. A triangular lattice with wave vector q is displayed on DMD2. A laser beam of intensity I_{DMD} at wavelength $\lambda = 532\,\mathrm{nm}$ illuminates the DMD, generating a triangular lattice potential with amplitude V_0 at the atomic plane. This potential creates a density modulation that can be decomposed into harmonics. The transfer function between V_0 and the amplitude of the first harmonic $\rho^{(1)}$ is given, at low V_0, by the equation in the blue ellipse. The cloud is imaged using absorption imaging with a laser beam at $\lambda = 780\,\mathrm{nm}$. The amplitude of the measured density modulation is $\rho^{(1)}_{\mathrm{meas}}$. A control camera on a plane conjugated to the atomic plane records the intensity modulation of the green light with amplitude I_{cc}. We assume that the transfer function between the atomic plane and the control camera is constant for the relevant spatial frequencies.

for the finite resolution of our imaging system, which acts as a low-pass filter for spatial frequencies. We assume the imaging system has a rotationally invariant filter in Fourier space, such that the density measured using absorption imaging is:

$$\rho_{\mathrm{meas}}(x,y) = \langle\rho\rangle + \sum_{n>0} \beta\left(q^n\right)\rho^{(n)}h^{(n)}(\mathbf{r}), \tag{5.10}$$

where $\beta(q)$ is the attenuation[2] at wave vector q. The measured amplitude of harmonic n is then $\rho^{(n)}_{\mathrm{meas}} = \beta\left(q^{(n)}\right)\rho^{(n)}$. To calibrate the potential depth using the measured density profile at low lattice depth, we rewrite eq. (5.9):

$$V_0 \approx \left(g + \frac{\epsilon_k}{2}\right)\rho^{(1)}_{\mathrm{meas}}/\beta\left(k\right), \tag{5.11}$$

Thus, we need to measure both the density response of the BEC and the $\beta(k)$ coefficient. Determining the β coefficients is crucial not only for calibrating the lattice depth but also for reconstructing the actual density profile from measurements, which will be essential for computing the bounds on the superfluid fraction. Therefore, we need the β coefficients for higher harmonics as well.

5.2.3.3 Calibration of the β coefficients

To calibrate the β coefficients, we model our system as described in fig. 5.4. We make two assumptions: first, that the light propagation between DMD2 and the atomic plane can be modeled in Fourier space by a rotationally invariant transfer function $T_{D\to A}(\mathbf{q}) = T_{D\to A}(q)$;

[2]The β coefficients take also other effects into account, such as the contrast decrease due to pixelization effects on the PIXIS camera.

second, that the intensity profile observed on the control camera is proportional to the intensity profile on the atomic plane. In other words, the transfer function $T_{D\to C}$ is independent of spatial frequency across the range studied here.

The parameters we need to calibrate are:

- The coefficient relating I_{DMD} (the beam intensity sent to $DMD2$) to the corresponding potential depth V_0 when imprinting a triangular lattice with 6 µm period.
- The β coefficients for different harmonics of the triangular lattice to reliably reconstruct the density profile.

Our approach examines the first harmonic of the density modulation. For $\beta\left(q^{(n)}\right)$ coefficients of higher harmonics, we take advantage of the versatility of the DMD by directly imprinting triangular lattice potentials corresponding to these higher harmonics.

Our calibration procedure is as follows: we load a triangular lattice pattern on DMD2 with wave vector q and vary I_{DMD} while measuring:

- $\rho^{(1)}_{\mathrm{meas}}(q)$, the amplitude of the first harmonic of the density modulation, to compute the slope $\alpha_{\mathrm{at}}(q) = \rho^{(1)}_{\mathrm{meas}}(q)/I_{\mathrm{DMD}}$ for low potential depths. This slope is proportional to $T_{D\to A}(q) \times \beta(q)$.
- $I_{\mathrm{cc}}(q)$, the intensity modulation amplitude recorded by the control camera, to compute the slope $\alpha_{\mathrm{cc}}(q) = I_{\mathrm{cc}}(q)/I_{\mathrm{DMD}}$. This slope is proportional to $T_{D\to A}(q) \times T_{A\to C}$.

Since we have two measurements for three quantities ($T_{D\to A}(q)$, $T_{A\to C}$, and $\beta(q)$), we cannot fully characterize the system. To resolve this, we also measure at a small q value for which we assume $\beta(q) = 1$, using a lattice with period 24 µm. Figure 5.5 shows the measurements of $\alpha_{\mathrm{at}}(q)$ and $\alpha_{\mathrm{cc}}(q)$.

Using this approach, we determine the β coefficient for the first two harmonics: $\beta(q^{(1)}) = 0.71(4)$ and $\beta(q^{(2)}) = 0.36(16)$. We also establish the calibration relating V_0 to I_{DMD}.

5.3 Experimental measurement of the superfluid fraction, and its bounds

Now that we have described the calibration procedure, we focus on measuring the superfluid fraction as well as Leggett's and Saslow's bounds. The superfluid fraction is determined by combining two dynamic measurements: the speed of sound and the compressibility. The bounds are calculated using the static density profile of the cloud.

5.3.1 Measurement of Saslow's and Leggett's bounds

5.3.1.1 Reconstruction of the profile for Leggett's and Saslow's bound calculation

Once the β coefficients have been calibrated, density profiles can be reconstructed up to our imaging resolution. We fit the density profile to obtain the weights of the harmonics, $\rho^{(n)}_{\mathrm{meas}}$, and then divide each weight by the corresponding attenuation coefficient $\beta(q^{(n)})$ to reconstruct the density profile at the atomic plane. Since we only have a signal for the first two harmonics, we have calibrated the β coefficients only for the 6 µm and 3.46 µm periods.

When using the density profile to compute Leggett's and Saslow's bounds, a question arises: are two harmonics sufficient for reliable estimation? At higher values of V_0, higher harmonics have greater relative weight (as shown in fig. 5.3b). For values of V_0 high

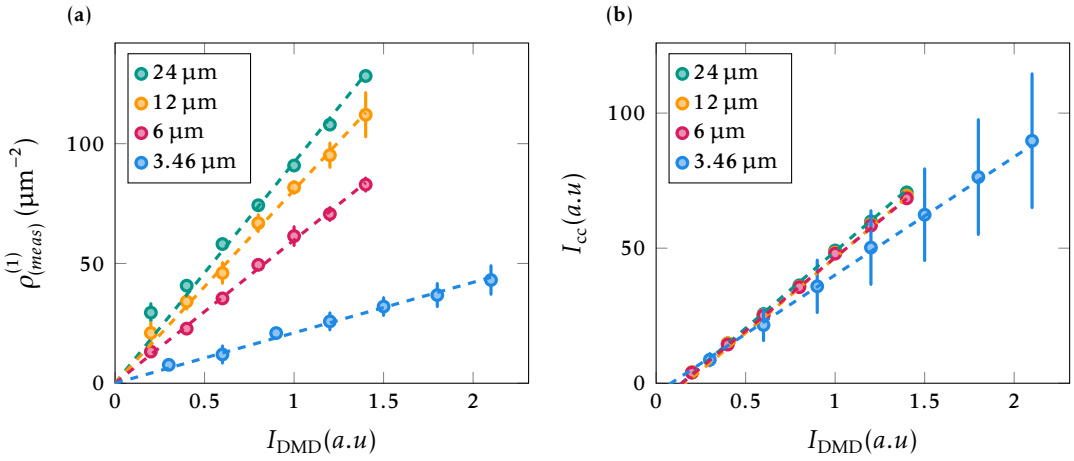

Figure 5.5: Calibration of the β coefficients. Triangular lattices of different periods are imprinted on DMD2. The point at period 12 µm is not used for the calibration but serves to verify the flatness of the transfer functions at low spatial frequency. (a) Density modulation amplitude versus incident beam intensity on DMD2; dotted lines show linear fits. The fitted slopes represent the coefficients $\alpha_{at}(q)$. The slopes for the two largest lattice periods are nearly identical, confirming that the transfer functions remain flat at large periods. (b) Intensity modulation amplitude on the control camera; dotted lines show linear fits yielding the coefficients $\alpha_{cc}(q)$. Again, the slopes for the largest lattice periods are nearly equal.

enough, typically above $3\,\mu_0$, filtering the density profile and keeping only the first two harmonics can result in negative density values, as shown in fig. 5.6. This causes $1/\rho$ to diverge, making the computation of Saslow's bound and Leggett's lower bound impossible.

To address this issue, we adopt the following procedure: after reconstructing the density profile using the first two harmonics, we set all values below a numerical cut-off (in our case 10^{-20}) to this cut-off. This ensures a positive reconstructed density profile. We benchmark this procedure against density profiles from GPE simulations. The results are shown in fig. 5.7. For the parameter range explored experimentally, we conclude that this procedure allows reliable estimation of all bounds.

5.3.1.2 Measured amplitudes of the harmonics

The density profile ρ_{meas} is obtained by averaging 40 absorption images. We fit these profiles to extract the mean density and the weights of the first two harmonics, $\rho^{(1)}_{meas}$ and $\rho^{(2)}_{meas}$. Each weight is rescaled by its corresponding β coefficient, the results obtained are displayed in fig. 5.8. Using these two harmonics we reconstruct a density profile with a lower threshold ensuring the density remains positive everywhere. From this reconstructed profile, we compute the Leggett lower bounds along the x and y directions using eqs. (4.60) and (4.61), as well as the upper bounds using eqs. (4.33) and (4.34). We also compute Saslow's upper bound, which is saturated in our system as it is governed by the GPE. The data analysis presented in this subsection was conducted by another PhD student, Sarah Wattellier, the final results are presented in fig. 5.11a.

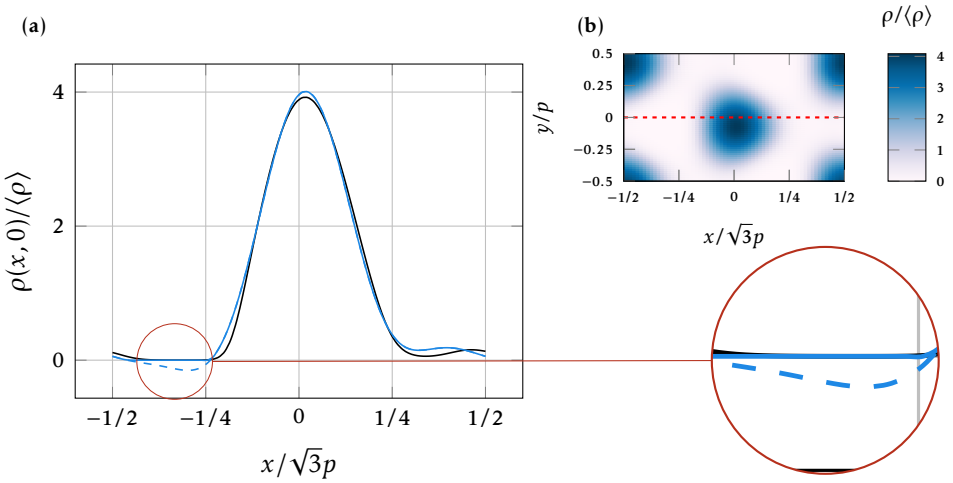

Figure 5.6: Density profile for $V_0 = 5.11\,\mu_0$ from a GPE simulation. (a) Density at $y = 0$ over a unit cell: the black solid line shows the density profile directly from simulation; the blue dashed line (mostly overlapping with the blue solid line) shows the density reconstructed using only the first two harmonics. This reconstructed density becomes negative at some points; a non-physical situation that prevents computation of Saslow's upper bound and Leggett's lower bound. By setting a small threshold (here 10^{-20}) to which all values below it are set, we obtain the solid blue curve, which closely approximates the unfiltered density profile. (b) The density distribution over a unit cell; the red dotted line indicates the cross-section plotted in panel (a).

5.3.2 Dynamical measurement of the superfluid fraction tensor

We now present the measurements of speed of sound and compressibility used to compute the superfluid fraction. Since the superfluid fraction tensor is isotropic for a triangular lattice potential, we measure the speed of sound only along a single direction, y in our case.

5.3.2.1 Speed of sound measurement

Density oscillations in a box The speed of sound in a homogeneous two-dimensional gas was measured previously in our group [258]. We use the same method, which works for gases confined in flat-bottom rectangular traps. To measure the speed of sound along the y direction, we excite the longest-wavelength sound mode of the box (wavelength $\Lambda = 2L_y$) and measure its frequency:

$$\nu_y = \frac{c_y}{2L_y}, \tag{5.12}$$

where L_y and c_y are the box size and speed of sound along direction y, respectively. The oscillation frequency can be measured either by examining the system's response to a drive as in refs. [258–260] or by analyzing the impulse response as in ref [258] and in this work.

To observe the impulse response, we prepare the system with a small density perturbation; in our case, a small linear density tilt given by $\delta\rho\, y/L_y$ where $\delta\rho \ll \langle\rho\rangle$. This perturbation is released abruptly, triggering density oscillations. These oscillations can be

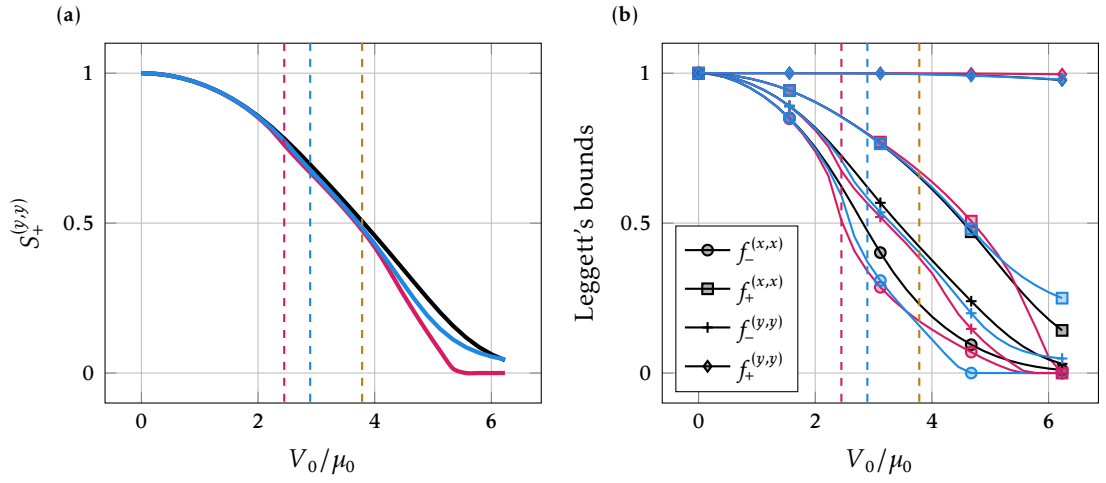

Figure 5.7: Benchmark of Leggett's and Saslow's bounds computed using one or two harmonics for density reconstruction, using profiles from GPE simulations. In all graphs, black curves show bounds computed directly from the original density profile; pink curves show bounds computed using only the first harmonic; and blue curves show bounds computed using the first and second harmonics. In both reconstructed cases, a lower threshold is applied to prevent negative density values. (a) Saslow bound versus potential depth. Using just two harmonics provides a very good estimation of the Saslow bound across the potential depths studied. (b) Leggett bounds versus potential depth, with markers indicating the corresponding bound. The pink, blue, and amber vertical dotted lines indicate where the reconstructed density, using the first harmonic, the first two harmonics, or the first six harmonics, respectively, reaches zero. Without applying a lower threshold, neither Saslow's bound nor Leggett's lower bound could be computed beyond these points.

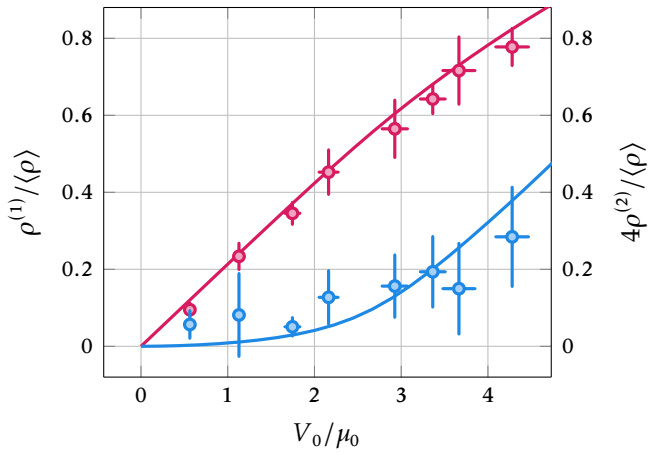

Figure 5.8: Amplitudes of the first two harmonics as a function of the normalized potential depth. The amplitudes are obtained by extracting the weight of the first two harmonics from the density profile. Each weight is then divided by the corresponding β coefficient to obtain the amplitudes plotted here. The pink points correspond to the first harmonic and the blue points to the second harmonic. The solid lines correspond to the amplitudes obtained with GPE simulations. The amplitudes of the second harmonic are rescaled by a factor of 4 to enhance readability.

decomposed into Fourier modes:

$$\rho(y,t) = \rho_0(y,t) + \sum_{j=1}^{\infty} W_j(t) \cos\left(\frac{\pi j}{L_y} y - \frac{\pi j}{2}\right), \tag{5.13}$$

where $\rho_0(y,t)$ is the equilibrium density. We include only cos terms so that the velocity vanishes at the box walls, at $y = \pm L_y/2$. For an initial linear tilt, the non-zero coefficients at $t = 0$ are those with odd indices. The lowest excited mode (at $j = 1$) has an initial weight $W_1 = 4\delta\rho/\pi^2$. The next excited mode (at $j = 3$) has an initial weight $W_3 = W_1/9$, so the tilt perturbation primarily excites the lowest mode. Provided that $\Lambda \gg p$, the amplitude W_j will oscillate at frequency ν_y.

Measuring the oscillation frequency To observe these oscillations experimentally, we monitor the CoM dynamics:

$$\Delta y = \frac{1}{N} \int_{-L_y/2}^{L_y/2} \int_{-L_x/2}^{L_x/2} y\rho(x,y)\,\mathrm{d}x\,\mathrm{d}y\,, \tag{5.14}$$

where $N = \int \rho(x,y)\,\mathrm{d}x\,\mathrm{d}y$ is the total number of atoms in the system. The CoM oscillates at frequency ν_y. We fit its evolution to a damped sinusoidal oscillation with no initial velocity:

$$\Delta y_0 + A\,\mathrm{e}^{-\Gamma_y t/2}\left(\frac{\Gamma_y}{2\omega_y}\sin(\omega_y t) + \cos(\omega_y t)\right), \tag{5.15}$$

where Δy_0, Γ_y, A, and ω_y are fit parameters. The frequency is determined using:

$$\nu_y = \sqrt{\omega_y^2 + (\Gamma_y/2)^2}/2\pi. \tag{5.16}$$

Experimentally, we produce a cloud in the magnetic-field sensitive state $|F = 1, m_F = -1\rangle$, with a quantization field along the z direction, orthogonal to the atomic plane. The magnetic field produces, at lowest order, a uniform force in the atomic plane. We can adjust the direction and magnitude of this force by shifting the magnetic bias field in-plane. The typical magnetic field gradient used is approximately $5\,\mathrm{G\,m^{-1}}$. The results of the speed of sound measurements are shown in fig. 5.9.

5.3.2.2 Compressibility measurement

To measure the compressibility, we use a method inspired by ref. [270], deducing compressibility from the system's linear response to a constant force. We prepare the sample in the presence of a uniform force along the y direction and measure the resulting CoM shift. Experimentally, the protocol is similar to the speed of sound measurement, except that instead of removing the force abruptly and studying the time evolution, we maintain the force and measure the steady-state CoM displacement. The compressibility is then calculated from the CoM response using:

$$\kappa = \frac{12}{L_y^2}\frac{\Delta y(F) - \Delta y_0}{F}, \tag{5.17}$$

where $\mathbf{F} = F\mathbf{e}_y$ is the force applied to the atoms. A proof of this formula is provided below.

Since we generate the force experimentally using a magnetic gradient, we can express

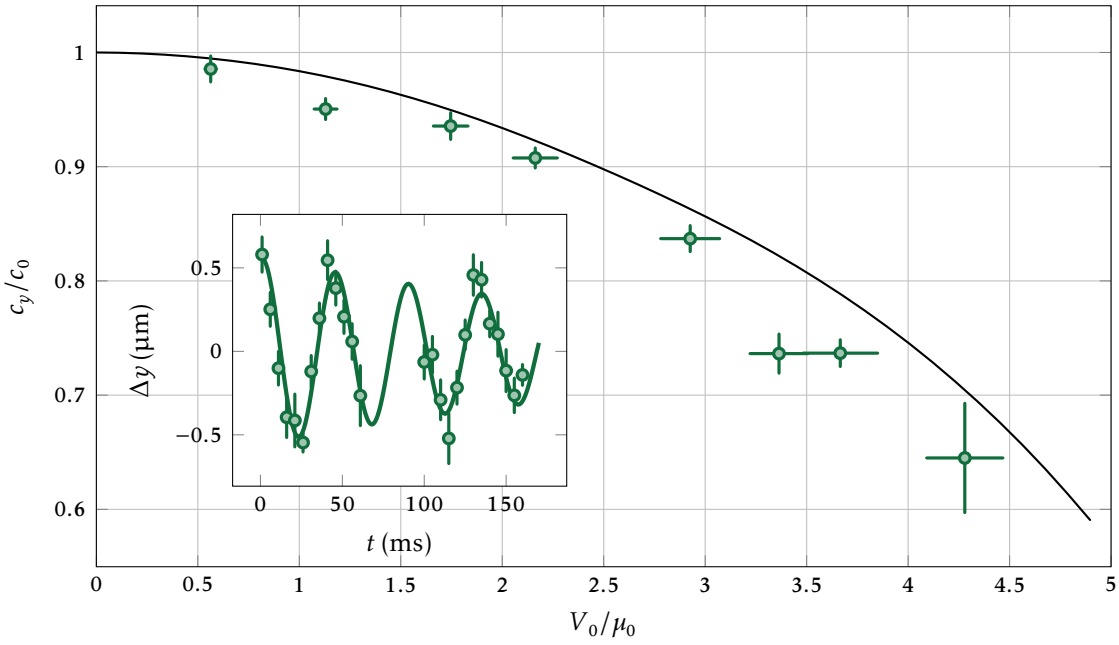

Figure 5.9: Speed of sound along y normalized to the speed of sound in a uniform condensate $c_0 = \sqrt{g\langle\rho\rangle/m}$ versus normalized potential depth. Green points show measurements from CoM oscillation frequencies; the solid black line shows the prediction from numerical GPE simulations. The inset shows CoM position versus time for one oscillation measurement at potential depth $V_0 \approx 2.2\,\mu_0$, with a magnetic gradient of $6\,\mathrm{G\,m^{-1}}$ applied for $t < 0$. Green circles show experimental data (each point averages 10 experimental iterations); the green solid line is a fit using the function from eq. (5.15).

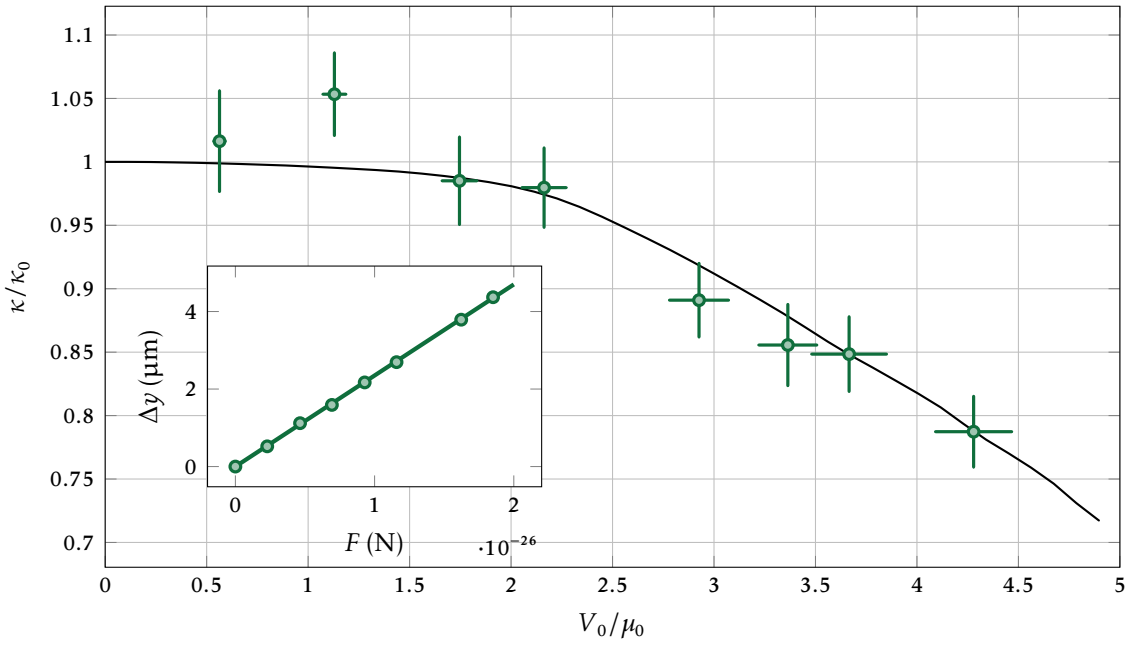

Figure 5.10: Compressibility normalized to the compressibility of a uniform condensate $\kappa_0 = 1/g\langle\rho\rangle$ versus normalized potential depth. Green points show measurements from the response of the system to a uniform force (magnetic gradient); the solid black line shows the prediction from numerical GPE simulations. The inset shows such a measurement at potential depth $V_0 \approx 2.2\,\mu_0$. Green circles show the CoM shift versus applied force, with each point averaged over 40 iterations, the error bars are smaller than the point size. The solid green line shows a linear fit, from which we extract the compressibility using eq. (5.17). The maximum applied force corresponds to a magnetic gradient of $40\,\mathrm{G\,m^{-1}}$.

the compressibility in terms of b_y, the gradient component along y:

$$\kappa = \frac{12\left(\Delta y(b_y) - \Delta y_0\right)}{L_y^2 \mu_b g_F m_F b_y}, \tag{5.18}$$

where for the hyperfine state $|F = 1, m_F = -1\rangle$, the Landé factor $g_F = -1/2$. We verified numerically that eq. (5.18) remains valid, in the presence of a lattice, for values of $b_y < 75\,\mathrm{G\,m^{-1}}$ [86].

In principle, the compressibility could be obtained from the speed of sound measurements, as the amplitude A in eq. (5.15) gives $\Delta y(F) - \Delta y_0$. However, we perform a separate measurement for compressibility, using gradients up to $40\,\mathrm{G\,m^{-1}}$ to improve the signal-to-noise ratio. Such forces would produce highly damped oscillations in the dynamic measurements. The results of these compressibility measurements are shown in fig. 5.10.

Proof of eq. (5.17) Equation 5.17 is valid for any lattice geometry. To prove it, we assume a lattice vector or combination of lattice vectors collinear with $\mathbf{e}_y$. The density profile is thus periodic along y with period p_y. We further assume that p_y is commensurate with the system size along y: $L_y/p_y = \mathcal{N}_y \in \mathbb{N}$. In our experiment $\mathcal{N}_y = 7$. We assume $\mathcal{N}_y$ is odd, though the reasoning can be adapted for even $\mathcal{N}_y$.

In the absence of a force, the static GPE reads:

$$\mu\psi = -\frac{\hbar^2}{2m}\nabla^2\psi + g\left|\psi\right|^2\psi + V(x,y)\psi, \tag{5.19}$$

with μ as the chemical potential and $\rho_0 = \left|\psi\right|^2$ as the density. When we add a force $\mathbf{F} = F\mathbf{e}_y$, we define ϕ as the new ground state.

We apply the LDA over intervals $[-L_y/2 + (l-1/2)p_y, -L_y/2 + (l+1/2)p_y]$ for $l \in \mathbb{N}$, centered at $y_l = -L_y/2 + lp_y$, assuming each interval has a local chemical potential μ_l. This approximation is valid when the energy Fp_y is small compared to other energy scales. Within interval l, we can approximate $Fy \approx Fy_l$, and the GPE becomes:

$$(\mu + Fy_l)\phi \approx -\frac{\hbar^2}{2m}\nabla^2\psi + g\left|\psi\right|^2\psi + V(x,y)\psi. \tag{5.20}$$

Thus, $\mu_l = \mu + Fy_l$. The compressibility is defined as:

$$\kappa = \frac{1}{\langle\rho\rangle}\frac{\partial\langle\rho\rangle}{\partial\mu}. \tag{5.21}$$

Expanding to first order in μ, the mean density in interval l becomes:

$$\langle\rho\rangle_l \approx \langle\rho_0\rangle(1 + \kappa F y_l). \tag{5.22}$$

We can now calculate the CoM shift caused by the force by summing over all intervals:

$$\begin{aligned}\Delta y - \Delta y_0 &= \frac{1}{N}\int_{-L_y/2}^{L_y/2}\int_{-L_x/2}^{L_x/2} y\left(\rho(x,y) - \rho_0(x,y)\right)\mathrm{d}x\,\mathrm{d}y \\ &= \frac{1}{N}\sum_{l=1}^{\mathcal{N}_y}\left[-\frac{L_y}{2} + \left(l - \frac{1}{2}\right)p_y\right]\left(\langle\rho\rangle_l - \langle\rho_0\rangle\right)L_x p_y,\end{aligned} \tag{5.23}$$

Substituting eq. (5.22), we obtain:

$$\Delta y - \Delta y_0 = \frac{\langle\rho_0\rangle\kappa L_x p_y F}{N}\sum_{l=1}^{\mathcal{N}_y}\left[-\frac{L_y}{2} + \left(l - \frac{1}{2}\right)p_y\right]^2 = \frac{\langle\rho_0\rangle\kappa L_x p_y^3 F}{N}\sum_{j=(-\mathcal{N}_y+1)/2}^{(\mathcal{N}_y-1)/2} j^2. \tag{5.24}$$

Approximating $\sum_{j=(-\mathcal{N}_y+1)/2}^{(\mathcal{N}_y-1)/2} j^2 \approx \mathcal{N}_y^3/12$ and using $\langle\rho_0\rangle L_x p_y \mathcal{N}_y = N$, we find:

$$\Delta y - \Delta y_0 = \frac{L_y^2 F\kappa}{12}, \tag{5.25}$$

which is equivalent to eq. (5.17).

Once both compressibility and speed of sound are measured, we calculate $f_s^{(y,y)}$ using eq. (4.68):

$$f_s^{(y,y)} = mc_y^2\kappa. \tag{5.26}$$

For the triangular lattice, the superfluid fraction tensor is proportional to the identity matrix. We therefore define the diagonal component of the superfluid fraction tensor as $f_s = f_s^{(y,y)} = f_s^{(x,x)}$.

5.3.3 Final results

All experimental results for the triangular lattice are summarized in fig. 5.11, along with predictions from GPE simulations.

We observe good agreement between the superfluid fraction obtained through our speed of sound and compressibility measurements and the GPE simulations. The discrepancy between experimental and numerical results increases with potential depth, with measured superfluid fractions consistently lower than theoretical predictions. By examining figs. 5.9 and 5.10, we find that this discrepancy stems primarily from the measured speed of sound being lower than numerical predictions. Several factors could explain these differences. First, finite temperature effects may play a role, our experiments were conducted at temperatures below 20 nK, however, we did not systematically investigate the influence of temperature on our measurements of κ and c, nor on the validity of eq. (5.26). Second, despite our efforts to ensure regularity of the imprinted potential (as described in section 5.1.2), residual irregularities may affect our results. Additionally, we observe that higher potential depths lead to increased damping of the CoM oscillations, though the precise origin of this damping remains unclear. Regarding Saslow's bounds, the vertical error bars are small but should be considered preliminary. These error estimates incorporate both statistical uncertainties in the β coefficients and fitting errors when extracting the harmonics. Excepted for the highest potential depth point, the agreement with numerical predictions is very good.

The measured Leggett's bounds show excellent agreement with theoretical predictions. The lower bound $f_-^{(x,x)}$ is slightly below numerical predictions, which is expected given that we only include the first two harmonics in our analysis (see fig. 5.7b). Similar to our observations with Saslow's upper bound, the measurement at the highest potential depth falls above the numerical predictions (except for $f_-^{(x,x)}$). The error bars for these measurements are also preliminary. Overall, our approach of estimating Saslow's and Leggett's bounds using only the first two harmonics yields satisfactory results across the range of potential depths studied.

This chapter has focused on the triangular lattice geometry. However, we performed the same experiment with a one-dimensional sinusoidal lattice using slightly different experimental parameters, as shown in table 5.1. The key difference for the sinusoidal lattice is that we did not measure compressibility directly. Instead, we measured the speed of sound along both the longitudinal ($c_{/\!/}$) and transverse ($c_\perp$) directions of the lattice and computed $f_s^{/\!/}$, the superfluid fraction tensor component along the longitudinal direction, using eq. (4.70):

$$f_s^{/\!/} = \frac{c_{/\!/}^2}{c_\perp^2}. \tag{5.27}$$

We also computed Leggett's upper bound along the longitudinal direction (which is saturated in this case) using the static density profile. As with the triangular lattice, we reconstructed the density using the first two harmonics, with periods of 4 µm and 2 µm respectively. These results appear in fig. 5.12 and show excellent agreement with the numerical prediction for both measurements.

Conclusion

In this chapter, we detailed our experimental investigation of the superfluid properties of a zero-temperature BEC subjected to an external periodic potential. We began by describing the experimental setup, highlighting the use of a DMD to generate a triangular lattice

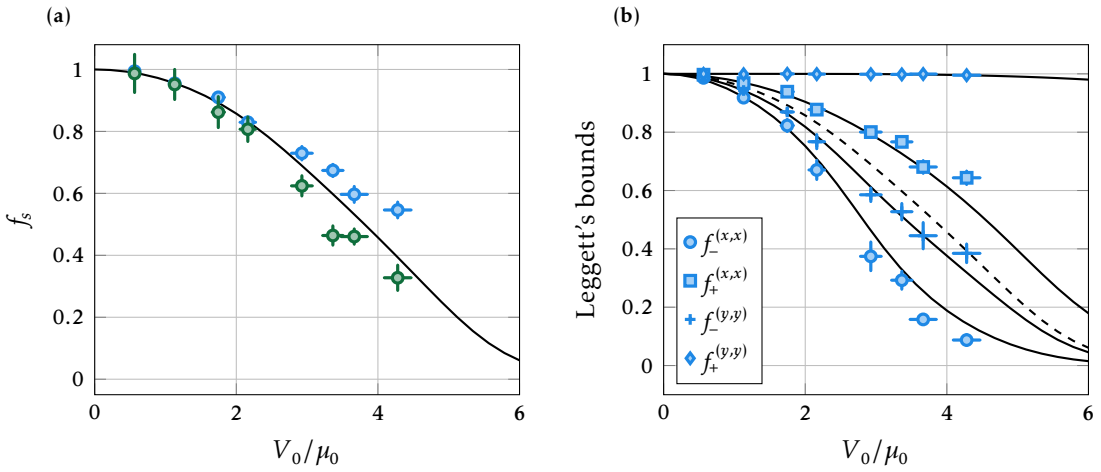

Figure 5.11: Measurements of superfluid fraction, Leggett's and Saslow's bounds for the triangular lattice. (a) Green points show measurements using the dynamic approach, computing f_s from speed of sound and compressibility using eq. (5.26). Blue points show measurements of Saslow's bound from static density profiles. The black solid line shows results from GPE simulations using twisted boundary conditions. (b) Blue points show Leggett's bounds computed from static density profiles; black solid lines show the corresponding bounds from GPE simulations. The black dotted line shows the superfluid fraction from GPE simulations.

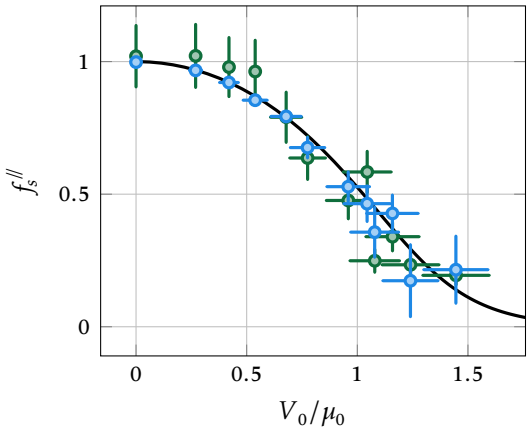

Figure 5.12: Superfluid fraction along the longitudinal direction for a one-dimensional sinusoidal lattice versus normalized potential depth. Green points show measurements from speed of sound; blue points show Leggett's upper bound calculated from static density profiles. The black curve shows predictions from GPE numerical simulations.

potential. We explained the necessity of implementing a feedback loop to correct the imperfections and ensure a homogeneous potential imprinted onto the atomic cloud.

Subsequently, we discussed the characterization of the system. We showed that the density profile of the BEC in the lattice can be decomposed into harmonics of the fundamental lattice structure. An essential part of our work involved calibrating both the depth of the optical potential and the spatial frequency response of our imaging system. This calibration was done for the first two harmonics of the triangular lattice.

The accurate calibration of the imaging system's frequency response is essential for reliably reconstructing the atomic density profile from absorption images. This reconstructed profile is then used to compute Saslow's and Leggett's bounds on the superfluid fraction. We demonstrated through numerical benchmarks that, within the range of potential depths explored experimentally, analyzing the first two density harmonics is sufficient to compute these bounds accurately.

Finally, we presented our experimental measurements. We described the methods used to determine the speed of sound and the compressibility of the modulated BEC. Combining these two dynamical measurements allowed us to compute the superfluid fraction for the triangular lattice geometry. We presented these results alongside the experimentally determined Saslow's and Leggett's bounds, showing good agreement with theoretical predictions based on the GPE. To conclude, we also presented results obtained previously for a one-dimensional sinusoidal lattice potential, where the superfluid fraction was determined using measurements of the speed of sound along two orthogonal directions.

Outlook As an outlook, two directions can be taken. In the short term, while the influence of disorder on the superfluid fraction has recently been studied theoretically [231, 232], it has yet to be explored experimentally. In the longer term, we are constructing a new experimental setup, largely similar to the one used for this work, but with a key improvement: a laser system capable of performing Rydberg excitations. This laser system will enable Rydberg dressing, a technique proposed as a way to realize supersolid states [271, 272]. Indeed, the effective interaction potential between Rydberg-dressed atoms closely resembles the soft-core interaction potential [273–276], which is known theoretically to lead to supersolid phases of matter [220, 247, 248, 264, 277, 278]. It would be interesting to explore the possibility of determining the superfluid fraction of such systems.

Conclusion

In this thesis, we have explored two phenomena using our experimental platform for producing and manipulating two-dimensional ^{87}Rb BECs: Bloch Oscillations of magnetic solitons, and superfluidity in spatially modulated systems.

In chapter 1, we described our experimental apparatus for creating and studying two-dimensional ^{87}Rb BECs. Dimensionality reduction is achieved by loading a 3D BEC into a single node of a vertical optical lattice. Atoms are confined in-plane by flat-bottom traps generated by shaping light with a DMD, offering high versatility in trap geometry, while arbitrary potential landscapes can be imprinted using a second DMD. We have control over the internal state of the atoms both globally using MW fields and in a spatially-resolved way using a pair of Raman beams. This comprehensive toolbox is essential for conducting the experiments presented in this thesis.

The first investigation presented in this thesis focused on BOs of magnetic solitons. In chapter 2, we established the theoretical framework and reviewed experimental realizations of matter-wave solitons in both single-component and two-component systems governed by the GPE. We then presented our experimental realization of a magnetic soliton at rest in a two-component mixture, which is the first realization in an immiscible mixture. In chapter 3, we extended our investigation to the dynamics of magnetic solitons under external forces. By measuring both the soliton's CoM position and the bath phase dynamics via matter-wave interferometry, we observed remarkable phenomena in two different geometries. In a segment geometry, we observed Bloch oscillations occurring without an external periodic potential. These oscillations were accompanied by π-phase jumps synchronized with the soliton's turning points. The oscillations stem from the periodicity of the soliton's energy with respect to its momentum, a general property of one-dimensional systems at the thermodynamic limit. We quantitatively confirmed the predicted inverse scaling of the oscillation period with the soliton atom number, thus revealing the collective nature of these oscillations. In a ring geometry, we observed more complex dynamics arising from the interplay between the oscillatory motion and the backflow current. This interaction leads to the pumping and depumping of quantized topological superfluid currents in the bath, which we directly observed through matter-wave interferometry. Looking forward, promising research directions include studying interactions and collisions between solitons, as well as exploring the few-body regime where mean-field descriptions break down.

The second study examined how density modulation reduces the superfluid fraction at zero temperature. In chapter 4, we reviewed the concepts of superfluidity and the superfluid fraction tensor, with particular attention to how broken translational invariance decreases superfluid fraction at zero temperature. This concept is especially relevant to the active research field of supersolids. We analyzed theoretical bounds on the superfluid fraction tensor in systems with broken translational invariance, specifically Leggett's

and Saslow's bounds, which can be computed from the system's density profile. For BECs described by the GPE, we demonstrated that Saslow's upper bound is saturated. This means the superfluid fraction is entirely determined by the density profile. We also established how, hydrodynamically, sound propagation measurements, combined with compressibility, provide experimental access to the superfluid fraction. Using GPE simulations, we numerically illustrated the behavior of the superfluid fraction as well as of Leggett's and Saslow's bounds for a BEC in different lattice geometries. In chapter 5, we experimentally investigated these theoretical predictions by measuring the superfluid properties of a BEC subjected to an external periodic potential. Using a DMD to generate a triangular lattice potential, we determined the superfluid fraction via measurements of the speed of sound and compressibility. A careful calibration of our imaging system enabled a reconstruction of density profiles with the accuracy necessary to compute Saslow's and Leggett's bounds. We also presented complementary results for a one-dimensional sinusoidal lattice, where we measured the superfluid fraction through speed of sound measurements along orthogonal directions. In both cases, we observed good agreement between the experimental results and GPE predictions for both the bounds and the superfluid fraction. We could extend this study in the short-term by investigating the influence of disorder on superfluidity. In the long-term, using a new experimental apparatus that is currently being built, we could potentially realize a supersolid through Rydberg dressing techniques and characterize its superfluid fraction.

Bibliography

[1] Bose. Plancks Gesetz und Lichtquantenhypothese. In: *Z. Physik* 26.1 (1 Dec. 1, 1924), pp. 178–181 (cit. on p. 1).

[2] A. Einstein. Quantentheorie Des Einatomigen Idealen Gases. In: *Sitzungsberichte/Physikalische Klasse, Preussische Akademie der Wissenschaften* 22 (1924), p. 261 (cit. on p. 1).

[3] A. Einstein. Quantentheorie Des Einatomigen Idealen Gases. II. In: *Sitzungsberichte/Physikalische Klasse, Preussische Akademie der Wissenschaften* 1 (1925), p. 3 (cit. on p. 1).

[4] A. Einstein. Zur Quantentheorie Des Idealen Gases. In: *Sitzungsberichte/Physikalische Klasse, Preussische Akademie der Wissenschaften* 3 (1925), p. 18 (cit. on p. 1).

[5] O. Penrose and L. Onsager. Bose-Einstein Condensation and Liquid Helium. In: *Phys. Rev.* 104.3 (Nov. 1, 1956), pp. 576–584 (cit. on p. 1).

[6] F. London. On the Bose-Einstein Condensation. In: *Phys. Rev.* 54.11 (Dec. 1, 1938), pp. 947–954 (cit. on pp. 1, 72).

[7] L. Landau. Theory of the Superfluidity of Helium II. In: *Phys. Rev.* 60.4 (Aug. 15, 1941), pp. 356–358 (cit. on pp. 1, 72, 86).

[8] P. Kapitza. Viscosity of Liquid Helium below the λ-Point. In: *Nature* 141.3558 (Jan. 1938), pp. 74–74. ISSN: 1476-4687 (cit. on pp. 1, 72).

[9] J. F. Allen and A. D. Misener. Flow of Liquid Helium II. In: *Nature* 141.3558 (Jan. 1938), pp. 75–75. ISSN: 1476-4687 (cit. on pp. 1, 72).

[10] T. R. Sosnick, W. M. Snow, et al. Momentum Distributions in Liquid ^{4}He. In: *EPL* 9.7 (Aug. 1, 1989), p. 707. ISSN: 0295-5075 (cit. on pp. 1, 72).

[11] W. M. Snow, Y. Wang, and P. E. Sokol. Density and Temperature Dependence of the Condensate Fraction in Liquid ^{4}He. In: *EPL* 19.5 (July 1, 1992), p. 403. ISSN: 0295-5075 (cit. on pp. 1, 72).

[12] D. D. Osheroff, R. C. Richardson, and D. M. Lee. Evidence for a New Phase of Solid ^{3}He. In: *Phys. Rev. Lett.* 28.14 (Apr. 3, 1972), pp. 885–888 (cit. on pp. 1, 72).

[13] J. M. Kosterlitz and D. J. Thouless. Long Range Order and Metastability in Two Dimensional Solids and Superfluids. (Application of Dislocation Theory). In: *J. Phys. C: Solid State Phys.* 5.11 (June 1972), p. L124. ISSN: 0022-3719 (cit. on p. 1).

[14] V. L. Berezinsky. Destruction of Long-range Order in One-dimensional and Two-dimensional Systems Possessing a Continuous Symmetry Group. II. Quantum Systems. In: *Sov. Phys. JETP* 34.3 (1972), p. 610 (cit. on p. 1).

[15] J. M. Kosterlitz. The Critical Properties of the Two-Dimensional Xy Model. In: *J. Phys. C: Solid State Phys.* 7.6 (Mar. 1974), p. 1046. ISSN: 0022-3719 (cit. on p. 1).

[16] D. J. Bishop and J. D. Reppy. Study of the Superfluid Transition in Two-Dimensional ^{4}He Films. In: *Phys. Rev. Lett.* 40.26 (June 26, 1978), pp. 1727–1730 (cit. on pp. 1, 72).

[17] R. Desbuquois, L. Chomaz, et al. Superfluid Behaviour of a Two-Dimensional Bose Gas. In: *Nature Phys* 8.9 (9 Sept. 2012), pp. 645–648. ISSN: 1745-2481 (cit. on p. 1).

[18] M. H. Anderson, J. R. Ensher, et al. Observation of Bose-Einstein Condensation in a Dilute Atomic Vapor. In: *Science* 269.5221 (July 14, 1995), pp. 198–201 (cit. on p. 1).

[19] K. B. Davis, M. .-. Mewes, et al. Bose-Einstein Condensation in a Gas of Sodium Atoms. In: *Phys. Rev. Lett.* 75.22 (Nov. 27, 1995), pp. 3969–3973 (cit. on p. 1).

[20] B. DeMarco and D. S. Jin. Onset of Fermi Degeneracy in a Trapped Atomic Gas. In: *Science* 285.5434 (Sept. 10, 1999), pp. 1703–1706 (cit. on p. 1).

[21] I. Bloch, J. Dalibard, and W. Zwerger. Many-Body Physics with Ultracold Gases. In: *Rev. Mod. Phys.* 80.3 (July 18, 2008), pp. 885–964 (cit. on p. 1).

[22] G. Modugno, G. Ferrari, et al. Bose-Einstein Condensation of Potassium Atoms by Sympathetic Cooling. In: *Science* 294.5545 (Nov. 9, 2001), pp. 1320–1322 (cit. on p. 1).

[23] G. Roati, F. Riboli, et al. Fermi-Bose Quantum Degenerate ^{40}K–^{87}Rb Mixture with Attractive Interaction. In: *Phys. Rev. Lett.* 89.15 (Sept. 23, 2002), p. 150403 (cit. on p. 1).

[24] M. Taglieber, A.-C. Voigt, et al. Quantum Degenerate Two-Species Fermi-Fermi Mixture Coexisting with a Bose-Einstein Condensate. In: *Phys. Rev. Lett.* 100.1 (Jan. 4, 2008), p. 010401 (cit. on p. 1).

[25] E. Wille, F. M. Spiegelhalder, et al. Exploring an Ultracold Fermi-Fermi Mixture: Interspecies Feshbach Resonances and Scattering Properties of ^{6}Li and ^{40}K. In: *Phys. Rev. Lett.* 100.5 (Feb. 5, 2008), p. 053201 (cit. on p. 1).

[26] L. D. Carr, D. DeMille, et al. Cold and Ultracold Molecules: Science, Technology and Applications. In: *New J. Phys.* 11.5 (May 2009), p. 055049. ISSN: 1367-2630 (cit. on p. 1).

[27] N. Bigagli, W. Yuan, et al. Observation of Bose–Einstein Condensation of Dipolar Molecules. In: *Nature* 631.8020 (July 2024), pp. 289–293. ISSN: 1476-4687 (cit. on p. 1).

[28] S. Inouye, M. R. Andrews, et al. Observation of Feshbach Resonances in a Bose–Einstein Condensate. In: *Nature* 392.6672 (Mar. 1998), pp. 151–154. ISSN: 1476-4687 (cit. on p. 1).

[29] C. Chin, R. Grimm, et al. Feshbach Resonances in Ultracold Gases. In: *Rev. Mod. Phys.* 82.2 (Apr. 29, 2010), pp. 1225–1286 (cit. on p. 1).

[30] P. Zupancic, P. M. Preiss, et al. Ultra-Precise Holographic Beam Shaping for Microscopic Quantum Control. In: *Opt. Express, OE* 24.13 (June 27, 2016), pp. 13881–13893. ISSN: 1094-4087 (cit. on p. 2).

[31] V. Boyer, R. M. Godun, et al. Dynamic Manipulation of Bose-Einstein Condensates with a Spatial Light Modulator. In: *Phys. Rev. A* 73.3 (Mar. 31, 2006), p. 031402 (cit. on p. 2).

[32] M. Greiner, O. Mandel, et al. Quantum Phase Transition from a Superfluid to a Mott Insulator in a Gas of Ultracold Atoms. In: *Nature* 415.6867 (Jan. 2002), pp. 39–44. ISSN: 1476-4687 (cit. on pp. 2, 76).

[33] R. Jördens, N. Strohmaier, et al. A Mott Insulator of Fermionic Atoms in an Optical Lattice. In: *Nature* 455.7210 (Sept. 2008), pp. 204–207. ISSN: 1476-4687 (cit. on p. 2).

[34] U. Schneider, L. Hackermüller, et al. Metallic and Insulating Phases of Repulsively Interacting Fermions in a 3D Optical Lattice. In: *Science* 322.5907 (Dec. 5, 2008), pp. 1520–1525 (cit. on p. 2).

[35] H.-J. Shao, Y.-X. Wang, et al. Antiferromagnetic Phase Transition in a 3D Fermionic Hubbard Model. In: *Nature* 632.8024 (Aug. 2024), pp. 267–272. ISSN: 1476-4687 (cit. on p. 2).

[36] T. Fukuhara, A. Kantian, et al. Quantum Dynamics of a Mobile Spin Impurity. In: *Nature Phys* 9.4 (Apr. 2013), pp. 235–241. ISSN: 1745-2481 (cit. on p. 2).

[37] S. Trotzky, P. Cheinet, et al. Time-Resolved Observation and Control of Superexchange Interactions with Ultracold Atoms in Optical Lattices. In: *Science* 319.5861 (Jan. 18, 2008), pp. 295–299 (cit. on p. 2).

[38] S. Nascimbène, Y.-A. Chen, et al. Experimental Realization of Plaquette Resonating Valence-Bond States with Ultracold Atoms in Optical Superlattices. In: *Phys. Rev. Lett.* 108.20 (May 14, 2012), p. 205301 (cit. on p. 2).

[39] M. Aidelsburger, M. Atala, et al. Realization of the Hofstadter Hamiltonian with Ultracold Atoms in Optical Lattices. In: *Phys. Rev. Lett.* 111.18 (Oct. 28, 2013), p. 185301 (cit. on p. 2).

[40] H. Miyake, G. A. Siviloglou, et al. Realizing the Harper Hamiltonian with Laser-Assisted Tunneling in Optical Lattices. In: *Phys. Rev. Lett.* 111.18 (Oct. 28, 2013), p. 185302 (cit. on p. 2).

[41] G. Jotzu, M. Messer, et al. Experimental Realization of the Topological Haldane Model with Ultracold Fermions. In: *Nature* 515.7526 (Nov. 2014), pp. 237–240. ISSN: 1476-4687 (cit. on p. 2).

[42] K. W. Madison, F. Chevy, et al. Vortex Formation in a Stirred Bose-Einstein Condensate. In: *Phys. Rev. Lett.* 84.5 (Jan. 31, 2000), pp. 806–809 (cit. on p. 2).

[43] J. R. Abo-Shaeer, C. Raman, et al. Observation of Vortex Lattices in Bose-Einstein Condensates. In: *Science* 292.5516 (Apr. 20, 2001), pp. 476–479 (cit. on p. 2).

[44] A. Aftalion, X. Blanc, and J. Dalibard. Vortex Patterns in a Fast Rotating Bose-Einstein Condensate. In: *Phys. Rev. A* 71.2 (Feb. 25, 2005), p. 023611 (cit. on p. 2).

[45] W. Zwerger. Basic Concepts and Some Current Directions in Ultracold Gases. Lecture notes. College de France, 2021 (cit. on pp. 2, 83).

[46] A. J. Leggett. Can a Solid Be "Superfluid"? In: *Phys. Rev. Lett.* 25.22 (Nov. 30, 1970), pp. 1543–1546 (cit. on pp. 2, 72, 76, 77).

[47] E. Kim and M. H. W. Chan. Probable Observation of a Supersolid Helium Phase. In: *Nature* 427.6971 (Jan. 2004), pp. 225–227. ISSN: 1476-4687 (cit. on p. 2).

[48] E. Kim and M. H. W. Chan. Observation of Superflow in Solid Helium. In: *Science* 305.5692 (Sept. 24, 2004), pp. 1941–1944 (cit. on p. 2).

[49] D. Y. Kim and M. H. W. Chan. Absence of Supersolidity in Solid Helium in Porous Vycor Glass. In: *Phys. Rev. Lett.* 109.15 (Oct. 8, 2012), p. 155301 (cit. on p. 2).

[50] J. Léonard, A. Morales, et al. Supersolid Formation in a Quantum Gas Breaking a Continuous Translational Symmetry. In: *Nature* 543.7643 (Mar. 2017), pp. 87–90. ISSN: 1476-4687 (cit. on pp. 2, 83).

[51] J. Léonard, A. Morales, et al. Monitoring and Manipulating Higgs and Goldstone Modes in a Supersolid Quantum Gas. In: *Science* 358.6369 (Dec. 15, 2017), pp. 1415–1418 (cit. on pp. 2, 83).

[52] J.-R. Li, J. Lee, et al. A Stripe Phase with Supersolid Properties in Spin–Orbit-Coupled Bose–Einstein Condensates. In: *Nature* 543.7643 (Mar. 2017), pp. 91–94. ISSN: 1476-4687 (cit. on pp. 2, 83).

[53] C. S. Chisholm, S. Hirthe, et al. *Probing Supersolidity through Excitations in a Spin-Orbit-Coupled Bose-Einstein Condensate*. Dec. 18, 2024. arXiv: 2412.13861 [cond-mat]. Pre-published (cit. on pp. 2, 83).

[54] N. Liebster, M. Sparn, et al. Supersolid-like Sound Modes in a Driven Quantum Gas. In: *Nat. Phys.* (June 2, 2025), pp. 1–7. ISSN: 1745-2481 (cit. on pp. 2, 83, 87).

[55] F. Böttcher, J.-N. Schmidt, et al. Transient Supersolid Properties in an Array of Dipolar Quantum Droplets. In: *Phys. Rev. X* 9.1 (Mar. 22, 2019), p. 011051 (cit. on pp. 2, 83).

[56] L. Tanzi, E. Lucioni, et al. Observation of a Dipolar Quantum Gas with Metastable Supersolid Properties. In: *Phys. Rev. Lett.* 122.13 (Apr. 3, 2019), p. 130405 (cit. on pp. 2, 83, 87).

[57] L. Chomaz, D. Petter, et al. Long-Lived and Transient Supersolid Behaviors in Dipolar Quantum Gases. In: *Phys. Rev. X* 9.2 (Apr. 19, 2019), p. 021012 (cit. on pp. 2, 83).

[58] F. Bloch. Über die Quantenmechanik der Elektronen in Kristallgittern. In: *Z. Physik* 52.7 (July 1, 1929), pp. 555–600. ISSN: 0044-3328 (cit. on pp. 2, 50).

[59] C. Zener and R. H. Fowler. A Theory of the Electrical Breakdown of Solid Dielectrics. In: *Proceedings of the Royal Society of London. Series A, Containing Papers of a Mathematical and Physical Character* 145.855 (July 2, 1934), pp. 523–529 (cit. on pp. 2, 50).

[60] K. Leo, P. H. Bolivar, et al. Observation of Bloch Oscillations in a Semiconductor Superlattice. In: *Solid State Communications* 84.10 (Dec. 1, 1992), pp. 943–946. ISSN: 0038-1098 (cit. on p. 2).

[61] J. Feldmann, K. Leo, et al. Optical Investigation of Bloch Oscillations in a Semiconductor Superlattice. In: *Phys. Rev. B* 46.11 (Sept. 15, 1992), pp. 7252–7255 (cit. on pp. 2, 50).

[62] C. Waschke, H. G. Roskos, et al. Coherent Submillimeter-Wave Emission from Bloch Oscillations in a Semiconductor Superlattice. In: *Phys. Rev. Lett.* 70.21 (May 24, 1993), pp. 3319–3322 (cit. on p. 2).

[63] M. Ben Dahan, E. Peik, et al. Bloch Oscillations of Atoms in an Optical Potential. In: *Phys. Rev. Lett.* 76.24 (June 10, 1996), pp. 4508–4511. ISSN: 0031-9007, 1079-7114 (cit. on pp. 2, 50).

[64] S. R. Wilkinson, C. F. Bharucha, et al. Observation of Atomic Wannier-Stark Ladders in an Accelerating Optical Potential. In: *Phys. Rev. Lett.* 76.24 (June 10, 1996), pp. 4512–4515 (cit. on pp. 2, 50).

[65] P. Cladé, S. Guellati-Khélifa, et al. A Promising Method for the Measurement Ofthe Local Acceleration of Gravity Using Bloch Oscillations of Ultracold Atoms in a Vertical Standing Wave. In: *EPL* 71.5 (Aug. 5, 2005), p. 730. ISSN: 0295-5075 (cit. on p. 2).

[66] G. Ferrari, N. Poli, et al. Long-Lived Bloch Oscillations with Bosonic Sr Atoms and Application to Gravity Measurement at the Micrometer Scale. In: *Phys. Rev. Lett.* 97.6 (Aug. 9, 2006), p. 060402 (cit. on pp. 2, 50).

[67] P. Wolf, P. Lemonde, et al. From Optical Lattice Clocks to the Measurement of Forces in the Casimir Regime. In: *Phys. Rev. A* 75.6 (June 8, 2007), p. 063608 (cit. on p. 2).

[68] F. Sorrentino, A. Alberti, et al. Quantum Sensor for Atom-Surface Interactions below 10 μm. In: *Phys. Rev. A* 79.1 (Jan. 9, 2009), p. 013409 (cit. on p. 2).

[69] Q. Beaufils, G. Tackmann, et al. Laser Controlled Tunneling in a Vertical Optical Lattice. In: *Phys. Rev. Lett.* 106.21 (May 27, 2011), p. 213002 (cit. on p. 2).

[70] V. Xu, M. Jaffe, et al. Probing Gravity by Holding Atoms for 20 Seconds. In: *Science* 366.6466 (Nov. 8, 2019), pp. 745–749 (cit. on pp. 2, 50).

[71] G. M. Tino. Testing Gravity with Cold Atom Interferometry: Results and Prospects. In: *Quantum Sci. Technol.* 6.2 (Mar. 2021), p. 024014. ISSN: 2058-9565 (cit. on p. 2).

[72] R. H. Parker, C. Yu, et al. Measurement of the Fine-Structure Constant as a Test of the Standard Model. In: *Science* 360.6385 (Apr. 13, 2018), pp. 191–195 (cit. on pp. 2, 50).

[73] L. Morel, Z. Yao, et al. Determination of the Fine-Structure Constant with an Accuracy of 81 Parts per Trillion. In: *Nature* 588.7836 (Dec. 2020), pp. 61–65. ISSN: 1476-4687 (cit. on pp. 2, 50).

[74] H. M. Price and N. R. Cooper. Mapping the Berry Curvature from Semiclassical Dynamics in Optical Lattices. In: *Phys. Rev. A* 85.3 (Mar. 15, 2012), p. 033620 (cit. on pp. 2, 50).

[75] M. Aidelsburger, M. Lohse, et al. Measuring the Chern Number of Hofstadter Bands with Ultracold Bosonic Atoms. In: *Nature Phys* 11.2 (Feb. 2015), pp. 162–166. ISSN: 1745-2481 (cit. on pp. 2, 50).

[76] F. Bloch. Superfluidity in a Ring. In: *Phys. Rev. A* 7.6 (June 1, 1973), pp. 2187–2191 (cit. on pp. 3, 63).

[77] F. Meinert, M. Knap, et al. Bloch Oscillations in the Absence of a Lattice. In: *Science* 356.6341 (June 2, 2017), pp. 945–948 (cit. on pp. 3, 60, 65).

[78] P. G. Drazin and R. S. Johnson. *Solitons: An Introduction*. 2nd ed. Cambridge Texts in Applied Mathematics. Cambridge: Cambridge University Press, 1989. ISBN: 978-0-521-33655-0 (cit. on pp. 3, 19).

[79] M. Peyrard and T. Dauxois. *Physique des solitons*. Les Ulis: EDP Sciences, 2014. 425 pp. ISBN: 978-2-7598-0288-3 978-2-86883-732-5 (cit. on pp. 3, 18).

[80] L. P. Pitaevskii and S. Stringari. *Bose-Einstein Condensation and Superfluidity*. First edition. International Series of Monographs on Physics 164. Oxford, United Kingdom: Oxford University Press, 2016. 553 pp. ISBN: 978-0-19-875888-4 978-0-19-882443-5 (cit. on pp. 3, 21, 23).

[81] L. Corman. "The Two-Dimensional Bose Gas in Box Potentials". These de doctorat. Paris Sciences et Lettres (ComUE), June 2, 2016 (cit. on p. 5).

[82] J.-L. Ville. "Quantum Gases in Box Potentials : Sound and Light in Bosonic Flatland". PhD thesis. Université Paris sciences et lettres, Apr. 13, 2018 (cit. on p. 5).

[83] R. Saint-Jalm. "Exploring Two-Dimensional Physics with Bose Gases in Box Potentials : Phase Ordering and Dynamical Symmetry". These de doctorat. Paris Sciences et Lettres (ComUE), Oct. 3, 2019 (cit. on pp. 5, 12).

[84] B. Bakkali-Hassani. "Testing Scale Invariance in a Two-Dimensional Bose Gas : Preparation and Characterization of Solitary Waves". These de doctorat. Sorbonne université, Dec. 10, 2021 (cit. on pp. 5, 25).

[85] C. Maury. "Probing Few and Many-Body Physics in a Planar Bose Gas : Atom-dimer Interactions and Zero-Temperature Superfluid Fraction". These de doctorat. Sorbonne université, Feb. 20, 2023 (cit. on pp. 5, 90).

[86] G. Chauveau. "Exploring the Dynamics of Zero-Temperature Bose Gases : Measurement of the Superfluid Fraction and Observation of Bloch-like Oscillations of a Magnetic Soliton". PhD thesis. Sorbonne Université, Mar. 26, 2024 (cit. on pp. 5, 14, 49, 90, 103).

[87] N. D. Mermin and H. Wagner. Absence of Ferromagnetism or Antiferromagnetism in One- or Two-Dimensional Isotropic Heisenberg Models. In: *Phys. Rev. Lett.* 17.22 (Nov. 28, 1966), pp. 1133–1136 (cit. on p. 6).

[88] P. C. Hohenberg. Existence of Long-Range Order in One and Two Dimensions. In: *Phys. Rev.* 158.2 (June 10, 1967), pp. 383–386 (cit. on p. 6).

[89] Z. Hadzibabic and J. Dalibard. Two-Dimensional Bose Fluids: An Atomic Physics Perspective. In: *La Rivista del Nuovo Cimento* 34.6 (June 7, 2011), pp. 389–434. ISSN: 0393697X, 0393697X. arXiv: 0912.1490 [cond-mat] (cit. on p. 6).

[90] R. Grimm, M. Weidemüller, and Y. B. Ovchinnikov. "Optical Dipole Traps for Neutral Atoms". In: *Advances In Atomic, Molecular, and Optical Physics*. Ed. by B. Bederson and H. Walther. Vol. 42. Academic Press, Jan. 1, 2000, pp. 95–170 (cit. on p. 7).

[91] J. L. Ville, T. Bienaimé, et al. Loading and Compression of a Single Two-Dimensional Bose Gas in an Optical Accordion. In: *Phys. Rev. A* 95.1 (2017) (cit. on p. 9).

[92] R. Floyd and L. Steinberg. An Adaptive Algorithm for Spatial Greyscale. In: *Proceedings of the Society for Information Display* 17.2 (1976), pp. 75–77 (cit. on p. 11).

[93] C. Dorrer and J. D. Zuegel. Design and Analysis of Binary Beam Shapers Using Error Diffusion. In: *J. Opt. Soc. Am. B, JOSAB* 24.6 (June 1, 2007), pp. 1268–1275. ISSN: 1520-8540 (cit. on p. 11).

[94] A. Ramanathan, S. R. Muniz, et al. Partial-Transfer Absorption Imaging: A Versatile Technique for Optimal Imaging of Ultracold Gases. In: *Review of Scientific Instruments* 83.8 (Aug. 30, 2012), p. 083119. ISSN: 0034-6748 (cit. on p. 11).

[95] E. A. Kuznetsov. On Solitons in Parametrically Unstable Plasma. In: *Doklady Akademii Nauk SSSR*, 236.3 (June 23, 1977), pp. 575–577 (cit. on p. 18).

[96] N. N. Akhmediev, V. M. Eleonskii, and N. E. Kulagin. Exact First-Order Solutions of the Nonlinear Schrödinger Equation. In: *Theor Math Phys* 72.2 (2 Aug. 1, 1987), pp. 809–818. ISSN: 1573-9333 (cit. on p. 18).

[97] D. J. Korteweg and G. de Vries. On the Change of Form of Long Waves Advancing in a Rectangular Canal, and on a New Type of Long Stationary Waves. In: *The London, Edinburgh, and Dublin Philosophical Magazine and Journal of Science* 39.240 (May 1, 1895), pp. 422–443. ISSN: 1941-5982 (cit. on p. 18).

[98] L. D. Landau and E. Lifshitz. On the Theory of the Dispersion of Magnetic Permeability in Ferromagnetic Bodies. In: *Phys. Z. Sowjetunion* 8.153 (1935), pp. 101–114 (cit. on pp. 19, 31, 73).

[99] A. M. Kosevich, B. A. Ivanov, and A. S. Kovalev. Magnetic Solitons. In: *Physics Reports* 194.3 (Oct. 1, 1990), pp. 117–238. ISSN: 0370-1573 (cit. on pp. 19, 35).

[100] J. Rubinstein. Sine-Gordon Equation. In: *Journal of Mathematical Physics* 11.1 (Jan. 1, 1970), pp. 258–266. ISSN: 0022-2488 (cit. on p. 19).

[101] G. L. Lamb. Analytical Descriptions of Ultrashort Optical Pulse Propagation in a Resonant Medium. In: *Rev. Mod. Phys.* 43.2 (Apr. 1, 1971), pp. 99–124 (cit. on p. 19).

[102] M. Remoissenet. *Waves Called Solitons: Concepts and Experiments*. 3rd ed. Advanced Texts in Physics Ser. Berlin, Heidelberg: Springer Berlin / Heidelberg, 2003. 1 p. ISBN: 978-3-662-03790-4 (cit. on p. 19).

[103] V. Zakharov and A. Shabat. Exact Theory of Two-Dimensional Self-Focusing and One- Dimensional Self-Modulation of Waves in Nonlinear Media. In: *Journal of Experimental and Theoretical Physics* 34.1 (Jan. 1972), p. 62 (cit. on p. 19).

[104] M. J. Ablowitz, D. J. Kaup, et al. The Inverse Scattering Transform-Fourier Analysis for Nonlinear Problems. In: *Studies in Applied Mathematics* 53.4 (1974), pp. 249–315. ISSN: 1467-9590 (cit. on p. 19).

[105] T. Tao. Why Are Solitons Stable? In: *Bull. Amer. Math. Soc.* 46.1 (2009), pp. 1–33. ISSN: 0273-0979, 1088-9485 (cit. on p. 19).

[106] A. Hasegawa and F. Tappert. Transmission of Stationary Nonlinear Optical Pulses in Dispersive Dielectric Fibers. I. Anomalous Dispersion. In: *Applied Physics Letters* 23.3 (Aug. 1, 1973), pp. 142–144. ISSN: 0003-6951 (cit. on p. 19).

[107] L. F. Mollenauer, R. H. Stolen, and J. P. Gordon. Experimental Observation of Picosecond Pulse Narrowing and Solitons in Optical Fibers. In: *Phys. Rev. Lett.* 45.13 (Sept. 29, 1980), pp. 1095–1098 (cit. on p. 19).

[108] L. F. Mollenauer and K. Smith. Demonstration of Soliton Transmission over More than 4000 Km in Fiber with Loss Periodically Compensated by Raman Gain. In: *Opt. Lett., OL* 13.8 (Aug. 1, 1988), pp. 675–677. ISSN: 1539-4794 (cit. on p. 19).

[109] D. R. Solli, C. Ropers, et al. Optical Rogue Waves. In: *Nature* 450.7172 (Dec. 2007), pp. 1054–1057. ISSN: 1476-4687 (cit. on p. 19).

[110] B. Kibler, J. Fatome, et al. The Peregrine Soliton in Nonlinear Fibre Optics. In: *Nature Phys* 6.10 (Oct. 2010), pp. 790–795. ISSN: 1745-2481 (cit. on p. 19).

[111] B. Kibler, J. Fatome, et al. Observation of Kuznetsov-Ma Soliton Dynamics in Optical Fibre. In: *Sci Rep* 2.1 (June 18, 2012), p. 463. ISSN: 2045-2322 (cit. on p. 19).

[112] F. Copie, P. Suret, and S. Randoux. Space–Time Observation of the Dynamics of Soliton Collisions in a Recirculating Optical Fiber Loop. In: *Optics Communications* 545 (Oct. 15, 2023), p. 129647. ISSN: 0030-4018 (cit. on p. 19).

[113] M. Ishikawa and H. Takayama. Solitons in a One-Dimensional Bose System with the Repulsive Delta-Function Interaction. In: *Journal of the Physical Society of Japan* 49.4 (1980), pp. 1242–1246 (cit. on p. 19).

[114] E. Kaminishi, T. Mori, and S. Miyashita. Construction of Quantum Dark Soliton in One-Dimensional Bose Gas. In: *J. Phys. B: At. Mol. Opt. Phys.* 53.9 (Apr. 2020), p. 095302. ISSN: 0953-4075 (cit. on p. 19).

[115] Y. Castin and C. Herzog. Bose–Einstein Condensates in Symmetry Breaking States. In: *Comptes Rendus de l'Académie des Sciences - Series IV - Physics* 2.3 (Apr. 1, 2001), pp. 419–443. ISSN: 1296-2147 (cit. on p. 20).

[116] L. Khaykovich, F. Schreck, et al. Formation of a Matter-Wave Bright Soliton. In: *Science* 296.5571 (May 17, 2002), pp. 1290–1293 (cit. on p. 20).

[117] K. E. Strecker, G. B. Partridge, et al. Formation and Propagation of Matter-Wave Soliton Trains. In: *Nature* 417.6885 (May 2002), pp. 150–153. ISSN: 1476-4687 (cit. on p. 20).

[118] A. L. Marchant, T. P. Billam, et al. Controlled Formation and Reflection of a Bright Solitary Matter-Wave. In: *Nat Commun* 4.1 (May 14, 2013), p. 1865. ISSN: 2041-1723 (cit. on p. 20).

[119] P. Medley, M. A. Minar, et al. Evaporative Production of Bright Atomic Solitons. In: *Phys. Rev. Lett.* 112.6 (Feb. 14, 2014), p. 060401 (cit. on p. 20).

[120] G. D. McDonald, C. C. N. Kuhn, et al. Bright Solitonic Matter-Wave Interferometer. In: *Phys. Rev. Lett.* 113.1 (July 2, 2014), p. 013002 (cit. on p. 20).

[121] J. H. V. Nguyen, P. Dyke, et al. Collisions of Matter-Wave Solitons. In: *Nature Phys* 10.12 (Dec. 2014), pp. 918–922. ISSN: 1745-2481 (cit. on pp. 20, 46, 47).

[122] A. L. Marchant, T. P. Billam, et al. Quantum Reflection of Bright Solitary Matter Waves from a Narrow Attractive Potential. In: *Phys. Rev. A* 93.2 (Feb. 3, 2016), p. 021604 (cit. on pp. 20, 46).

[123] J. H. V. Nguyen, D. Luo, and R. G. Hulet. Formation of Matter-Wave Soliton Trains by Modulational Instability. In: *Science* 356.6336 (Apr. 28, 2017), pp. 422–426 (cit. on p. 20).

[124] T. Mežnaršič, T. Arh, et al. Cesium Bright Matter-Wave Solitons and Soliton Trains. In: *Phys. Rev. A* 99.3 (Mar. 29, 2019), p. 033625 (cit. on pp. 20, 46, 47).

[125] A. Di Carli, C. D. Colquhoun, et al. Excitation Modes of Bright Matter-Wave Solitons. In: *Phys. Rev. Lett.* 123.12 (Sept. 17, 2019), p. 123602 (cit. on p. 20).

[126] O. J. Wales, A. Rakonjac, et al. Splitting and Recombination of Bright-Solitary-Matter Waves. In: *Commun Phys* 3.1 (Mar. 13, 2020), pp. 1–9. ISSN: 2399-3650 (cit. on p. 20).

[127] D. Luo, Y. Jin, et al. Creation and Characterization of Matter-Wave Breathers. In: *Phys. Rev. Lett.* 125.18 (Oct. 30, 2020), p. 183902 (cit. on p. 20).

[128] N. G. Parker, S. L. Cornish, et al. Bright Solitary Waves and Trapped Solutions in Bose–Einstein Condensates with Attractive Interactions. In: *J. Phys. B: At. Mol. Opt. Phys.* 40.15 (July 2007), p. 3127. ISSN: 0953-4075 (cit. on pp. 20, 47).

[129] S. L. Cornish, S. T. Thompson, and C. E. Wieman. Formation of Bright Matter-Wave Solitons during the Collapse of Attractive Bose-Einstein Condensates. In: *Phys. Rev. Lett.* 96.17 (May 3, 2006), p. 170401 (cit. on pp. 20, 46).

[130] L. Khaykovich and B. A. Malomed. Deviation from One Dimensionality in Stationary Properties and Collisional Dynamics of Matter-Wave Solitons. In: *Phys. Rev. A* 74.2 (Aug. 16, 2006), p. 023607 (cit. on pp. 20, 47).

[131] J. Satsuma and N. Yajima. B. Initial Value Problems of One-Dimensional Self-Modulation of Nonlinear Waves in Dispersive Media. In: *Progress of Theoretical Physics Supplement* 55 (Jan. 1, 1974), pp. 284–306. ISSN: 0375-9687 (cit. on p. 20).

[132] B. Eiermann, Th. Anker, et al. Bright Bose-Einstein Gap Solitons of Atoms with Repulsive Interaction. In: *Phys. Rev. Lett.* 92.23 (June 8, 2004), p. 230401 (cit. on p. 21).

[133] T. Tsuzuki. Nonlinear Waves in the Pitaevskii-Gross Equation. In: *J Low Temp Phys* 4.4 (4 Apr. 1, 1971), pp. 441–457. ISSN: 1573-7357 (cit. on p. 21).

[134] S. Burger, K. Bongs, et al. Dark Solitons in Bose-Einstein Condensates. In: *Phys. Rev. Lett.* 83.25 (Dec. 20, 1999), pp. 5198–5201 (cit. on p. 22).

[135] J. Denschlag, J. E. Simsarian, et al. Generating Solitons by Phase Engineering of a Bose-Einstein Condensate. In: *Science* 287.5450 (Jan. 7, 2000), pp. 97–101 (cit. on p. 22).

[136] C. Becker, S. Stellmer, et al. Oscillations and Interactions of Dark and Dark–Bright Solitons in Bose–Einstein Condensates. In: *Nature Phys* 4.6 (June 2008), pp. 496–501. ISSN: 1745-2481 (cit. on pp. 22, 30, 47).

[137] S. Stellmer, C. Becker, et al. Collisions of Dark Solitons in Elongated Bose-Einstein Condensates. In: *Phys. Rev. Lett.* 101.12 (Sept. 19, 2008), p. 120406 (cit. on pp. 22, 47).

[138] B. Wu, J. Liu, and Q. Niu. Controlled Generation of Dark Solitons with Phase Imprinting. In: *Phys. Rev. Lett.* 88.3 (Jan. 2, 2002), p. 034101 (cit. on p. 22).

[139] A. R. Fritsch, M. Lu, et al. Creating Solitons with Controllable and Near-Zero Velocity in Bose-Einstein Condensates. In: *Phys. Rev. A* 101.5 (May 20, 2020), p. 053629 (cit. on pp. 22, 41, 47).

[140] T. Yefsah, A. T. Sommer, et al. Heavy Solitons in a Fermionic Superfluid. In: *Nature* 499.7459 (July 2013), pp. 426–430. ISSN: 1476-4687 (cit. on pp. 22, 47).

[141] L. D. Carr, J. Brand, et al. Dark-Soliton Creation in Bose-Einstein Condensates. In: *Phys. Rev. A* 63.5 (Apr. 9, 2001), p. 051601 (cit. on p. 22).

[142] A. Weller, J. P. Ronzheimer, et al. Experimental Observation of Oscillating and Interacting Matter Wave Dark Solitons. In: *Phys. Rev. Lett.* 101.13 (Sept. 22, 2008), p. 130401 (cit. on pp. 22, 47).

[143] I. Shomroni, E. Lahoud, et al. Evidence for an Oscillating Soliton/Vortex Ring by Density Engineering of a Bose–Einstein Condensate. In: *Nature Phys* 5.3 (Mar. 2009), pp. 193–197. ISSN: 1745-2481 (cit. on p. 22).

[144] J. J. Chang, P. Engels, and M. A. Hoefer. Formation of Dispersive Shock Waves by Merging and Splitting Bose-Einstein Condensates. In: *Phys. Rev. Lett.* 101.17 (Oct. 23, 2008), p. 170404 (cit. on p. 22).

[145] W. H. Zurek. Causality in Condensates: Gray Solitons as Relics of BEC Formation. In: *Phys. Rev. Lett.* 102.10 (Mar. 12, 2009), p. 105702 (cit. on p. 22).

[146] G. Lamporesi, S. Donadello, et al. Spontaneous Creation of Kibble–Zurek Solitons in a Bose–Einstein Condensate. In: *Nature Phys* 9.10 (Oct. 2013), pp. 656–660. ISSN: 1745-2481 (cit. on p. 22).

[147] S. I. Shevchenko. Quasi-One-Dimensional Superfluidity in Bose Systems. In: *Soviet Journal Low Temperature Physics* 14.10 (Oct. 1, 1988), pp. 553–562. ISSN: 0360-0335 (cit. on p. 23).

[148] L. P. Pitaevskii. On the Momentum of Solitons and Vortex Rings in a Superfluid. In: *J. Exp. Theor. Phys.* 119.6 (Dec. 1, 2014), pp. 1097–1101. ISSN: 1090-6509 (cit. on pp. 23, 38).

[149] L. P. Pitaevskii. Dynamics of Solitary Waves in Ultracold Gases in Terms of Observable Quantities. In: *Phys.-Usp.* 59.10 (Oct. 1, 2016), p. 1028. ISSN: 1063-7869 (cit. on p. 24).

[150] E. Timmermans. Phase Separation of Bose-Einstein Condensates. In: *Phys. Rev. Lett.* 81.26 (Dec. 28, 1998), pp. 5718–5721 (cit. on p. 25).

[151] S. V. Manakov. On the Theory of Two-Dimensional Stationary Self-Focusing of Electromagnetic Waves. In: *Zhurnal Eksperimentalnoi i Teoreticheskoi Fiziki* 65 (Aug. 1, 1973), pp. 505–516. ISSN: 0044-4510 (cit. on p. 25).

[152] B. Bakkali-Hassani, C. Maury, et al. Realization of a Townes Soliton in a Two-Component Planar Bose Gas. In: *Phys. Rev. Lett.* 127.2 (July 9, 2021), p. 023603 (cit. on pp. 25, 26, 41).

[153] S. Trillo, S. Wabnitz, et al. Optical Solitary Waves Induced by Cross-Phase Modulation. In: *Opt. Lett., OL* 13.10 (Oct. 1, 1988), pp. 871–873. ISSN: 1539-4794 (cit. on p. 26).

[154] Th. Busch and J. R. Anglin. Dark-Bright Solitons in Inhomogeneous Bose-Einstein Condensates. In: *Phys. Rev. Lett.* 87.1 (June 15, 2001), p. 010401 (cit. on pp. 26, 28, 46, 47).

[155] Q.-H. Park and H. J. Shin. Systematic Construction of Multicomponent Optical Solitons. In: *Phys. Rev. E* 61.3 (Mar. 1, 2000), pp. 3093–3106 (cit. on p. 28).

[156] P. G. Kevrekidis, D. J. Frantzeskakis, and R. Carretero-González. "Chapter 2: The One-Dimensional Case". In: *The Defocusing Nonlinear Schrödinger Equation*. Other Titles in Applied Mathematics. Society for Industrial and Applied Mathematics, Mar. 8, 2015, pp. 17–156. ISBN: 978-1-61197-393-8 (cit. on p. 28).

[157] A. P. Sheppard and Y. S. Kivshar. Polarized Dark Solitons in Isotropic Kerr Media. In: *Phys. Rev. E* 55.4 (Apr. 1, 1997), pp. 4773–4782 (cit. on p. 28).

[158] N. Mao and L.-C. Zhao. Exact Analytical Soliton Solutions of N-Component Coupled Nonlinear Schr\"odinger Equations with Arbitrary Nonlinear Parameters. In: *Phys. Rev. E* 106.6 (Dec. 14, 2022), p. 064206 (cit. on pp. 28, 30).

[159] L.-C. Zhao, W. Wang, et al. Spin Soliton with a Negative-Positive Mass Transition. In: *Phys. Rev. A* 101.4 (Apr. 28, 2020), p. 043621 (cit. on pp. 30, 63).

[160] P. G. Kevrekidis, H. E. Nistazakis, et al. Families of Matter-Waves in Two-Component Bose-Einstein Condensates. In: *Eur. Phys. J. D* 28.2 (2 Feb. 1, 2004), pp. 181–185. ISSN: 1434-6079 (cit. on p. 30).

[161] B. P. Anderson, P. C. Haljan, et al. Watching Dark Solitons Decay into Vortex Rings in a Bose-Einstein Condensate. In: *Phys. Rev. Lett.* 86.14 (Apr. 2, 2001), pp. 2926–2929 (cit. on p. 30).

[162] C. Hamner, J. J. Chang, et al. Generation of Dark-Bright Soliton Trains in Superfluid-Superfluid Counterflow. In: *Phys. Rev. Lett.* 106.6 (Feb. 11, 2011), p. 065302 (cit. on p. 31).

[163] M. A. Hoefer, J. J. Chang, et al. Dark-Dark Solitons and Modulational Instability in Miscible Two-Component Bose-Einstein Condensates. In: *Phys. Rev. A* 84.4 (Oct. 14, 2011), p. 041605 (cit. on p. 31).

[164] F. Rabec, G. Chauveau, et al. *Bloch Oscillations of a Soliton in a 1D Quantum Fluid*. Dec. 5, 2024. arXiv: 2412.04355 [cond-mat]. Pre-published (cit. on pp. 31, 46).

[165] L. D. Landau, E. M. Lifshitz, and L. P. Pitaevskii. *Statistical Physics, Part 2*. Vol. 9. Course of Theoretical Physics. 1980 (cit. on p. 31).

[166] T. Congy, A. Kamchatnov, and N. Pavloff. Dispersive Hydrodynamics of Nonlinear Polarization Waves in Two-Component Bose-Einstein Condensates. In: *SciPost Physics* 1.1 (Oct. 25, 2016), p. 006. ISSN: 2542-4653 (cit. on pp. 32, 33).

[167] C. Qu, L. P. Pitaevskii, and S. Stringari. Magnetic Solitons in a Binary Bose-Einstein Condensate. In: *Phys. Rev. Lett.* 116.16 (Apr. 20, 2016), p. 160402 (cit. on pp. 32, 34).

[168] S. K. Ivanov, A. M. Kamchatnov, et al. Solution of the Riemann Problem for Polarization Waves in a Two-Component Bose-Einstein Condensate. In: *Phys. Rev. E* 96.6 (Dec. 11, 2017), p. 062202 (cit. on p. 33).

[169] S. Bresolin, A. Roy, et al. Oscillating Solitons and Ac Josephson Effect in Ferromagnetic Bose-Bose Mixtures. In: *Phys. Rev. Lett.* 130.22 (May 31, 2023), p. 220403 (cit. on pp. 33, 34, 39, 51, 52).

[170] B. A. Ivanov and A. M. Kosevich. Bound States of a Large Number of Magnons in a Ferromagnet with a Single-Ion Anisotropy. In: *Soviet Journal of Experimental and Theoretical Physics* 45 (1977), p. 1050 (cit. on pp. 34, 39).

[171] K. A. Long and A. R. Bishop. Nonlinear Excitations in Classical Ferromagnetic Chains. In: *J. Phys. A: Math. Gen.* 12.8 (Aug. 1979), p. 1325. ISSN: 0305-4470 (cit. on pp. 34, 39).

[172] A. Farolfi, D. Trypogeorgos, et al. Observation of Magnetic Solitons in Two-Component Bose-Einstein Condensates. In: *Phys. Rev. Lett.* 125.3 (July 15, 2020), p. 030401 (cit. on p. 34).

[173] E. G. M. van Kempen, S. J. J. M. F. Kokkelmans, et al. Interisotope Determination of Ultracold Rubidium Interactions from Three High-Precision Experiments. In: *Phys. Rev. Lett.* 88.9 (Feb. 14, 2002), p. 093201 (cit. on p. 41).

[174] Y.-Q. Zou, B. Bakkali-Hassani, et al. Magnetic Dipolar Interaction between Hyperfine Clock States in a Planar Alkali Bose Gas. In: *Phys. Rev. Lett.* 125.23 (Dec. 2, 2020), p. 233604 (cit. on p. 41).

[175] S. De, D. L. Campbell, et al. Quenched Binary Bose-Einstein Condensates: Spin-domain Formation and Coarsening. In: *Phys. Rev. A* 89.3 (Mar. 25, 2014), p. 033631 (cit. on p. 41).

[176] E. H. Lieb and W. Liniger. Exact Analysis of an Interacting Bose Gas. I. The General Solution and the Ground State. In: *Phys. Rev.* 130.4 (May 15, 1963), pp. 1605–1616 (cit. on p. 41).

[177] V. V. Konotop and L. Pitaevskii. Landau Dynamics of a Grey Soliton in a Trapped Condensate. In: *Phys. Rev. Lett.* 93.24 (Dec. 7, 2004), p. 240403 (cit. on p. 46).

[178] G. C. Katsimiga, G. M. Koutentakis, et al. Dark–Bright Soliton Dynamics beyond the Mean-Field Approximation. In: *New J. Phys.* 19.7 (July 2017), p. 073004. ISSN: 1367-2630 (cit. on p. 47).

[179] G. C. Katsimiga, J. Stockhofe, et al. Dark-Bright Soliton Interactions beyond the Integrable Limit. In: *Phys. Rev. A* 95.1 (Jan. 20, 2017), p. 013621 (cit. on p. 47).

[180] G. C. Katsimiga, P. G. Kevrekidis, et al. Dark-Bright Soliton Pairs: Bifurcations and Collisions. In: *Phys. Rev. A* 97.4 (Apr. 23, 2018), p. 043623 (cit. on p. 47).

[181] A. M. Kosevich, V. V. Gann, et al. Magnetic Soliton Motion in a Nonuniform Magnetic Field. In: *J. Exp. Theor. Phys.* 87.2 (Aug. 1, 1998), pp. 401–407. ISSN: 1090-6509 (cit. on p. 48).

[182] Z. A. Geiger, K. M. Fujiwara, et al. Observation and Uses of Position-Space Bloch Oscillations in an Ultracold Gas. In: *Phys. Rev. Lett.* 120.21 (May 24, 2018), p. 213201 (cit. on p. 50).

[183] T. Pertsch, P. Dannberg, et al. Optical Bloch Oscillations in Temperature Tuned Waveguide Arrays. In: *Phys. Rev. Lett.* 83.23 (Dec. 6, 1999), pp. 4752–4755 (cit. on p. 50).

[184] R. Morandotti, U. Peschel, et al. Experimental Observation of Linear and Nonlinear Optical Bloch Oscillations. In: *Phys. Rev. Lett.* 83.23 (Dec. 6, 1999), pp. 4756–4759 (cit. on p. 50).

[185] H. Sanchis-Alepuz, Y. A. Kosevich, and J. Sánchez-Dehesa. Acoustic Analogue of Electronic Bloch Oscillations and Resonant Zener Tunneling in Ultrasonic Superlattices. In: *Phys. Rev. Lett.* 98.13 (Mar. 29, 2007), p. 134301 (cit. on p. 50).

[186] A. Block, C. Etrich, et al. Bloch Oscillations in Plasmonic Waveguide Arrays. In: *Nat Commun* 5.1 (May 12, 2014), p. 3843. ISSN: 2041-1723 (cit. on p. 50).

[187] O. Morsch, J. H. Müller, et al. Bloch Oscillations and Mean-Field Effects of Bose-Einstein Condensates in 1D Optical Lattices. In: *Phys. Rev. Lett.* 87.14 (Sept. 13, 2001), p. 140402 (cit. on p. 50).

[188] M. Gustavsson, E. Haller, et al. Control of Interaction-Induced Dephasing of Bloch Oscillations. In: *Phys. Rev. Lett.* 100.8 (Feb. 28, 2008), p. 080404 (cit. on p. 50).

[189] M. Eckstein and P. Werner. Damping of Bloch Oscillations in the Hubbard Model. In: *Phys. Rev. Lett.* 107.18 (Oct. 27, 2011), p. 186406 (cit. on p. 50).

[190] F. Meinert, M. J. Mark, et al. Interaction-Induced Quantum Phase Revivals and Evidence for the Transition to the Quantum Chaotic Regime in 1D Atomic Bloch Oscillations. In: *Phys. Rev. Lett.* 112.19 (May 15, 2014), p. 193003 (cit. on p. 50).

[191] P. M. Preiss, R. Ma, et al. Strongly Correlated Quantum Walks in Optical Lattices. In: *Science* 347.6227 (Mar. 13, 2015), pp. 1229–1233 (cit. on pp. 50, 51).

[192] G. Corrielli, A. Crespi, et al. Fractional Bloch Oscillations in Photonic Lattices. In: *Nat Commun* 4.1 (Mar. 5, 2013), p. 1555. ISSN: 2041-1723 (cit. on pp. 50, 51).

[193] W. Zhang, H. Yuan, et al. Observation of Bloch Oscillations Dominated by Effective Anyonic Particle Statistics. In: *Nat Commun* 13.1 (May 2, 2022), p. 2392. ISSN: 2041-1723 (cit. on p. 50).

[194] A. M. Kosevich. Bloch Oscillations of Magnetic Solitons as an Example of Dynamical Localization of Quasiparticles in a Uniform External Field (Review). In: *Low Temperature Physics* 27.7 (July 1, 2001), pp. 513–541. ISSN: 1063-777X (cit. on p. 51).

[195] M. Schecter, D. M. Gangardt, and A. Kamenev. Quantum Impurities: From Mobile Josephson Junctions to Depletons. In: *New J. Phys.* 18.6 (May 2016), p. 065002. ISSN: 1367-2630 (cit. on pp. 51, 64, 65, 67).

[196] L. Corman, L. Chomaz, et al. Quench-Induced Supercurrents in an Annular Bose Gas. In: *Phys. Rev. Lett.* 113.13 (Sept. 26, 2014), p. 135302 (cit. on p. 53).

[197] S. Eckel, F. Jendrzejewski, et al. Interferometric Measurement of the Current-Phase Relationship of a Superfluid Weak Link. In: *Phys. Rev. X* 4.3 (Sept. 22, 2014), p. 031052 (cit. on p. 53).

[198] M. Aidelsburger, J. L. Ville, et al. Relaxation Dynamics in the Merging of N Independent Condensates. In: *Phys. Rev. Lett.* 119.19 (Nov. 6, 2017), p. 190403 (cit. on pp. 53, 57).

[199] R. M. Goldstein and C. L. Werner. Radar Interferogram Filtering for Geophysical Applications. In: *Geophysical Research Letters* 25.21 (1998), pp. 4035–4038. ISSN: 1944-8007 (cit. on p. 53).

[200] T. Isoshima, M. Nakahara, et al. Creation of a Persistent Current and Vortex in a Bose-Einstein Condensate of Alkali-Metal Atoms. In: *Phys. Rev. A* 61.6 (May 16, 2000), p. 063610 (cit. on p. 57).

[201] A. E. Leanhardt, A. Görlitz, et al. Imprinting Vortices in a Bose-Einstein Condensate Using Topological Phases. In: *Phys. Rev. Lett.* 89.19 (Oct. 22, 2002), p. 190403 (cit. on p. 57).

[202] K. C. Wright, R. B. Blakestad, et al. Driving Phase Slips in a Superfluid Atom Circuit with a Rotating Weak Link. In: *Phys. Rev. Lett.* 110.2 (Jan. 10, 2013), p. 025302 (cit. on p. 57).

[203] X.-L. Li, M. Gong, et al. *Manipulating Topological Charges via Engineering Zeros of Wave Functions*. Dec. 10, 2024. arXiv: 2412.07101 [cond-mat]. Pre-published (cit. on p. 60).

[204] D. M. Gangardt and A. Kamenev. Bloch Oscillations in a One-Dimensional Spinor Gas. In: *Phys. Rev. Lett.* 102.7 (Feb. 18, 2009), p. 070402 (cit. on pp. 63, 65).

[205] M. Schecter, D. M. Gangardt, and A. Kamenev. Dynamics and Bloch Oscillations of Mobile Impurities in One-Dimensional Quantum Liquids. In: *Annals of Physics* 327.3 (Mar. 1, 2012), pp. 639–670. ISSN: 0003-4916 (cit. on pp. 63, 65).

[206] F. Grusdt, A. Shashi, et al. Bloch Oscillations of Bosonic Lattice Polarons. In: *Phys. Rev. A* 90.6 (Dec. 4, 2014), p. 063610 (cit. on p. 63).

[207] M. Will and M. Fleischhauer. Dynamics of Polaron Formation in 1D Bose Gases in the Strong-Coupling Regime. In: *New J. Phys.* 25.8 (Aug. 2023), p. 083043. ISSN: 1367-2630 (cit. on pp. 63–65).

[208] L.-Z. Meng, X.-W. Luo, and L.-C. Zhao. *Self-Adapted Josephson Oscillation of Dark-Bright Solitons under Constant Forces*. Jan. 27, 2025. arXiv: 2501.15841 [cond-mat]. Pre-published (cit. on pp. 63, 64).

[209] X. Yu and P. B. Blakie. Propagating Ferrodark Solitons in a Superfluid: Exact Solutions and Anomalous Dynamics. In: *Phys. Rev. Lett.* 128.12 (Mar. 24, 2022), p. 125301 (cit. on p. 63).

[210] G. E. Astrakharchik and L. P. Pitaevskii. Motion of a Heavy Impurity through a Bose-Einstein Condensate. In: *Phys. Rev. A* 70.1 (July 20, 2004), p. 013608 (cit. on p. 65).

[211] M. Knap, C. J. M. Mathy, et al. Quantum Flutter: Signatures and Robustness. In: *Phys. Rev. Lett.* 112.1 (Jan. 7, 2014), p. 015302 (cit. on p. 65).

[212] A. Petković and Z. Ristivojevic. Dynamics of a Mobile Impurity in a One-Dimensional Bose Liquid. In: *Phys. Rev. Lett.* 117.10 (Sept. 1, 2016), p. 105301 (cit. on p. 65).

[213] A. J. Leggett. *Quantum Liquids: Bose Condensation and Cooper Pairing in Condensed-Matter Systems*. Oxford Graduate Texts. Oxford ; New York: Oxford University Press, 2006. 388 pp. ISBN: 978-0-19-852643-8 (cit. on p. 72).

[214] C. Raman, M. Köhl, et al. Evidence for a Critical Velocity in a Bose-Einstein Condensed Gas. In: *Phys. Rev. Lett.* 83.13 (Sept. 27, 1999), pp. 2502–2505 (cit. on p. 72).

[215] R. Onofrio, C. Raman, et al. Observation of Superfluid Flow in a Bose-Einstein Condensed Gas. In: *Phys. Rev. Lett.* 85.11 (Sept. 11, 2000), pp. 2228–2231 (cit. on p. 72).

[216] D. E. Miller, J. K. Chin, et al. Critical Velocity for Superfluid Flow across the BEC-BCS Crossover. In: *Phys. Rev. Lett.* 99.7 (Aug. 16, 2007), p. 070402 (cit. on p. 72).

[217] W. H. Keesom and G. E. Macwood. The Viscosity of Liquid Helium. In: *Physica* 5.8 (Aug. 1, 1938), pp. 737–744. ISSN: 0031-8914 (cit. on p. 72).

[218] N. V. Prokof'ev and B. V. Svistunov. Two Definitions of Superfluid Density. In: *Phys. Rev. B* 61.17 (May 1, 2000), pp. 11282–11284 (cit. on p. 73).

[219] J. Dalibard. Magnetic Interactions between Cold Atoms: Quantum Droplets and Supersolid States. Lecture notes. College de France, 2024 (cit. on p. 74).

[220] P. B. Blakie. Superfluid Fraction Tensor of a Two-Dimensional Supersolid. In: *J. Phys. B: At. Mol. Opt. Phys.* 57.11 (May 2024), p. 115301. ISSN: 0953-4075 (cit. on pp. 75, 76, 79, 80, 107).

[221] A. J. Leggett. On the Superfluid Fraction of an Arbitrary Many-Body System at T=0. In: *Journal of Statistical Physics* 93.3 (Nov. 1, 1998), pp. 927–941. ISSN: 1572-9613 (cit. on pp. 76, 81).

[222] R. P. Feynman. Atomic Theory of Liquid Helium Near Absolute Zero. In: *Phys. Rev.* 91.6 (Sept. 15, 1953), pp. 1301–1308 (cit. on p. 76).

[223] E. H. Lieb and R. Seiringer. *The Stability of Matter in Quantum Mechanics*. Cambridge: Cambridge University Press, 2009. ISBN: 978-0-521-19118-0 (cit. on p. 76).

[224] M. P. A. Fisher, P. B. Weichman, et al. Boson Localization and the Superfluid-Insulator Transition. In: *Phys. Rev. B* 40.1 (July 1, 1989), pp. 546–570 (cit. on p. 76).

[225] D. Jaksch, C. Bruder, et al. Cold Bosonic Atoms in Optical Lattices. In: *Phys. Rev. Lett.* 81.15 (Oct. 12, 1998), pp. 3108–3111 (cit. on p. 76).

[226] E. Taylor and E. Zaremba. Bogoliubov Sound Speed in Periodically Modulated Bose-Einstein Condensates. In: *Phys. Rev. A* 68.5 (Nov. 19, 2003), p. 053611 (cit. on p. 76).

[227] G. Watanabe, G. Orso, et al. Equation of State and Effective Mass of the Unitary Fermi Gas in a One-Dimensional Periodic Potential. In: *Phys. Rev. A* 78.6 (Dec. 29, 2008), p. 063619 (cit. on p. 76).

[228] J. Tao, M. Zhao, and I. B. Spielman. Observation of Anisotropic Superfluid Density in an Artificial Crystal. In: *Phys. Rev. Lett.* 131.16 (Oct. 18, 2023), p. 163401 (cit. on pp. 76, 87).

[229] G. Orso and S. Stringari. Superfluid Fraction and Leggett Bound in a Density-Modulated Strongly Interacting Fermi Gas at Zero Temperature. In: *Phys. Rev. A* 109.2 (Feb. 1, 2024), p. 023301 (cit. on p. 76).

[230] S. Giorgini, L. Pitaevskii, and S. Stringari. Effects of Disorder in a Dilute Bose Gas. In: *Phys. Rev. B* 49.18 (May 1, 1994), pp. 12938–12944 (cit. on p. 76).

[231] K. T. Geier, J. Maki, et al. Superfluidity and Sound Propagation in Disordered Bose Gases. In: *Phys. Rev. Res.* 7.1 (Feb. 21, 2025), p. 013187 (cit. on pp. 76, 107).

[232] D. Pérez-Cruz, G. E. Astrakharchik, and P. Massignan. Superfluid Fraction of Interacting Bosonic Gases. In: *Phys. Rev. A* 111.1 (Jan. 13, 2025), p. L011302 (cit. on pp. 76, 107).

[233] S. Saccani, S. Moroni, and M. Boninsegni. Excitation Spectrum of a Supersolid. In: *Phys. Rev. Lett.* 108.17 (Apr. 24, 2012), p. 175301 (cit. on p. 76).

[234] T. Macrì, F. Maucher, et al. Elementary Excitations of Ultracold Soft-Core Bosons across the Superfluid-Supersolid Phase Transition. In: *Phys. Rev. A* 87.6 (June 11, 2013), p. 061602 (cit. on p. 76).

[235] L. Chomaz. Probing the Supersolid Order via High-Energy Scattering: Analytical Relations among the Response, Density Modulation, and Superfluid Fraction. In: *Phys. Rev. A* 102.2 (Aug. 28, 2020), p. 023333 (cit. on p. 76).

[236] B. T. E. Ripley. Two-Dimensional Supersolidity in a Planar Dipolar Bose Gas. In: *Phys. Rev. A* 108.5 (2023) (cit. on pp. 76, 83).

[237] P. B. Blakie, L. Chomaz, et al. Compressibility and Speeds of Sound across the Superfluid-to-Supersolid Phase Transition of an Elongated Dipolar Gas. In: *Phys. Rev. Res.* 5.3 (Sept. 6, 2023), p. 033161 (cit. on p. 76).

[238] E. Poli, D. Baillie, et al. Excitations of a Two-Dimensional Supersolid. In: *Phys. Rev. A* 110.5 (Nov. 4, 2024), p. 053301 (cit. on pp. 76, 87).

[239] G. Biagioni, N. Antolini, et al. Measurement of the Superfluid Fraction of a Supersolid by Josephson Effect. In: *Nature* 629.8013 (May 2024), pp. 773–777. ISSN: 1476-4687 (cit. on pp. 76, 87).

[240] N. Chamel. Neutron Conduction in the Inner Crust of a Neutron Star in the Framework of the Band Theory of Solids. In: *Phys. Rev. C* 85.3 (Mar. 12, 2012), p. 035801 (cit. on p. 76).

[241] G. Watanabe and C. J. Pethick. Superfluid Density of Neutrons in the Inner Crust of Neutron Stars: New Life for Pulsar Glitch Models. In: *Phys. Rev. Lett.* 119.6 (Aug. 10, 2017), p. 062701 (cit. on p. 76).

[242] Yi-Cai Zhang, Zeng-Qiang Yu, et al. Superfluid Density of a Spin-Orbit-Coupled Bose Gas. In: *Phys. Rev. A* 94.3 (2016) (cit. on p. 76).

[243] W. M. Saslow. Superfluidity of Periodic Solids. In: *Phys. Rev. Lett.* 36.19 (May 10, 1976), pp. 1151–1154 (cit. on p. 79).

[244] W. M. Saslow. On the Superfluid Fraction and the Hydrodynamics of Supersolids. In: *J Low Temp Phys* 169.3 (Nov. 1, 2012), pp. 248–263. ISSN: 1573-7357 (cit. on p. 79).

[245] C. Josserand, Y. Pomeau, and S. Rica. Patterns and Supersolids. In: *Eur. Phys. J. Spec. Top.* 146.1 (July 1, 2007), pp. 47–61. ISSN: 1951-6401 (cit. on p. 79).

[246] C. Josserand, Y. Pomeau, and S. Rica. Coexistence of Ordinary Elasticity and Superfluidity in a Model of a Defect-Free Supersolid. In: *Phys. Rev. Lett.* 98.19 (May 9, 2007), p. 195301 (cit. on p. 79).

[247] N. Sepúlveda, C. Josserand, and S. Rica. Nonclassical Rotational Inertia Fraction in a One-Dimensional Model of a Supersolid. In: *Phys. Rev. B* 77.5 (Feb. 25, 2008), p. 054513 (cit. on pp. 79, 107).

[248] N. Sepúlveda, C. Josserand, and S. Rica. Superfluid Density in a Two-Dimensional Model of Supersolid. In: *Eur. Phys. J. B* 78.4 (Dec. 1, 2010), pp. 439–447. ISSN: 1434-6036 (cit. on pp. 79, 107).

[249] A. F. Andreev and I. M. Lifshitz. Quantum Theory of Defects in Crystals. In: *Soviet Journal of Experimental and Theoretical Physics* 29 (Jan. 1, 1969), p. 1107. ISSN: 1063-7761 (cit. on p. 83).

[250] M. A. Norcia, C. Politi, et al. Two-Dimensional Supersolidity in a Dipolar Quantum Gas. In: *Nature* 596.7872 (Aug. 2021), pp. 357–361. ISSN: 1476-4687 (cit. on p. 83).

[251] D. Trypogeorgos, A. Gianfrate, et al. Emerging Supersolidity in Photonic-Crystal Polariton Condensates. In: *Nature* 639.8054 (Mar. 2025), pp. 337–341. ISSN: 1476-4687 (cit. on p. 83).

[252] C. T. Lane, H. A. Fairbank, and W. M. Fairbank. Second Sound in Liquid Helium II. In: *Phys. Rev.* 71.9 (May 1, 1947), pp. 600–605 (cit. on p. 87).

[253] D. S. Jin, J. R. Ensher, et al. Collective Excitations of a Bose-Einstein Condensate in a Dilute Gas. In: *Phys. Rev. Lett.* 77.3 (July 15, 1996), pp. 420–423 (cit. on p. 87).

[254] M.-O. Mewes, M. R. Andrews, et al. Collective Excitations of a Bose-Einstein Condensate in a Magnetic Trap. In: *Phys. Rev. Lett.* 77.6 (Aug. 5, 1996), pp. 988–991 (cit. on p. 87).

[255] M. R. Andrews, D. M. Kurn, et al. Propagation of Sound in a Bose-Einstein Condensate. In: *Phys. Rev. Lett.* 79.4 (July 28, 1997), pp. 553–556 (cit. on p. 87).

[256] D. M. Stamper-Kurn, H.-J. Miesner, et al. Collisionless and Hydrodynamic Excitations of a Bose-Einstein Condensate. In: *Phys. Rev. Lett.* 81.3 (July 20, 1998), pp. 500–503 (cit. on p. 87).

[257] R. Meppelink, S. B. Koller, and P. van der Straten. Sound Propagation in a Bose-Einstein Condensate at Finite Temperatures. In: *Phys. Rev. A* 80.4 (Oct. 12, 2009), p. 043605 (cit. on p. 87).

[258] J. L. Ville, R. Saint-Jalm, et al. Sound Propagation in a Uniform Superfluid Two-Dimensional Bose Gas. In: *Phys. Rev. Lett.* 121.14 (Oct. 3, 2018), p. 145301 (cit. on pp. 87, 99).

[259] T. A. Hilker, L. H. Dogra, et al. First and Second Sound in a Compressible 3D Bose Fluid. In: *Phys. Rev. Lett.* 128.22 (June 2, 2022), p. 223601 (cit. on pp. 87, 99).

[260] P. Christodoulou, M. Gałka, et al. Observation of First and Second Sound in a BKT Superfluid. In: *Nature* 594.7862 (7862 June 2021), pp. 191–194. ISSN: 1476-4687 (cit. on pp. 87, 99).

[261] L. A. Sidorenkov, M. K. Tey, et al. Second Sound and the Superfluid Fraction in a Fermi Gas with Resonant Interactions. In: *Nature* 498.7452 (June 2013), pp. 78–81. ISSN: 1476-4687 (cit. on p. 87).

[262] D. K. Hoffmann, V. P. Singh, et al. Second Sound in the Crossover from the Bose-Einstein Condensate to the Bardeen-Cooper-Schrieffer Superfluid. In: *Nat Commun* 12.1 (Dec. 6, 2021), p. 7074. ISSN: 2041-1723 (cit. on p. 87).

[263] Z. Yan, P. B. Patel, et al. Thermography of the Superfluid Transition in a Strongly Interacting Fermi Gas. In: *Science* 383.6683 (Feb. 9, 2024), pp. 629–633 (cit. on p. 87).

[264] H. Watanabe and T. Brauner. Spontaneous Breaking of Continuous Translational Invariance. In: *Phys. Rev. D* 85.8 (Apr. 6, 2012), p. 085010 (cit. on pp. 87, 107).

[265] J. Hofmann and W. Zwerger. Hydrodynamics of a Superfluid Smectic. In: *J. Stat. Mech.* 2021.3 (Mar. 2021), p. 033104. ISSN: 1742-5468 (cit. on p. 87).

[266] C.-D. Yoo and A. T. Dorsey. Hydrodynamic Theory of Supersolids: Variational Principle, Effective Lagrangian, and Density-Density Correlation Function. In: *Phys. Rev. B* 81.13 (Apr. 15, 2010), p. 134518 (cit. on p. 87).

[267] M. Guo, F. Böttcher, et al. The Low-Energy Goldstone Mode in a Trapped Dipolar Supersolid. In: *Nature* 574.7778 (Oct. 2019), pp. 386–389. ISSN: 1476-4687 (cit. on p. 87).

[268] G. Natale, R. M. W. van Bijnen, et al. Excitation Spectrum of a Trapped Dipolar Supersolid and Its Experimental Evidence. In: *Phys. Rev. Lett.* 123.5 (Aug. 1, 2019), p. 050402 (cit. on p. 87).

[269] Y.-Q. Zou, É. L. Cerf, et al. Optical Control of the Density and Spin Spatial Profiles of a Planar Bose Gas. In: *J. Phys. B: At. Mol. Opt. Phys.* 54.8 (Apr. 2021), 08LT01. ISSN: 0953-4075 (cit. on p. 92).

[270] E. Busley, L. E. Miranda, et al. Compressibility and the Equation of State of an Optical Quantum Gas in a Box. In: *Science* 375.6587 (Mar. 25, 2022), pp. 1403–1406 (cit. on p. 101).

[271] G. Pupillo. Strongly Correlated Gases of Rydberg-Dressed Atoms: Quantum and Classical Dynamics. In: *Phys. Rev. Lett.* 104.22 (2010) (cit. on p. 107).

[272] N. Henkel. Three-Dimensional Roton Excitations and Supersolid Formation in Rydberg-Excited Bose-Einstein Condensates. In: *Phys. Rev. Lett.* 104.19 (2010) (cit. on p. 107).

[273] F. Cinti, T. Macrì, et al. Defect-Induced Supersolidity with Soft-Core Bosons. In: *Nat Commun* 5.1 (Feb. 4, 2014), p. 3235. ISSN: 2041-1723 (cit. on p. 107).

[274] J. B. Balewski, A. T. Krupp, et al. Rydberg Dressing: Understanding of Collective Many-Body Effects and Implications for Experiments. In: *New J. Phys.* 16.6 (June 2014), p. 063012. ISSN: 1367-2630 (cit. on p. 107).

[275] F. Maucher. Rydberg-Induced Solitons: Three-Dimensional Self-Trapping of Matter Waves. In: *Phys. Rev. Lett.* 106.17 (2011) (cit. on p. 107).

[276] J. Honer, H. Weimer, et al. Collective Many-Body Interaction in Rydberg Dressed Atoms. In: *Phys. Rev. Lett.* 105.16 (Oct. 15, 2010), p. 160404 (cit. on p. 107).

[277] Y. Pomeau and S. Rica. Dynamics of a Model of Supersolid. In: *Phys. Rev. Lett.* 72.15 (Apr. 11, 1994), pp. 2426–2429 (cit. on p. 107).

[278] M. Kunimi and Y. Kato. Mean-Field and Stability Analyses of Two-Dimensional Flowing Soft-Core Bosons Modeling a Supersolid. In: *Phys. Rev. B* 86.6 (Aug. 24, 2012), p. 060510 (cit. on p. 107).

Contents